MULTISCALE COMPUTATIONAL SIMULATION OF MULTIDIMENSIONAL CHEMICALLY REACTING FLOW OVER WASHCOATED HETEROGENEOUS CATALYSTS

by

Justin M. Blasi

ProQuest LLC.
789 East Eisenhower Parkway
P.O. Box 1346
Ann Arbor, MI 48106 - 1346

A thesis submitted to the Faculty and the Board of Trustees of the Colorado School of Mines in partial fulfillment of the requirements for the degree of Doctor of Philosophy (Mechanical Engineering).

Golden, Colorado

Date ____________________

Signed: ____________________
Justin M. Blasi

Signed: ____________________
Dr. Robert J. Kee
Thesis Advisor

Golden, Colorado

Date ____________________

Signed: ____________________
Dr. Greg Jackson
Professor and Head
Department of Mechanical Engineering

ABSTRACT

This work addresses three distinct but interrelated topics: The simulation and evaluation of a novel ceramic microchannel heat exchanger; the adaptation of in situ adaptive tabulation for the acceleration of transient, heterogeneous chemistry in large CFD models; and the development of catalytic washcoat performance relations informed by 3D reconstructions of actual, commercial washcoats.

Ceramic microchannel heat exchangers/reactors have several distinct advantages. They are cost effective, chemically inert, are capable of operating at high temperatures, and integrate well with internal catalysts. In this work, a particular design for a ceramic microchannel reactor is evaluated. A 3D computational fluid dynamics model with conjugate heat transfer and detailed kinetics for methane steam reforming was built. The model is used to evaluate the kinetic and hydraulic performance of the reactor as well as explore potential catalyst degradation mechanisms.

In situ adaptive tabulation (ISAT) is a technique for accelerating the simulation of detailed kinetic mechanisms. The present work adapts this method, which was originally developed for homogeneous chemistry, to accelerate transient, heterogeneous kinetics. The approach is demonstrated on a series of transient simulations of methane steam reforming within the ceramic microchannel reactor model. For the particular case studied, 10 – 20 times speed-up factors were observed over the internal kinetics solver of ANSYS FLUENT with no appreciable decrease in accuracy.

Data collected from FIB-SEM imaging provided nanoscale phase information for actual, commercial washcoat structures. Algorithms were developed to process, filter, and discriminate phase information in the FIB-SEM images to facilitate 3D reconstruction. Reconstructed washcoat pores were cast in a dimensionless context and simulated to predict their catalytic performance. Performance relations, first for pores alone, and then for washcoats as a whole, were developed based on good agreement between reconstructed pores and an idealized 2D cylindrical pore model. The generalized relations suggest optimum washcoat depths based on effective kinetic rates and diffusion coefficients. Additionally, a modified washcoat factor was developed to relate the often used multiplicative factor $F_{\text{cat,geo}}$ to a particular reaction-diffusion regime. These have important implications not only on the accurate simulation of washcoat performance but also for washcoat manufacturing.

TABLE OF CONTENTS

LIST OF FIGURES

LIST OF TABLES

LIST OF SYMBOLS

Activation energy	E_{a}
Catalytic flat plate flux	J_{o}
Concentration	C
Damköhler number	Da
Density	ρ
Depth of reaction	Z_{95}
Diffusive mass flux	$\mathbf{j}_k$
Effective diffusion coefficient	D_{eff}
Effectiveness	η
Effectiveness, heat-exchangers	ϵ
Enthalpy	h
Error tolerance	$\varepsilon_{\mathrm{tol}}$
Forward rate coefficient	ν'_{ki}
Geometric area	A_{geo}
Heat of reaction	Q_{rxn}
Heat transfer coefficient	h
Hydraulic diameter	D_h
Idealized geometric area	A_{o}
Kinetic rate constant	k
Mapping-gradient matrix	$\mathbf{A}^n$

Mass flow rate	$\dot{m}$
Mass fraction of species k	Y_k
Mass source for species k	$\dot{s}_k$
Mole fraction of species k	X_k
Molecular weight of species k	W_k
Normalized pore flux	Γ_p
Nusselt number	Nu
Pore aspect ratio	α
Pore flux	J
Pore radius	R
Pore volume	V_p
Ratio of geometric area to pore opening area	β
Reverse rate coefficient	ν''_{ki}
Reynolds number	Re
Specific heat per unit mass	c_p
Sticking coefficient	γ_i
Surface area	A_s
Surface site density	Γ
Surface site fraction of species k	θ_k
Tabulated solution	$\mathbf{f}^n$
Tabulated thermochemical state	$\mathbf{x}^\mathrm{n}$
Thermal conductivity	λ
Thiele modulus	Φ

Time	t
Viscosity	μ
Washcoat multiplicative factor	$F_{\mathrm{cat,geo}}$

LIST OF ABBREVIATIONS

Backward differential formula	BDF
Brunauer-Emmett-Teller	BET
Catalytic partial oxidation	CPOX
Colorado Fuel Cell Center	CFCC
Computational fluid dynamics	CFD
Differential algebraic equation	DAE
Ellipsoid of accuracy	EOA
Finite element method	FEM
Focused ion beam	FIB
Gas hourly space velocity	GHSV
Graphics processing unit	GPU
Heat exchanger - reactor	HEX-reactor
In Situ Adaptive Tabulation	ISAT
Lawrence Livermore National Laboratory	LNLL
Mass flow controller	MFC
Model predictive control	MPC
Ordinary differential equation	ODE
Region of accuracy	ROA
Scanning electron microscopy	SEM
Solid oxide fuel cell	SOFC

Standard liters per minute	SLPM
Steam methane reforming	SMR
Steam-to-carbon ratio	S/C
User defined memory	UDM

ACKNOWLEDGMENTS

The following work represents not only several years of my life, but also roughly half a million people-hours of encouragement and support from family, friends, and colleagues. I could not have done it without them.

I could not be where I am today without the love and support of my parents. Growing up, they managed to both encourage my interests in science and engineering while also tolerating my "experiments" that seemed to consume every flat surface in the house. I suppose a large portion of this degree belongs to you, though I suspect you'll want me to keep it at my house so you don't have to store any more of my stuff. Thank you to you both, I love you.

To my brother, thank you for all the support, direction, and housing you provided over the years we lived and attended Mines together. You've turned out to be quite an engineer yourself and have really grown into the man that I wished you were years ago. I love you big brother.

I will forever be indebted to my wife for her unwavering support during my studies. You were patient and supportive while also pushing me when I needed it. I could not have done it without you and am incredibly lucky to have you. I love you.

I would like to thank my advisor Dr. Robert Kee for years of sage advice and scientific tutelage. As scrupulous as they come, I am undoubtedly a better scientist and researcher thanks to you.

My time at Colorado School of Mines would not have been nearly as productive or enjoyable if it weren't for my exceptional colleagues in the thermal sciences group. I would like to thank those, both past and present, whom I've had the pleasure of working with including, but not limited to, Andreas Wiedemann, Dr. Canan Karakaya, Peter Weddle, Dr. Danielle Murphy, and Dr. Huayang Zhu.

I would also like to thank my thesis committee for their support and advisement: Dr. Greg Bogin, Dr. Anthony Dean, Dr. Neal Sullivan, and Dr. Tyrone Vincent. I greatly appreciate the time and effort you put into the following work. In retrospect, given the decades of scientific expertise at my disposal, I should have used more of it.

I also appreciate the many fruitful discussions and helpful advice given by Dr. Graham Goldin when I was just getting my feet wet in CFD.

Additionally, this work would not have been possible without funding from the Office of Naval Research via grant N00014-08-1-0539 and the Air Force Office of Scientific Research via grant FA9550-12-1-0495.

To Madge

CHAPTER 1

INTRODUCTION

Catalytic processes play a critical role in modern industrial, energy conversion, and environmental fields. Applications can range from large industrial catalytic processes that produce chemical products measured in the millions of tons [1, 2] to small embedded applications such as automotive catalytic converters. Often the economic and energetic viability of these processes depends heavily on application specific designs for reactors and process optimality. This presents a significant challenge from a design perspective as high-performance designs often require detailed understanding of complex chemical, fluid dynamic, and conjugate heat transfer phenomena. Each of these aspects can be complex in their own right but often must be treated together due to the coupled nature of flow, heat transfer, and kinetics. The numerical simulation of catalytic processes is a valuable tool in the design and optimization workflow, often accelerating design iterations and facilitating a more granular understanding of the process, while reducing development costs.

Part of the work presented herein focuses on the development and simulation of a novel ceramic microchannel heat exchanger and reactor. The benefits of microchannel heat exchangers and reactors (collectively HEX-reactors) lend themselves well to high-performance embedded thermal and chemical systems and can provide significant gains in efficiency through process intensification. As an example, Figure 1.1 depicts a process flow configuration of a solid-oxide fuel cell (SOFC) system. The high temperature operation of SOFCs typically requires some pre-heating for inlet gases (often air). The balance of plant of a system such as the one shown can be improved by recouping waste heat (as depicted) elsewhere in the system to accomplish some of the pre-heating. Additionally, SOFCs operate on hydrogen rich fuel streams, but due to the inefficiencies in storing hydrogen, often hydrocarbon fuels are stored instead. The hydrocarbon fuels (e.g., methane, propane) must be reformed to produce a hydrogen rich syngas for use in the SOFC. This is a highly endothermic process which requires thermal support to maintain high conversion. The tight thermal coupling of microchannel heat exchangers means integrated catalytic reforming on one channel can be supported by waste heat from exhaust gases supplied on the other channel.

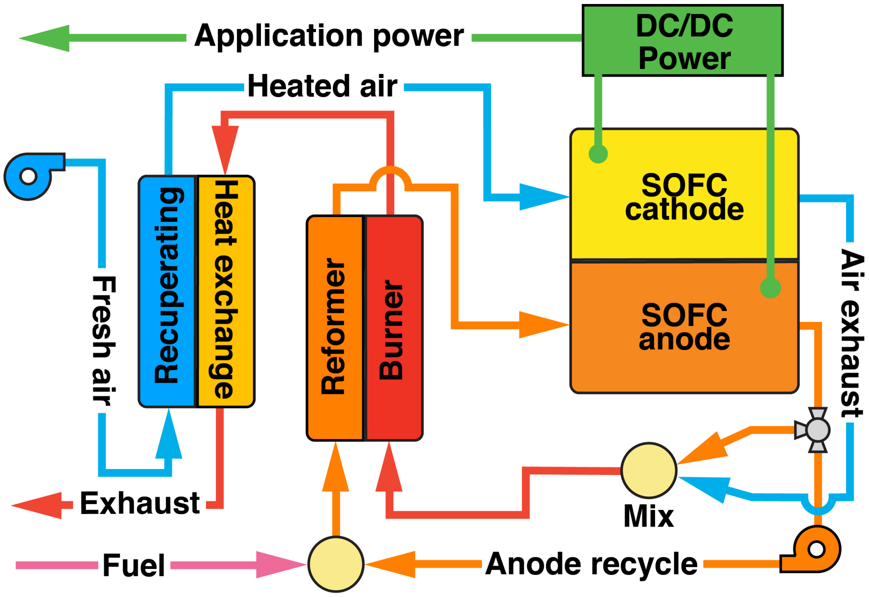

Figure 1.1: A process flow diagram for an example embedded SOFC system showing two possible use cases for a compact, high-performance heat exchanger and fuel reformer.

The computational fluid dynamics (CFD) models developed in Chapter 2 are centered around capturing the flow and thermal performance of a microchannel HEX-reactor developed at the Colorado Fuel Cell Center (CFCC). These models are validated against experimental data collected from HEX-reactors manufactured in-house and by CoorsTek. The models assist in characterizing the HEX-reactor performance and in quantifying unknown experimental variables. These models are then extended to integrate the simulation of steam methane reforming (SMR) via a detailed kinetic mechanism. The model can then provide insight into the thermal and chemical performance of the HEX-reactor that is not accessible by experiment.

The numerical simulation of large fluid dynamics and chemical kinetics problems has some challenges though. Broadly speaking, a requirement of useful numerical results is accurately capturing the physics of interest. The pursuit of this goal often leads to more geometrically complex models (e.g., 1-dimensional to 2- or 3-dimensional), the inclusion of additional coupled phenomena (e.g., conjugate heat transfer, detailed chemical kinetics), and more complex, and ideally more accurate, chemical kinetics mechanisms. For reasons discussed further in Section 1.1.2, the coupling of CFD and detailed chemical kinetics presents a unique set of challenges. Due to the nature of the way coupled CFD and kinetics problems are simulated, the computational cost of solving such problems becomes very expensive. So much so that the utility of models suffer.

A second aspect of the research presented in this work is the adaptation of in situ adaptive tabulation (ISAT) for accelerating the simulation of heterogeneous chemistry, specifically for transient simulations where the computational cost is exacerbated by time-stepping. By adapting ISAT to the problem of transient, heterogeneous chemistry, significant acceleration in simulation time is realized. In fact, the thermochemical study of the ceramic microchannel reactor was greatly aided by the use of ISAT for simulating SMR.

A third aspect of the research presented is focused on the performance, characterization, and manufacturing of catalytic washcoats. The efficacy of any catalytic process depends on exposing as much catalyst surface area as possible to reactants. In packed bed reactors, this is done by using porous pellets or similar structures impregnated with the catalyst of choice. For applications where the pressure drop associated with driving flow through a packed bed is undesirable, a high surface area substrate (e.g., a monolithic structure as seen in Figure 1.2) is coated with a catalyst containing slurry and fired to produce a thin, porous surface washcoat. The characteristics of this washcoat (e.g., porosity, tortuosity, surface area) have a large effect on the performance of the reactor as a whole.

Relying on new techniques for imaging porous structures at the μm and nm scale, research is presented that seeks to characterize actual washcoat performance and generalize the results in a dimensionless form. This work has repercussions both for the accurate simulation of heterogeneous chemistry but also for washcoat manufacturing as well.

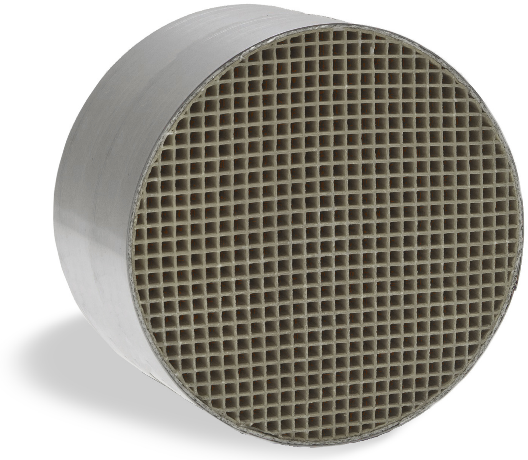

Figure 1.2: An example catalytic monolith structure with a dipcoated washcoat.

1.1 Motivations and background

While the three aspects of the research presented here are very much interrelated, they will largely be treated independently. The following sections (and the chapters to follow) will treat each subject in turn. What follows are discussions on the purpose of each aspect of the research and the related literature on the subject.

1.1.1 Ceramic microchannel fuel reformer model

Microchannel heat exchangers and reactors offer high performance and close thermal coupling in relatively small packages. The motivating principle driving the development of microchannel HEX-reactors is the enhanced convective heat transfer as evidenced by the Nusselt number relation

$$h = \mathrm{Nu}\frac{\lambda}{D_h} \tag{1.1}$$

where h is the heat transfer coefficient, λ the thermal conductivity of the working fluid, and D_h the hydraulic diameter of the flow channel. By reducing the hydraulic diameter for a particular flow of interest, high heat transfer can be realized in low volume devices. These advantages are well documented in the literature [3, 4, 5, 6, 7].

Common configurations for compact heat exchangers are crossflow and counterflow, describing the orientation of the independent fluid flow directions with respect to each other. When possible, the counterflow configuration is preferred due to its superior thermal characteristics. Counterflow configurations are capable of producing the largest temperature changes between the two fluids amongst any other configuration [8]. Shah et al. point out, though, that the requirement that inlet and outlet ports for the separate flows must exist together at either side of the heat exchanger can present manufacturing and manifolding challenges.

Hasan et al. [9] used 3D CFD modeling of generalized microchannel structures to optimize channel geometry for counterflow configurations. They found generally that for the same volume heat exchanger, increasing the number of microchannels improved effectiveness but also increased the pressure drop across the reactor. Additionally, they reported that circular channels provided the optimal thermal and hydraulic performance. Along the same lines, Folio et al. [10] used genetic optimization to codify the balance that must be struck between high heat transfer and pressure drop.

Often, microchannel reactors have been fabricated from metals due to their ease of manufacturing, robustness, and good thermal properties for high heat transfer. There is also significant interest in the development of ceramic HEX-reactors [11, 12]. Ceramic materials can provide an ideal substrate for integrated catalyst deposition, tend to be more chemically inert and therefore resistant to corrosion, and can operate at higher temperatures compared to their metal counterparts.

Integrating catalyst into microchannel geometries to couple the function of heat exchanger and reactor (HEX-reactor) has some distinct advantages. Often chemical processes of interest are either highly endo- or exothermic. Having catalytic surfaces directly coupled to high performance microchannel heat exchanger geometries allows for tight temperature control and ideally isothermal operation. This configuration along with the high surface area to volume ratio inherent to microchannel designs, lends itself well to high-performance embedded systems and gains in efficiency through process intensification.

In a review by Kiwi-Minsker et al. [11] they note that in addition to improved thermal control, microchannel reactors can provide integrated chemistry without the hydraulic cost of backed bed reactors. Even more, the microchannels allow for high conversion at reduced residence times which can improve selectivity and mitigate some catalyst deactivation pathways.

A particular catalytic process of interest both industrially and in the development of embedded fuel cell systems [13] is the production of syngas via steam methane reforming (SMR). Globally the reaction is described as

$$CH_4 + H_2O \longleftrightarrow CO + 3H_2 \qquad \Delta H^0_{298} = +206 \text{ kJ/mol} \tag{1.2}$$

$$CO + H_2O \longleftrightarrow CO_2 + H_2 \qquad \Delta H^0_{298} = -41 \text{ kJ/mol} \tag{1.3}$$

The first reaction is highly endothermic while the second reaction, the water-gas shift reaction, is mildly exothermic. The overall highly endothermic nature of this important reaction makes microchannel reactors, with their inherently tight thermal coupling and high surface area to volume ratio, an attractive option [14, 15].

Grasso et al. studied manufacturing techniques, specifically plate bonding techniques and their effect on methane conversion for a 0.6Rh-Al_2O_3 catalyst [16]. In their case, they were using metal reactor plates and using either high temperature brazing or laser bonding to manufacture the reactor structure. What is relevant to ceramic microchannel reactors is that inter-channel bonding, or failure thereof, caused marked reductions in methane conversion due to poor thermal conduction between layers. For some flow conditions the difference between well bonded and poorly bonded reactor plates was a roughly 40% reduction in methane conversion. Manufacturing techniques for the ceramic microchannel reactors under study here have produced essentially non-existent bond lines [17].

Zhai et al. developed a 2D channel flow model simulating methane steam reforming [18]. A backing channel is simulated by global reactions for methane combustion on Platinum. They compared the reactor performance for different wall thermal conductivities approximating a ceramic and metal wall, noting that the ceramic wall produced a large temperature variation on the reactive side. It should be noted their channel model was simulated as co-flow configuration which tends to produce lower overall heat transfer compared to counterflow.

1.1.2 Accelerated chemistry simulation

High fidelity computational fluid dynamics (CFD) models with integrated detailed chemistry can be computationally expensive. As the number of reactive species grows, solving the ordinary differential equations (ODEs) associated with species conservation becomes the dominant factor in simulation time. As the complexity, and ideally the accuracy of these kinetic mechanisms increases, the utility of the model can suffer as run-times become long. The time required to run parameterized studies or transient simulations can be prohibitive.

Essentially all CFD software implements some sort of split-operator algorithm, wherein detailed chemical kinetics is simulated on a cell-by-cell basis that is indirectly coupled to the underlying solution of the partial differential equations representing mass and energy conservation. The chemical kinetics problem is represented as a system of ordinary differential equations (ODE) within each finite-volume cell that includes chemistry. For steady-state heterogeneous kinetics, the surface-site constraints usually lead to solving a system of differential algebraic equations (DAEs). For transient simulations, the mathematical formulation requires solving a set of ODEs as initial value problems. In such split-operator methods, two time steps are relevant. The CFD simulation typically uses relatively large time steps, which are characteristic of the macroscopic flow problem. However, the local kinetics problems typically use high-fidelity ODE (or DAE) software that use much smaller time steps that vary adaptively to maintain accuracy and stability in the stiff differential-equation solutions.

The individual evaluations of the chemistry are relatively inexpensive, solving the number of surface species n_{s} ODEs over the CFD time step Δt. In the context of a large CFD problem with thousands to tens of millions of chemically active control volumes, the combined cost of solving the ODEs for every cell, for every iteration, and for every time step is prohibitive.

Various methods to accelerate the simulation of chemical kinetics have been proposed, including chemical mechanism reduction [19], precomputed and mapped rate data [20, 21, 22], low-dimensional manifolds [23] and multi-zone methods [24, 25].

Tomlin et al. details procedures for largely avoiding the problem by judicious use of mechanism reduction. Using rate and sensitivity analyses, species found to have small influence on major species production rates are neglected. Additionally, reduction using time-scale analysis can neglect species whose effect is diminished within the time-scales of interest. Tomlin et al. notes that while significant computational savings can be had using mechanism reduction, often the reduced mechanisms are only accurate for a very specific kinetic regime and/or time-scale. The same overall reaction but at different concentrations or analyzed at different time-scales would require a separate mechanism reduction procedure.

Multi-zone methods seek to accelerate the simulation of CFD and combined kinetics problems by effectively decoupling the two. McNenly et al. achieved a 35 – 250 fold acceleration in the simulation of homogeneous charge compression ignition in an engine cylinder by subdividing the geometry into a series of coupled, well-mixed reactors. Energy, mass, and species conservations equations are solved across zones, but by not resolving the full CFD problem within each zone, the scaling problem described above is avoided.

Aceves et al. developed a hybrid approach that fully resolves the CFD problem and establishes temperature profiles, and only then is the chemistry solved [25]. By separating the solution of the CFD and chemistry, significant speed-ups were observed. For combustion simulations, the predicted maximum pressure and burn duration agreed well with expected results, but certain emissions predictions suffered in accuracy.

A different class of acceleration techniques center around the notion that for a given set of variables within a chemically active control volume, not all of the thermochemical space defined by those variables is used. That is, given physical constraints on the chemical composition within a reactor, the chemistry falls on a low-dimensional manifold. Maas et al. described a method for reducing a detailed mechanism to a low-dimensional manifold, and then tabulating the solution of the chemistry problem along that manifold. By tabulating the chemistry solution a priori, solutions can be retrieved at a reduced cost at run-time.

Votsmeier, operating on a similar idea, used multidimensional, cubic splines as opposed to tabulation, to fit reaction-space low-order manifolds a priori [20]. The spline fits could capture the dynamics of the kinetics with smooth interpolation between solutions. The splines could then be evaluated at run-time at a reduced cost compared to evaluating the chemistry. The method is valuable for relatively simple kinetic mechanisms. As the number of variables that have to be fit increases (e.g., species concentrations, temperature) the cost and complexity of the cubic splines becomes large and acceleration gains are lost. Additionally, the thermochemical space of the problem must be known a priori, or splines fit to cover a sufficiently large thermochemical space so as to ensure the problem of interest is contained within. Further Nien et al. extended the use of multidimensional splines to incorporate precomputed multi-scale data as well [21]. Micro- and mesoscale data was precomputed for later retrieval in a macroscale model. They reported speed of factors in the several orders of magnitude. Again, the efficiency of the cubic spline method relies on relatively few fitting parameters and thus limits the physical systems it can capture.

A method that has become widely used in homogeneous chemistry is in situ adaptive tabulation (ISAT). ISAT is widely used in combustion modeling to accelerate the simulation of homogeneous kinetics with tens to hundreds of species [26, 27, 28]. In the context of homogeneous combustion chemistry, speed-up factors of 1000-fold have been reported.

More recently ISAT has been adapted to accelerate heterogeneous chemistry in steady-state catalytic reactor simulations [29, 30]. Kumar and Mazumder achieved speed-up factors of 5 – 11 for steady-state catalytic-combustion models. The current work builds upon the success of Kumar et al. by expanding ISAT to transient simulations with detailed catalytic reaction mechanisms.

1.1.3 Microstructural washcoat analysis

Catalytic washcoats play a critical role in both the chemical and economic performance of catalytic systems. The inclusion of a porous support structure for metal catalysts greatly increases the area available for catalytic activity thereby improving chemical conversion for a given reactor. The manufacturing and physical characteristics of washcoats have been studied extensively due to their critical role.

When developing reacting flow models, the large scale disparity between washcoat morphological features (on the order of nm – μm) and flow channel geometry (on the order of mm) makes it particularly difficult to fully resolve the important physics at their respective scales. Figure 1.3 illustrates the multi-scale nature of a typical catalyst monolith. The individual channel dimensions are typically on the order of a millimeter and the monolith is typically a few centimeters long. The thin catalyst washcoat, which covers the monolith walls, is typically a few tens of microns thick. When modeling at the monolith macroscale and the individual channel scale, because of great scale disparity, microstructural details of the washcoat must be approximated. The simplest approach, which is widely practiced, is simply to assign an empirical factor by which the effective catalyst area is a multiple of the channel wall area [31, 32]. Of course, the multiplicative factor should be informed by measurements, such as BET surface area or chemisorption characteristics. The current work seeks to improve the empiricism that is inherent in upscaling by incorporating knowledge from models that consider the actual catalyst microstructure.

As illustrated in the upper balloons of Figure 1.3, alternative notional representations of the catalyst microstructure can be developed. One approach is to represent the microstructure as assemblies of packed spheres, which can be characterized by packing structure, particle diameter, pore diameter, porosity, and tortuosity. Such representations have appeal

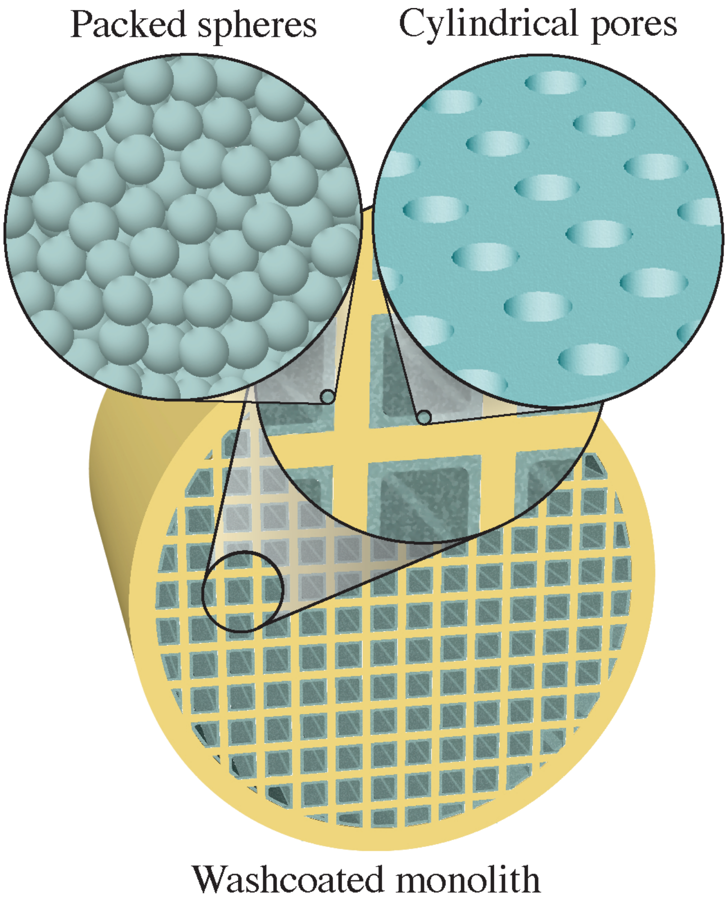

Figure 1.3: Illustration of a rectangular-channel monolith, showing a range of scales for a washcoat catalyst. The two upper balloons illustrate alternative idealizations of the washcoat microstructure.

because modeling approaches are well established. For packed spheres, Kozney–Carman relationships can be used to model the effective porous-media properties. Dusty-Gas models have been developed and applied successfully to represent reactive porous-media in applications such as fuel-cell electrodes [33, 34]. However, such success depends upon the underlying microstructures being adequately represented by homogeneous porous media.

The right-hand balloon in Figure 1.3 illustrates a different idealized notion of the washcoat layer. In this case, cylindrical holes penetrate into the washcoat layer. Penetrating holes may provide a better idealization than isotropic porous media. Such hole structures can be modeled using approaches based on the Thiele modulus [35, 36].

Models based on Thiele modulus are well understood and widely practiced, but are usually applied to pores within pelletized catalysts in packed beds. However, there are alternative implementations of the Thiele modulus, leading to alternative representation of performance metrics such as pore effectiveness [37, 38, 39, 40]. Such models lump complex microscopic geometric influences into empirical effective diffusion coefficients. Without direct knowledge of actual pore microstructures, establishing and validating the needed empiricism is difficult.

Reaction and transport processes within the porous catalysts proceed on greatly disparate length scales (nano, micro and macro), depending on multiscale pore geometries and characteristics. One upscaling approach to bridge these length scales is based upon evaluating effective diffusion coefficients within porous media. However, because the effective transport depends on complex microscale processes, finding general macroscale representations of effective diffusion coefficients is difficult. Berson et al. [41] developed a procedure to predict effective diffusion coefficients within computer-synthesized porous media. Their studies showed that for discrete geometries, because the definition of the characteristic length is difficult, it is not possible to accurately predict diffusivity for a wide range of porosities. Salejova et al. [42] studied the effect of microstructural properties to determine effective diffusion coefficients and permeabilities in porous media. The pore structures are computer generated and based on the microscopic images. They suggested that the contribution of nano-pores towards the total diffusion flux is significant and can not be neglected, but they can be neglected for calculating the permeability. Zalc et al. [43] studied the diffusion processes within random porous structures. By using computer-generated random loosely packed spheres, they reported the effect of porosity on the determination of tortuosity, and hence the effective diffusion coefficient. Their simulations revealed that accurate determination of Knudsen diffusion length scale is crucial.

Stutz et al. [44] simulated a reactor for syngas production via steam reforming of methane while fully resolving the washcoat layer. By varying the depth of the modeled washcoat, they identified an optimum thickness in terms of H_2 and CO yield and CH_4 conversion. Their formulation for the washcoat relied on volume averaged reactions and properties based on Knudsen number relations and assumptions about pore geometry.

Using synthesized or reconstructed microscale geometries, a number of groups have developed three-dimensional models to study catalyst performance at the microscale [45, 45, 46, 47, 48, 42, 49]. However, generalization of the reaction-diffusion problems are difficult. Studies often focus on specific reaction kinetics for given operating conditions and a specific catalyst.

Novák et al. [48] studied diffusion within catalytic coatings for a digitally reconstructed, three-dimensional, porous layer for CO oxidation over a Pt-γAl_2O_3 catalyst. Their model represented the microscale and macroscale structures of the catalyst. Results showed that random-pore models cannot accurately predict effective diffusivities (25-45% lower compared to the three-dimensional model) for CO, and hence cannot predict experimental measurements. The differences were more pronounced at lower levels of macroporosity. Thus, accurate three-dimensional representations should include both micro and macro pore structures. Pereira et al. [47] also studied the effect of catalyst microstructures on CO oxidation rates in three-dimensional and one-dimensional washcoat models. The catalysts were composed of nanoscale to macroscale pores. These results showed that accurate effective diffusivities are needed to accurately represent measured performance.

Koči et al. [45, 50] developed relationships between the catalyst's particle size and effectiveness factor for the CO oxidation reaction over Pt-γAl_2O_3 catalysts within a three-dimensional computer-generated porous structure. Their model, which incorporated macroscale and mesoscale pores, predicted concentration and temperature variations within the catalytic media. They reported a correlation between process optimization and its relationship to microstructural properties of the catalyst (e.g., porosity and particle size) at a larger scale (e.g., monolith channel in a catalytic converter for automotive exhaust gas after-treatment).

Naseri et al. [49] studied the effect of microscale characteristics on macroscale methane reforming processes. They synthesized three-dimensional catalyst microstructures with a particle-packing algorithm. The three-dimensional simulations considered methane steam reforming at both reactor level (macroscale) and the catalyst microstructure level (microscale). Their study emphasized the significant effect of the catalyst intraparticle and interparticle porosity as well as the particle size on the reaction effectiveness factor and methane conversion. Results suggested optimal washcoat structures for methane reforming.

CHAPTER 2

MICROCHANNEL REFORMER MODEL

The work presented in this chapter centers around the HEX-reactor design illustrated in Figure 2.1. The HEX-reactor is manufactured by machining or pressing the internal flow paths into a compressed plate of 94% alumina powder supplied by CoorsTek [51]. For a single plate, this creates a flow path and de-facto "floor" separator as one piece. The inlet and outlet ports are designed such that the plates can be stacked, alternating every other one by 180°, such that two independent flow channels are formed. The stack of green plates are then compressed and fired, creating a single, seamless, hermetically sealed ceramic component. The details surrounding the manufacturing process of the HEX-reactor are not the focus of this research so the reader is referred to publications by Kee et al. (2011) [17] and Murphy (2013) [52] for further details.

The nominal HEX-reactor design is approximately 100 mm long by 50 mm wide. The 4-layer configuration has a thickness of approximately 7.4 mm. The height of the flow channel and the thickness of the "floor" separator between flow channels are approximately equal at 0.7 mm. A summary of some geometric parameters of the HEX-reactor design are collected in Table 2.1. Detailed schematics of the reactor design can be found in Appendix A.

For either of the two independent flow paths, entrant gases are delivered via the single large manifolding hole (top-center of the plate illustrated in Figure 2.1). Gases are distributed across the breadth of the HEX-reactor using the diverging ribs at the microchannel entrance. Gaps in ribs separating the flow channels allow for pressure variation among channels to equalize. At the opposite end of the HEX-reactor, the flow is split and exits via two outlet ports. To facilitate high performance heat transfer, the HEX-reactor is run in a counter-flow configuration. The internal rib structures serve two purposes: To distribute gases evenly across the HEX-reactor to improve heat transfer between layers and effectively use

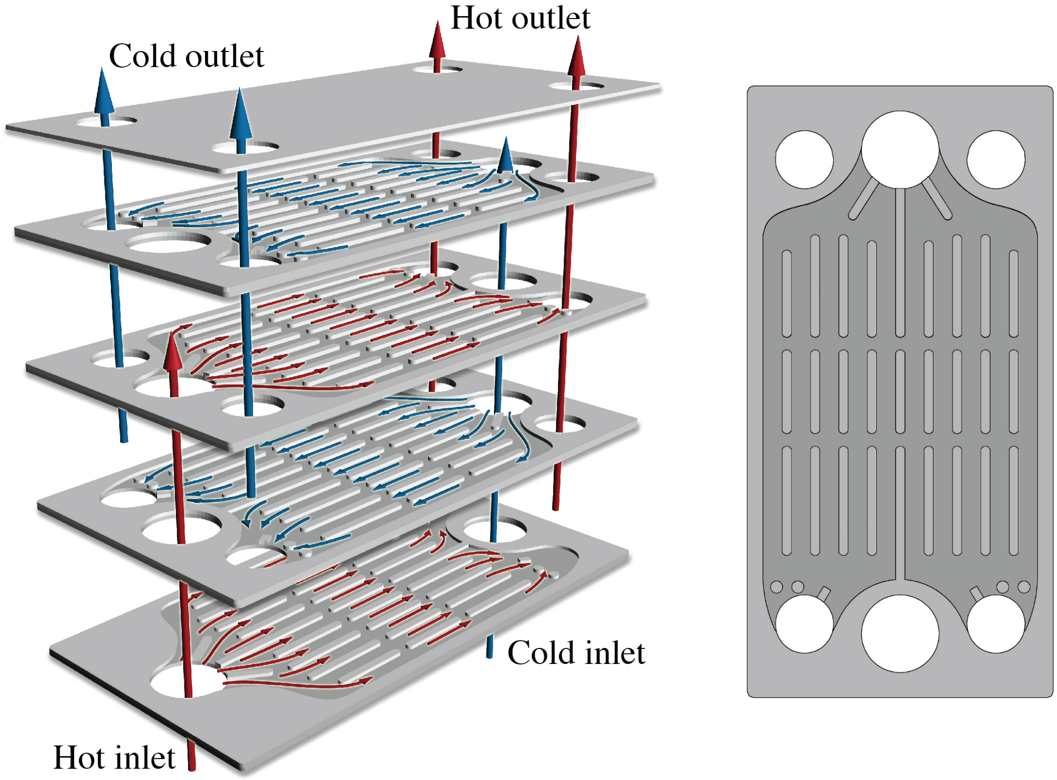

Figure 2.1: An exploded view of a 4-layer HEX-reactor (left) showing two independent flow channels and a single slide (right) detailing internal flow geometry.

Table 2.1: Heat exchanger / reactor physical parameters

Parameter	Value	Units
Overall dimensions	$100 \times 50 \times 7.42$	mm
Approximate channel dimensions	$60 \times 3.0 \times 0.7$	mm
Single layer volume	1.6599×10^{-6}	m^3
Single layer reactive surface area	2.7296×10^{-3}	m^2

the catalyst (if operating as a catalytic reactor), and to support the plate above during the compression and firing process. Without these structures, when the reactor is fired under pressure, the layers have the potential to deform and delaminate, destroying the sealing between flow channels. This is also the purpose of the small post features near the outlet ports. While these geometric features are necessary for proper manufacturing, they represent a flow impediment with potential performance penalties. This issue will be investigated further in Section 2.4.

The following sections will lay out the development of a series of purpose driven 3D CFD models of the HEX-reactor described. These models will be validated against experimental data collected at the Colorado Fuel Cell Center (CFCC) on a series of HEX-reactors manufactured in house and at CoorsTek. The models can then be used to further the understanding of the experimental data and assist in accounting for unknowns in the experimental apparatus. Further, the models can be expanded to include complex chemical kinetics coupled with the 3D CFD problem to gain insight into internal thermochemical conditions not accessible during experiment.

2.1 Fluid dynamics model

The development of the 3D CFD model is motivated by three goals: Create a model that can be validated against experimental results and then be used to analyze internal thermal and chemical conditions, explore thermal performance effects of manifolding used in experimental setup, and investigate geometric effects on thermal and chemical performance.

Pursuant to these goals, three models were created. The first is a direct representation of the nominal 4-layer design as shown in Figure 2.1. This model is validated against experimental thermal results collected by the author and Berkeley Hippel at the CFCC [17]. The second model includes stainless steel manifolding used to support the HEX-reactor and supply reactive and backing flow during experiments. This model is fit and validated against experimental data collected by Dr. Murphy also in the CFCC [52]. The third model is a reduced model based on reactor symmetries. The reduced model is valuable for its numerical efficiency when only the internal channel flow is of interest as opposed to the edge or manifolding effects. This is especially true for transient simulations with detailed chemical kinetics discussed in Chapter 3. Visual overviews of the three models are presented in Figure 2.2.

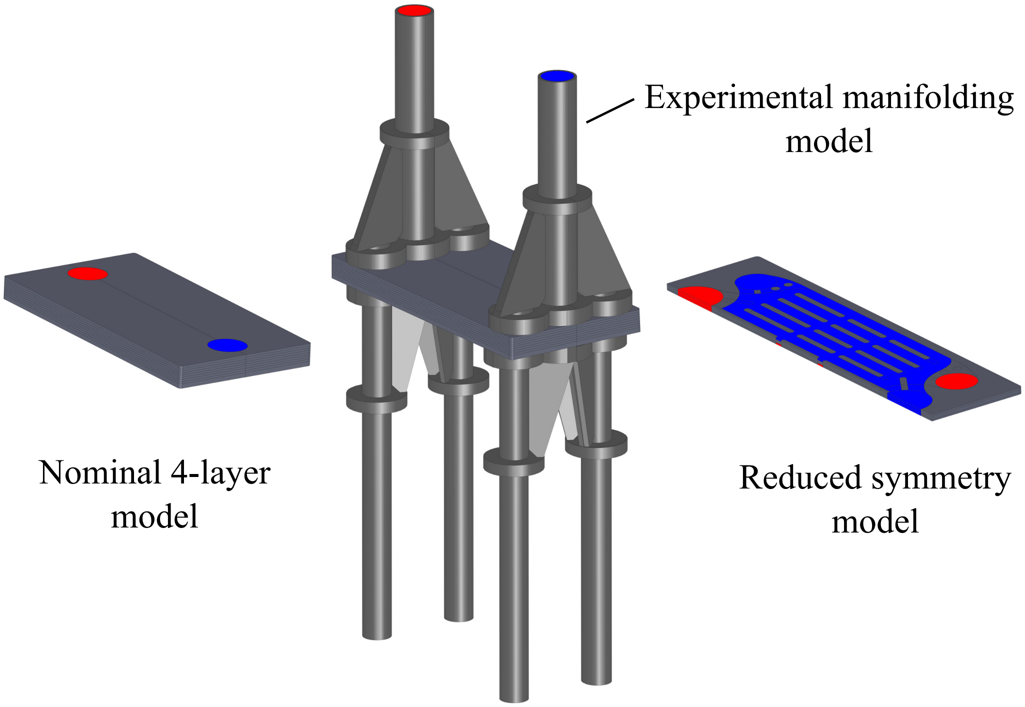

Figure 2.2: View of three reactor models used in this investigation. The nominal 4-layer design, the 4-layer design with stainless steel manifolding, and the symmetry reduced model are shown from left to right, respectively.

2.1.1 Meshing

In any CFD model, meshing is a critical component affecting the speed, and thus the utility, of the model as well as its accuracy. Meshing microchannel reactors presents a unique problem. In order to accurately capture the flow, and consequently the convective heat transfer, within the microchannels a sufficiently fine mesh is needed. Applying such a sufficiently fine mesh over the entire geometry, including in the solid body where only thermal conduction is being considered, can result in an exceedingly large mesh with accordingly long simulation run times. This problem of bridging areas that require small control volumes to those that don't is often done with a variety of mesh inflation techniques. The small, intricate features in a microchannel reactor are problematic for these techniques. The close proximity between one millimeter-scale geometric feature and the next does not leave much room for expansions techniques to do much good. Additionally, chasing down bad or degenerate control volumes that result from these meshing techniques is very time consuming.

Fortunately, this particular HEX-reactor geometry lends itself well to a meshing method known as 'coopering' or swept face meshing [53, 54]. Because of the way this heat exchanger was designed, every layer is either an exact copy of a lower layer or an exact copy rotated 180°. As such, every element on each layer, solid or fluid, exists on every other layer as well. In effect, the geometry can be collapsed to a series of 2D faces that capture every element in the 3D geometry. Figure 2.3 shows all the features of the HEX-reactor projected onto a plane. By meshing each face element with a quadrilateral mesh, the size and skewness can be tightly controlled and appropriately conform to each geometric element. Notice that geometric elements that contain fluid control volumes (though they may not on every layer of the HEX-reactor) have a relatively fine mesh, while elements like the external reactor body that are always solid body material are meshed more coarsely. Internal ribs that are also always solid are meshed at comparable resolution to flow channels. This is due to the fact that any inflation or expansion scheme would likely not give any benefit in the amount of space available.

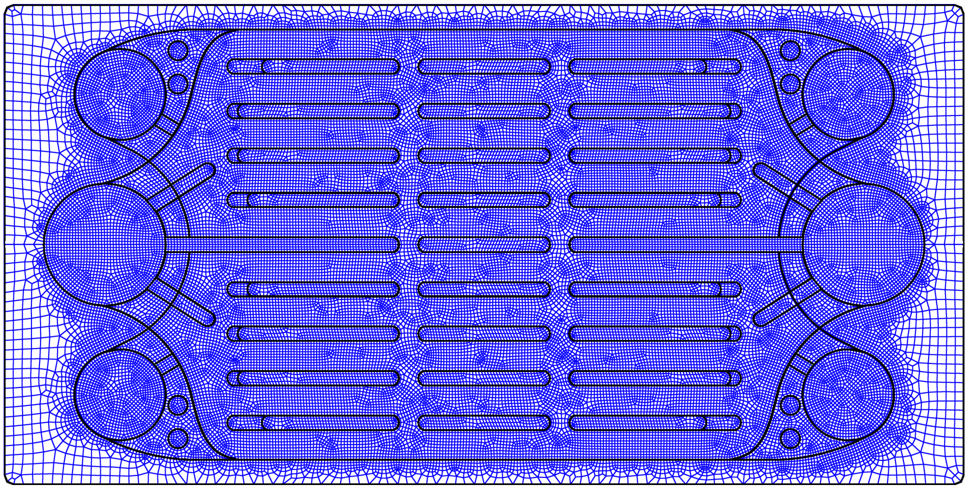

Figure 2.3: Detailed view of the collapsed HEX-reactor geometry with a 2D face mesh.

Once a satisfactory face mesh is generated, it can then be 'extruded' in the third dimension into the HEX-reactor body and flow channels. At defined intervals, the face 'extrusion' is cut to create control volumes. The original face mesh remains unchanged through the extrusion ensuring the quality of control volumes is maintained. Figure 2.4 gives a detailed view of extruded mesh covering all solid and flow layers. For the nominal 4-layer model and the manifolding model, the top and bottom alumina plates have no flow channels and can therefore be meshed relatively coarsely. By controlling the number of cuts in the extruded mesh, the number of control volumes that span the height of the flow channels (and the solid separator layers) can be tightly controlled. The resulting mesh is highly efficient and rarely requires manual effort to clean up degenerate or highly skewed cells.

The meshing scheme described here is applied to all of the models illustrated in Figure 2.2. For the manifolding model, a standard tetrahedral mesh is used to discretize the manifolding geometry. Flow within the manifolding is also meshed using tetrahedral volumes with inflation layers at the solid-fluid interface.

All reactor models were meshed in ANSYS Gambit. The nominal 4-layer design required approximately 1.5 million control volumes while the manifolded geometry required approximately 1.6 million and the symmetry reduced model only 400,000. The CFD solutions

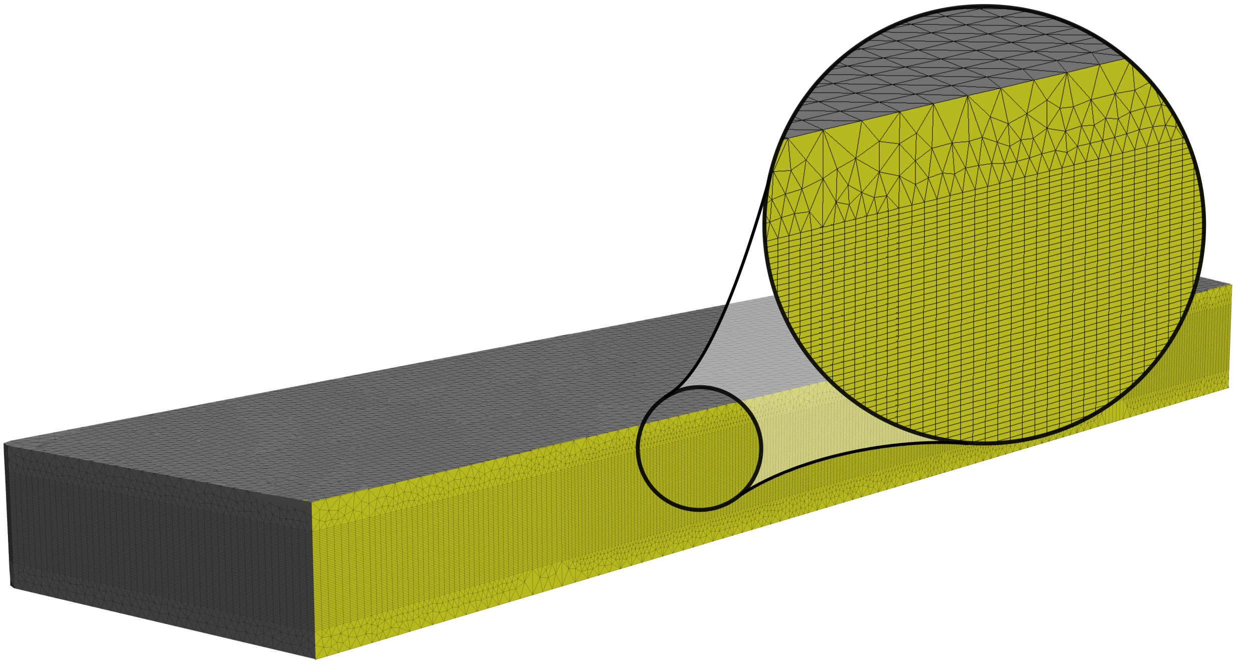

Figure 2.4: Detailed view of 4-layer reactor mesh. Internal flow and separation layers use the extruded mesh while external, solid alumina layers are meshes with tetrahedral volumes.

generated for the following analyses where done in ANSYS Fluent.

2.1.2 Mesh independence study

The accuracy of computational fluid dynamics simulations can be dependent on the size of the control volume mesh on which the equations of flow are resolved. The validity of any CFD model therefore depends on demonstrating that the solution is independent of the mesh size. In order to ensure that the meshes used in this work were of sufficient resolution, a set of models with constant boundary conditions and varying mesh sizes were compared. Any change in the solution between simulations indicates that the solution is not mesh independent. For this study, two comparative parameters were chosen, pressure drop across the reactor as a whole, and the maximum velocity observed in the microchannels. These parameters where chosen as their values come as a consequence of many other variables and flow conditions. As such, they represent global measures of a solution and can be relied on to sensitively measure variance between models. The parameters with which each trial was run are summarized in Table 2.2.

Table 2.2: Mesh independence study parameters

Parameter	Value	Units
Air temperature (T)	300	K
Mass flow rate ($\dot{m}$)	60	SLPM
Average mesh element size		
Trial 1	1.0×10^{-3}	m
Trial 2	8.0×10^{-4}	m
Trial 3	4.0×10^{-4}	m
Trial 4	2.0×10^{-4}	m

Figure 2.5 plots the predicted pressure drop across the HEX-reactor for a simple, non-reactive flow case. 60 SLPM of air at room temperature is driven through one side of the nominal 4-layer design. The average mesh element size is varied from 1 mm to 0.2 mm (this length indicates an average edge dimension of a 3D control volume element). Note, this length scale does not characterize all the control volume elements; Elements within flow channels tend to be smaller while elements in the solid body are larger. The average mesh

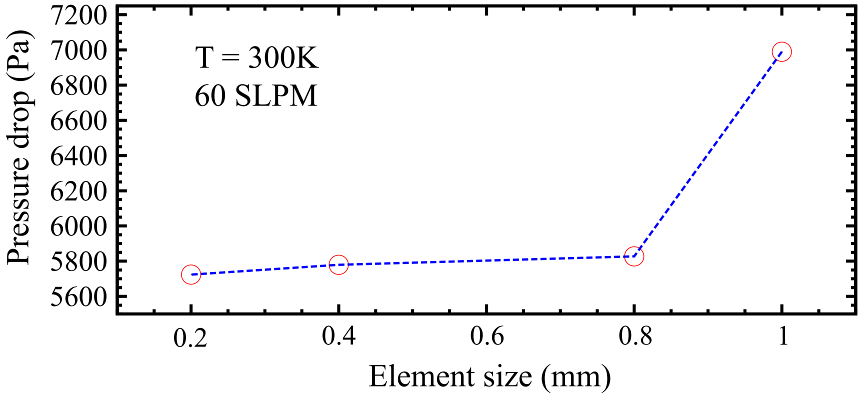

Figure 2.5: Pressure drop across a single microchannel layer as a function of average mesh element size. The flow considered is 60 SLPM at 300 K. The pressure drop appears largely unchanged for mesh sizes below 0.8 mm

element size is simply an average across the whole model. It is apparent in Figure 2.5 that for average element sizes above 0.8 mm, the predicted pressure drop deviates significantly from those predicted by mesh sizes below 0.8 mm. The solution at an average mesh element size of 1.0 mm shows a roughly 20% increase over the solution at 0.8 mm. This indicates that meshes above 0.8 mm are too coarse to properly capture the flow.

Figure 2.6 corroborates the pressure results. The maximum predicted velocity shows negligible variation below 0.8 mm but shows a roughly 6% difference at 1.0 mm.

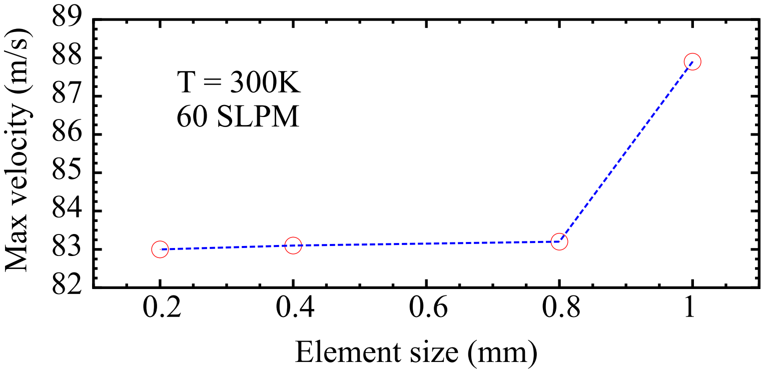

Figure 2.6: Maximum predicted velocity within a single microchannel layer as a function of average mesh element size. The flow considered is 60 SLPM at 300 K. The solution appears unchanged for mesh sizes below 0.8 mm

In the case of chemically reactive simulations, mesh independence for the fluid dynamics solution is considered sufficient for the kinetic solution. The diffusion length scales within microchannels are small by design and very little variation in species concentrations exists across channel dimensions. Therefore, the constraints for mesh independence for the hydraulic solution are considered to be more strict than those for the chemical solution. As such, for all following studies an average mesh element size of 0.8 mm or smaller is used to ensure solutions are mesh independent.

2.1.3 Thermophysical properties

Accurately capturing the thermal performance of the reactor is key to understanding its capabilities as a heat exchanger and fuel reformer. As will be discussed further in Section 2.2, for compact heat exchanger configurations, axial conduction along the direction of flow, especially for counterflow configurations, can play a significant role in thermal performance [55]. Additionally, as the reactor will experience large temperature gradients, the temperature dependence of the physical properties of 94% alumina are important. The manufacturer specifies the thermal conductivity of the 94% alumina as 22.4 W m^{-1} K^{-1} at 20 °C [51], but no temperature dependence is provided. In order to capture the temperature dependence, the average behavior of polycrystalline alumina was fit to the known data point from the manufacturer. Figure 2.7 illustrates the thermal conductivity of aluminum oxide as a function of temperature collected by Powell et al. from over 100 experimental measurements [56]. The blue line is the best fit and recommended relationship for 99.5% alumina. The red symbol indicates the single known point for CoorsTek 94% alumina.

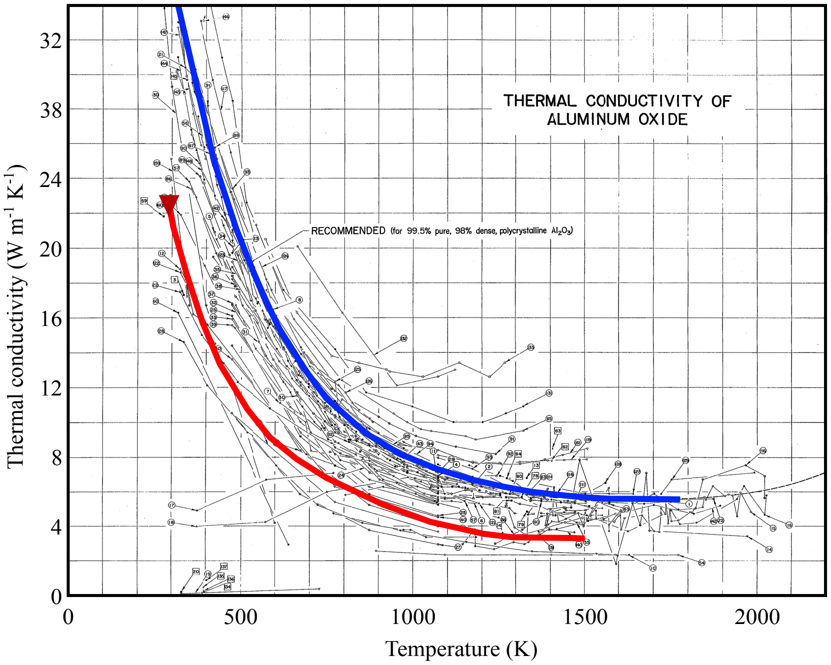

Figure 2.7: Compiled experimental measurements of thermal conductivity of alumina at various temperatures [56]. The blue line highlights the average for 99.5% alumina. The symbol marks the single known measurement for 94% alumina available from the manufacturer. The red line indicates the temperature dependence relationship used for 94% alumina.

The red line is the same behavior as that measured for 99.5% alumina but translated to the known point for 94% alumina. This relationship for the thermal conductivity as a function of temperature $\lambda(T)$ is described by the polynomial

$$\begin{aligned}\lambda(T) = &+ 72.355\\ &- 2.8985 \times 10^{-1}\ T\\ &+ 5.3742 \times 10^{-4}\ T^2\\ &- 5.1573 \times 10^{-7}\ T^3\\ &+ 2.4688 \times 10^{-10}\ T^4\\ &- 4.6442 \times 10^{-14}\ T^5 \qquad [\mathrm{W\ m^{-1}\ K^{-1}}]\end{aligned} \tag{2.1}$$

This relationship will be used for all reactor models.

The temperature dependence of the thermal capacity of 94% alumina is acquired by the same method. Ginnings et al. measured the thermal capacity of α-alumina over a range of temperatures, the results of which are shown in Figure 2.8 [57]. The temperature dependent behavior is then fit to the manufactures specification for the thermal capacity of 94% alumina, shown in the figure as the single symbol. The temperature dependent relationship for the heat capacity for 94% alumina $c_p(T)$ is modeled as

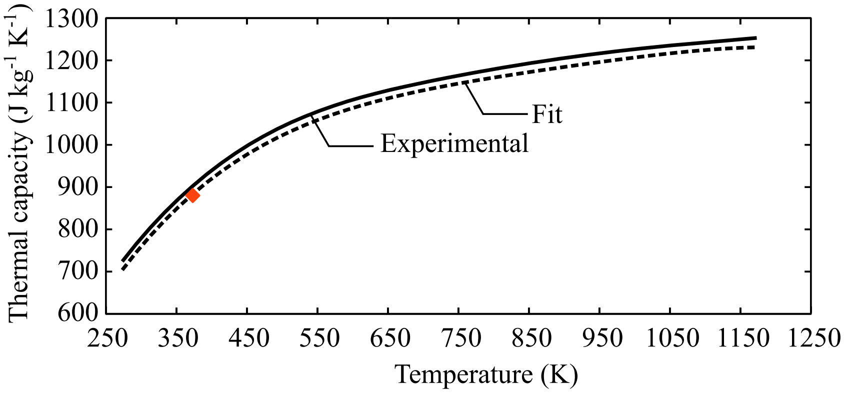

Figure 2.8: Experimental results for the thermal capacity of α-alumina (solid line) with the temperature dependence fit (dashed line) to the manufacturer's specification of thermal capacity (symbol) for 94% alumina.

$$\begin{aligned} c_p(T) = &- 330.0 \\ &+ 5.7861\ T \\ &- 8.9789 \times 10^{-3}\ T^2 \\ &+ 6.5388 \times 10^{-6}\ T^3 \\ &- 1.8093 \times 10^{-9}\ T^4 \qquad [\mathrm{J\ kg^{-1}\ K^{-1}}] \end{aligned} \tag{2.2}$$

The various gases used in the following studies (i.e., $H_2O(g)$, H_2, O_2, CH_4, CO_2, CO, and N_2) are modeled as incompressible ideal gases with temperature dependent properties when possible. A summary of the temperature dependent properties of all the gases used can be found in Appendix B.

2.1.4 Flow simulation considerations

All following simulations consider the internal flow to be laminar. The onset for the transition to turbulent flow is considered to be at a Reynolds number of Re = 2300. Considering the channel dimensions listed in Table 2.1, nitrogen at 25 °C will remain laminar within the microchannels up to approximately 84.5 SLPM. At elevated temperatures where gas viscosities are higher, for example 500 °C, transition to turbulence begins at 155 SLPM. All cases are either run well below those thresholds or at elevated temperatures and thus a laminar flow assumption is justified.

This analysis is slightly complicated by the reduced cross sectional area at the entrance to the microchannel layer. The higher velocity flow in this region will likely transition to turbulent at much lower flow rates than the flow in the microchannels in the center of the HEX-reactor. While this will be a source of error at higher flow rates, it is expected to not play a significant role at the flow rates considered. The flow will quickly transition to laminar in the small hydraulic diameter microchannels. The accuracy of this assumption is discussed further below.

2.1.5 Model validation

An important aspect of any model development process is model validation. For a model to claim any predictive capability it must demonstrate agreement with empirical observations. Two separate comparisons between model predictions and experimental measurements were made. The first compares the pressure drop across the reactor as a whole. Internal velocity and pressure information is not accessible in experiment so the overall pressure drop serves as a validation that the model is accurately capturing the flow characteristics within the microchannel. The second case compares the thermal performance of the HEX-reactor at high temperature and varied flow rates to model predictions. This comparison is intended to validate the conjugate heat transfer aspect of the HEX-reactor.

The experimental data were collected in the CFCC by fixing a 4-layer HEX-reactor to pressurized shop air controlled by an Alicat Scientific MCR-500SLPM mass flow controller (MFC). Pressure data were recorded at the MFC. For the high temperature experiments, the inlet air for the hot side is pre-heated with a series split-tube electric furnace. Temperatures were measured directly at the inlets to the HEX-reactor via thermocouples and recorded using LabVIEW. Thermal losses were minimized by mounting the HEX-reactor immediately after the furnace and wrapping the whole fixture in fiberglass mat and rope.

Figure 2.9 plots non-reactive, room temperature (30 °C) experimental measurements of pressure drop across a single 4-layer reactive channel. The microchannel heat exchanger produces approximately 33 kPa of pressure drop at 175 SLPM, the maximum flow measured. The superlinear behavior of pressure drop becomes apparent for flows greater than 80 SLPM.

Figure 2.9 also shows the model predicted pressure drop. The model and experimental results are broadly in good agreement over the whole range of tested flow rates, but do show some deviation at flows above approximately 100 SLPM. This is due to flows likely transitioning to turbulent within the microchannels at higher flow rates. Turbulent flow tends to increase pressure drop for a given mass flow rate. The model is simulated as laminar flow which will under predict pressure drop at high flow rates. Nevertheless, all experiments and

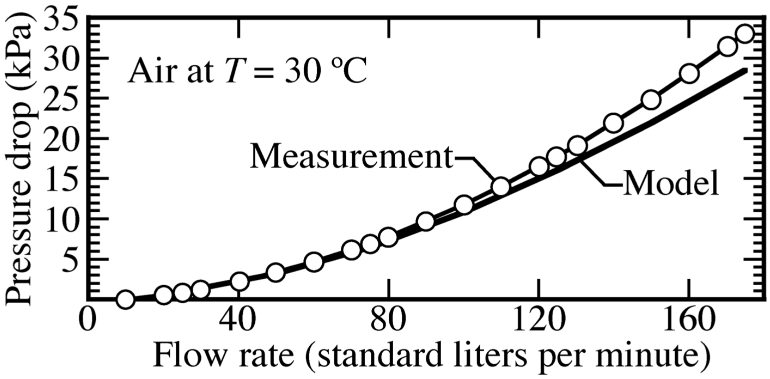

Figure 2.9: A comparison of model predicted (lines) pressure drop across the four-layer heat exchanger and experimentally measured pressure drop (symbols).

analysis discussed later are considered for operating conditions below 100 SLPM.

The more telling, and arguably more important, comparison is the thermal performance of the reactor. Figure 2.10 shows the inlet and outlet temperatures as measured by experiment for the reactor under non-reacting conditions. The backing-side flow rate is fixed at 80 SLPM and 700 °C while the cold-side flow rate is varied from 60 SLPM to 100 SLPM. The cold-side flow enters the manifolding at room temperature. Also reported on Figure 2.10 is the equivalent gas hourly space velocity (GHSV) for the cold-side flow. GHSV is calculated as

$$\mathrm{GHSV} = \frac{\dot{V}}{V} \tag{2.3}$$

where $\dot{V}$ is the volumetric flow rate and V the reactor volume. This is essentially the reactor volume turnover rate per hour.

The lines in Figure 2.10 represent model predictions of pressure drop for the nominal 4-layer design simulated with the same flow conditions as the experiment. The two are in good agreement over the whole range of cold-side flow rates considered. While precautions were taken in the experiment to limit stray heat loss to the environment, some loss was inevitable. To account for this, a small heat loss was applied to the external surfaces of the HEX-reactor model in the form of a heat transfer coefficient and ambient temperature. It was found the best fit came from a heat transfer coefficient of $h = 4.5$ W m^{-2} K^{-1}

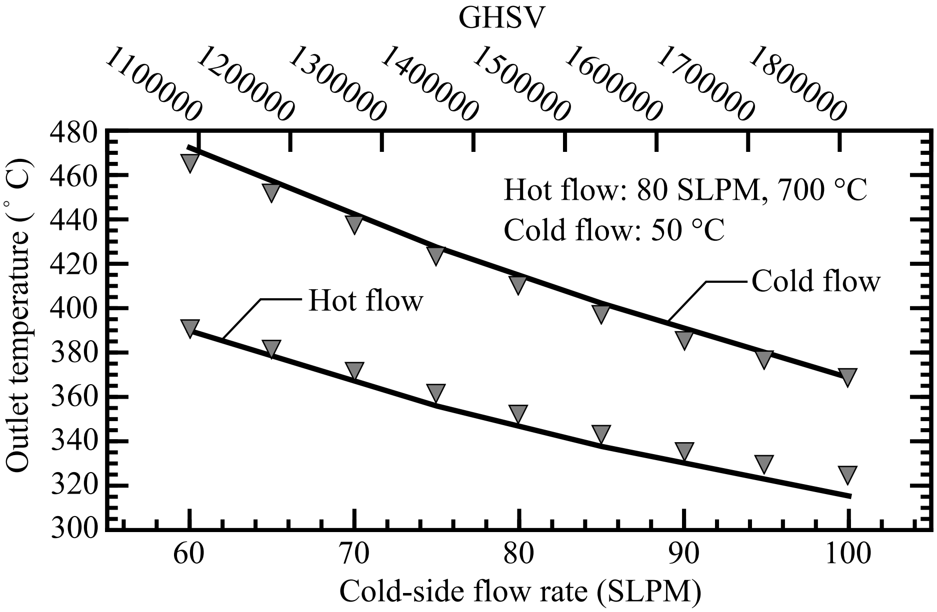

Figure 2.10: Inert flow outlet temperatures of the nominal 4-layer HEX-reactor as measured by experiment compared with model predictions. Experiment (symbols) and model (lines) were run with a backing-side flow rate and temperature of 80 SLPM at 700 °C.

with ambient temperature considered to be $T_{\text{amb}} = 27$ °C. Of the total amount of thermal energy transferred from the hot flow to the cold flow, the loss to the environment represents approximately 2.5%.

Ultimately, Figure 2.9 and Figure 2.10 provide solid validation for the fluid and conjugate heat transfer models developed. Further analysis can be done with confidence.

2.2 Thermophysical properties investigation

The choice of alumina for the HEX-reactor body has several advantages. The process of green machining or pressing flow channels into the pre-fired plates is well suited for fast and inexpensive manufacturing. Additionally, the raw material costs of alumina is highly advantageous with respect to metal analogues. As discussed previously, alumina is also well suited to operate at high temperatures where metals commonly used in heat exchangers (e.g., copper, aluminum, steel [7]) cannot. On the other hand ceramics tend to have lower thermal conductivity than most of those same metals. Figure 2.11 plots the thermal conductivity of various common metals used in heat exchanger construction at a range of temperatures. Plotted for comparison are alumina and cordierite. Cordierite which depending on manufacturing technique can have excellent thermal shock characteristics [58, 59] has a relatively low thermal conductivity (1.6 – 4 W m^{-1} K^{-1}). Another common option not plotted is silicon carbide which has a very high thermal conductivity in the range of 100 – 300 W m^{-1} K^{-1} [60].

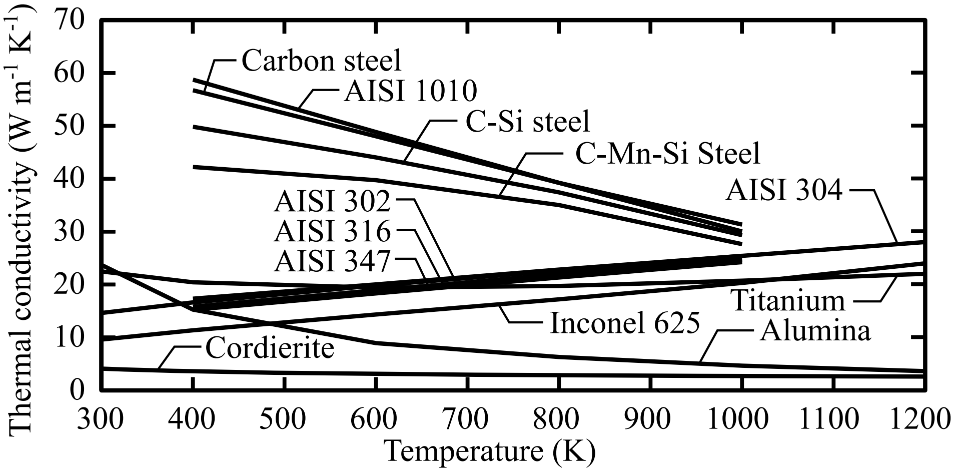

Figure 2.11: Thermal conductivity of various metals and cordierite compared to 94% alumina over a range of temperatures[61, 62, 63].

The thermal conductivity of the reactor material has a significant effect on the overall thermal performance. This is especially true for HEX-reactors in a counterflow configuration. Operating heat-exchangers in a counterflow fashion tends to produce large thermal gradients across the flow axis of the exchanger body which contributes to higher heat transfer between flows and therefore higher effectiveness [8]. One complication that arises in this configuration is that higher thermal conductivity materials tend to increase heat transfer through the solid material in the direction of the flow as well as perpendicular between flows. This axial conduction tends to degrade the thermal gradient across the reactor and reduce the overall thermal performance. On the other hand, low thermal conductivity will increase the thermal resistance to heat transfer between flows. A balance must be struck between these two competing effects.

What follows is a study of the effect of the solid body thermal conductivity on the overall performance of the HEX-reactor. In order to explore this effect for this particular design, the thermal conductivity of the HEX-reactor body material was varied between 1.0 and 150 W m^{-1} K^{-1} and the predicted non-reactive heat exchanger effectiveness was recorded. The effectiveness ϵ is measured as the total amount of heat transfer between flows $\dot{Q}$ compared to the maximum possible heat transfer $\dot{Q}_{\mathrm{max}}$ given the inlet conditions, or

$$\epsilon = \frac{\dot{Q}}{\dot{Q}_{\mathrm{max}}}. \tag{2.4}$$

The maximum heat transfer $\dot{Q}_{\mathrm{max}}$ is calculated as

$$\dot{Q}_{\mathrm{max}} = C_{\mathrm{p,min}}(T_{\mathrm{hot,i}} - T_{\mathrm{cold,i}}) \tag{2.5}$$

where $T_{\mathrm{hot,i}}$ and $T_{\mathrm{cold,i}}$ are the hot and cold inlet temperatures, respectively. $C_{\mathrm{p,min}}$ is the minimum heat capacity rate between the two inlet flows or

$$C_{\mathrm{p,min}} = \mathrm{MIN}\left(\dot{m}_{\mathrm{hot}} C_{\mathrm{p,hot}},\ \dot{m}_{\mathrm{cold}} C_{\mathrm{p,cold}}\right). \tag{2.6}$$

Figure 2.12 shows the predicted effectiveness of the HEX-reactor running under balanced flow for a range of solid body material thermal conductivities. Three flow conditions are plotted: 25 SLPM (GHSV $\approx 450,000$ h^{-1}), 50 SLPM, and 100 SLPM. All cases had cold flow entering at 40 °C and hot flow entering at 500 °C. The three cases show an optimum value for thermal conductivity in terms of maximizing the effectiveness, though the higher flow case is less pronounced. The 25 SLPM case indicates an optimum thermal conductivity at approximately $\lambda = 5$ W m^{-1} K^{-1} while the 50 SLPM case has an optimum around 15 W m^{-1} K^{-1}. The optimum for the 100 SLPM case is less apparent but occurs around 40 W m^{-1} K^{-1}. Figure 2.12 suggests that for high-flow conditions in this microchannel reformer, the body material thermal conductivity does not play a significant role with the difference in effectiveness between the optimum and that at 150 W m^{-1} K^{-1} being only a few percent. The exception of course is for $\lambda < 10$ W m^{-1} K^{-1} where transverse heat conduction between flows is inhibited. For lower flow scenarios, on the other hand, the effect is large and can be a significant factor in heat exchanger performance. For low flow cases, lower thermal conductivity, to a point, tends to produce higher overall effectiveness. The difference between the optimum and the minimum predicted effectiveness is greater than 10% for the 25 SLPM case.

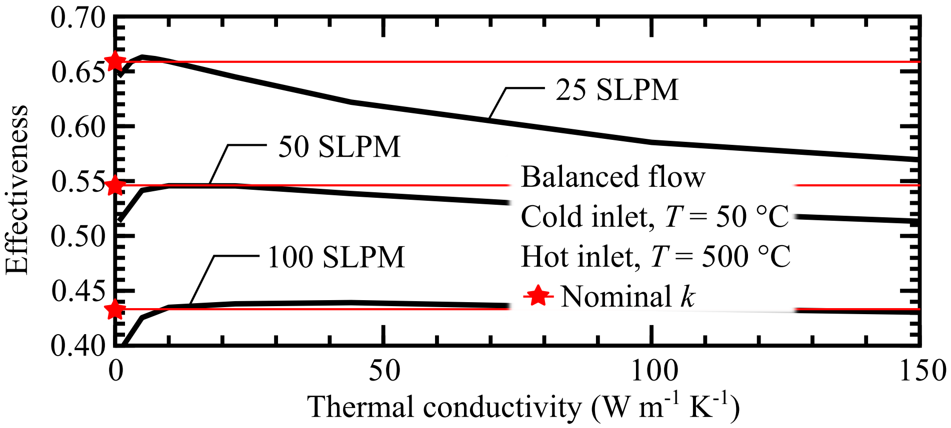

Figure 2.12: Predicted heat exchanger effectiveness as a function of solid body thermal conductivity. Three cases were considered, 25 SLPM, 50 SLPM, and 100 SLPM. The red symbols and lines represent the HEX-reactor performance at nominal thermal conductivity for comparison.

Also plotted in red are the nominal operating points using the 94% alumina thermal properties discussed in Section 2.1.3. The relatively low thermal conductivity of alumina at elevated temperatures (see Figure 2.11) places it near the optima for the flows tested.

It should be noted that the results in Figure 2.12 are specific to the current HEX-reactor design. Changes in design that, for example, enlarge or shrink the ribs in the flow channels or reduce the floor thickness between flow channels will change the axial cross-sectional area available for conduction. These geometric features will increase (enlarged cross-sectional area) or decrease (reduced cross-sectional area) the effect λ has on overall effectiveness.

2.3 Thermal performance

Studying the performance of any device in isolation is useful for understanding its inherent characteristics and improving its design. Though in any practical application, as is surely the case with the HEX-reactor in question, the effects of the supporting hardware must be considered. This is especially true for high temperature applications where large temperature differences can exist between different pieces of equipment in the system. As mentioned previously in Section 2.1, the experimental setup used in testing the HEX-reactor included stainless steel manifolding for supporting and supplying the HEX-rector with reactant flow and carrying away reformate gases. These manifolding structures clamp the HEX-reactor under spring pressure to provide a good seal on the mica intermediate material [52]. The contact area between the steel manifolding and alumina HEX-reactor body is relatively large as flanges are added (cf., Figure 2.2) to ensure the clamping pressure does not induce significant bending stress in the ceramic material. This large contact area provides low thermal resistance to conduction along the manifolding away from the HEX-reactor and can have an appreciable effect on the thermal and chemical performance of the HEX-reactor. In any embedded application, the design of the manifolding may be different from the setup used by Murphy [52], but the effects will nevertheless need to be accounted for.

Experimental data on the thermal performance of the reactor while mounted in its manifolding were collected by Murphy at the CFCC [52]. Temperature data was collected at the inlet ports to the ceramic heat exchanger. The CFD model with incorporated steel manifolding was run under the same conditions. The difference in this case is that the boundary conditions for the inlet flows are applied not at the HEX-reactor ports, but at the entrance to the manifolding. As in the validation experiments in Section 2.1.5, a heat transfer coefficient was applied to the outer surfaces of the HEX-reactor and the steel manifolding and varied to find the best fit for the experimental data. It was found that a heat transfer coefficient of $h = 4.5$ W m^{-2} K^{-1} with ambient temperature considered to be $T_{\text{amb}} = 27$ °C provided a very good fit. These are the same conditions that provided a good fit for the validation case where manifolding was not a large factor. An example 3D solution, with boundary conditions identified is shown in Figure 2.13. The hot side enters at 50 SLPM and 700 °C with the cold side flowing at 2.0 SLPM at 25 °C. It is clear that at these conditions, the

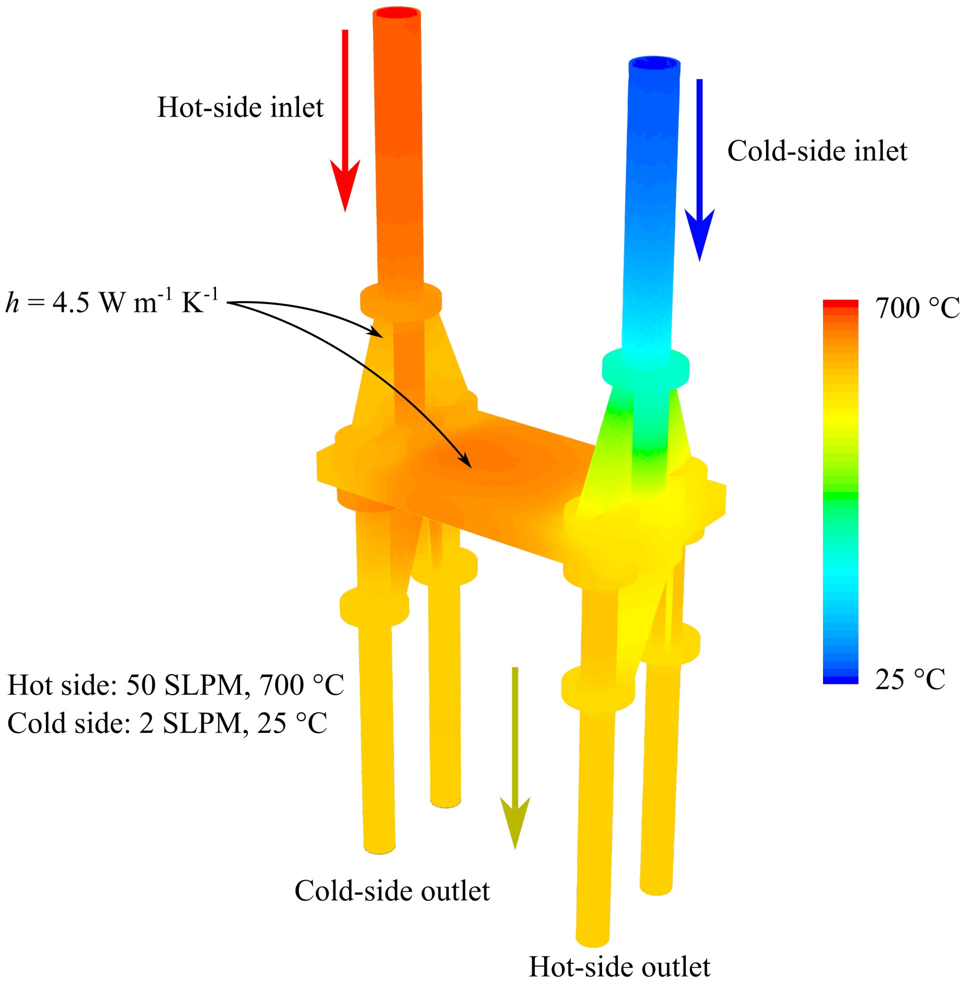

Figure 2.13: Surface temperature contour for the HEX-reactor with stainless steel manifolding included. This particular solution is for a hot-side flow rate of 50 SLPM at 700 °C and a cold-side flow rate of 2.0 SLPM at 25 °C.

hot flow dominates the overall temperature of the assembly. What is also clear is that a significant amount of pre-heating takes place on the cold side inlet prior to the flow reaching the HEX-reactor inlet.

Exploring this further, the model was simulated for each of the operating points measured by experiment. Furthermore the HEX-reactor was simulated with the effects of the manifolding negated as a benchmark for comparison. Figure 2.14 illustrates the results of that investigation. In Figure 2.14a, the inlet and outlet temperatures are reported for a range

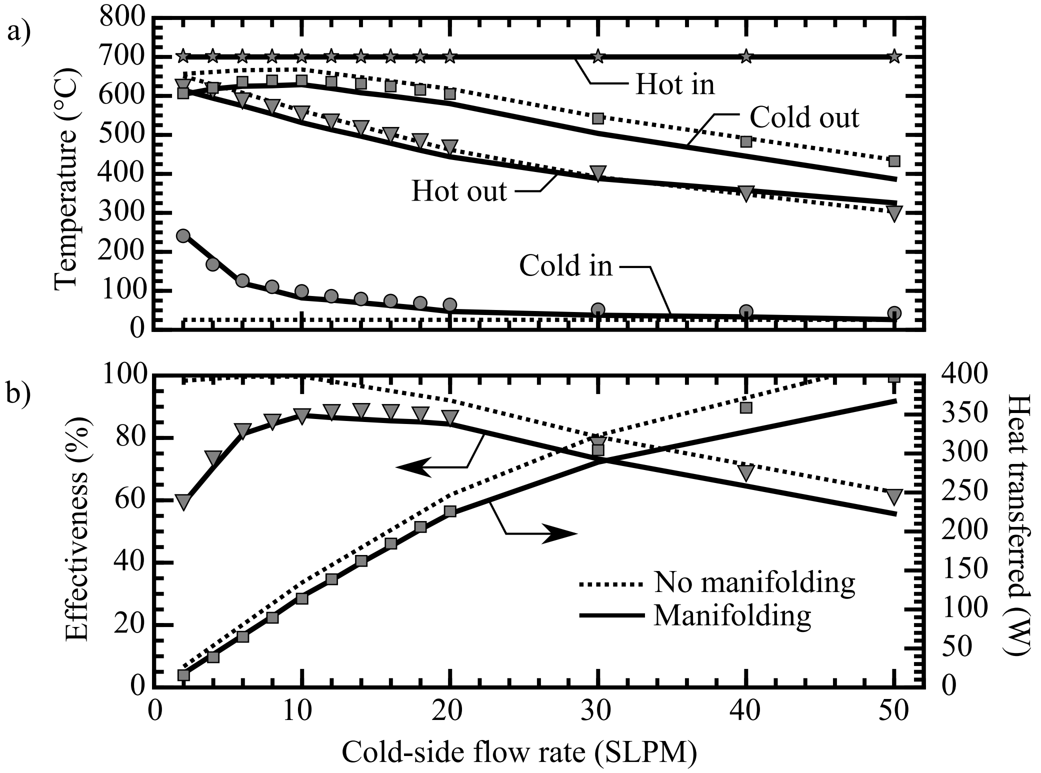

Figure 2.14: Comparison of thermal performance between experimental results and model predictions over a range of cold-side flow rates. Experimental data is marked by symbols, the manifolded model is marked by solid lines, and the non-manifolded model is marked by dashed lines. a) shows predicted and measured inlet and outlet temperatures for cold and hot flow. b) shows the heat exchanger effectiveness and heat transferred.

of cold-side flow rates. Three sets of data are plotted: Experimental temperature measurements, predicted temperatures based on the manifolded model, and predictions based on the HEX-reactor model with no manifolding. One thing to note is the very good agreement between the experimental data and the manifolded model. Not only does the model predict outlet temperature very closely, the effects of the manifolding on the inlet temperatures are also captured. For example, at low flow rates, thermal conduction through the manifolding from the relatively hot heat exchanger body heats the cold-side flow prior to reaching the inlet proper. This is why the measured cold-side inlet temperature is near 250 °C at 2 SLPM. At higher flow rates this effect is reduced as the thermal capacity of the cold flow increases. Obviously the non-manifolded model does not have this effect.

The most significant difference between the manifolded and non-manifolded predictions is a roughly 50 °C increase in cold-side outlet temperatures. This is likely due to the decrease in thermal losses to the environment from the manifolding surfaces. Figure 2.14b quantifies that more clearly by plotting the total amount of heat transferred (to the cold flow) and the overall heat exchanger effectiveness. It is important to note that for this study, the amount of heat transferred, for the purposes of calculating the effectiveness (see Equation 2.4), is considered to only be the amount transferred to the cold flow. This does not capture losses from the hot flow to the environment. This is why the non-manifolded model predicts near unity effectiveness at low cold-side flow rates. The non-manifolded model generally shows a ten percentage point increase in effectiveness and roughly 5 – 50 W increase in heat transferred depending on flow rate. This puts a range on the thermal losses to the environment due to manifolding effects.

2.4 Pressure performance

In any integrated system, and in the design of its components, the plant efficiency is a critical factor in its energetic and economic success. A common parasitic power loss is the pumping work associated with moving the working fluid through the system. The pressure drop across a flow device is therefore an important design consideration. The power associated with pressure drop in equipment (assuming an ideal pump) is [64]

$$W_{\text{pump}} = \frac{\dot{m}}{\rho}\Delta p \tag{2.7}$$

The pressure drop across a device is the result of both fluid and geometric parameters. Shah et al. [8] presented the following relations for the pressure drop across a heat exchanger for both turbulent and laminar flow:

$$\Delta p = \begin{cases} \dfrac{1}{D_h^3}\left[\dfrac{1}{2g_c}\dfrac{\mu}{\rho}\dfrac{(4L)^2}{A}\dot{m}(f\cdot\mathrm{Re})\right] & \text{for laminar flow} \\ \dfrac{1}{D_h^3}\left[\dfrac{0.046}{2g_c}\dfrac{\mu^{0.2}}{\rho}\dfrac{(4L)^{2.8}}{A^{1.8}}\dot{m}^{1.8}\right] & \text{for turbulent flow} \end{cases} \tag{2.8}$$

where D_h is the hydraulic diameter, g_c is a proportionality constant ($g_c = 1$ for SI units), μ is the fluid viscosity, ρ the fluid density, L the length of the heat exchanger flow channel, A the total heat transfer surface area, and $f \cdot \mathrm{Re}$ the Reynolds number friction factor. Depending on channel geometry, the heat exchanger pressure drop depends on hydraulic diameter as

$$\Delta p \propto \begin{cases} \dfrac{1}{D_h^3} \text{ to } \dfrac{1}{D_h^4} & \text{for laminar flow} \\ \dfrac{1}{D_h^3} \text{ to } \dfrac{1}{D_h^{4.8}} & \text{for turbulent flow} \end{cases} \tag{2.9}$$

For fully developed, internal, laminar flow the Nusselt number becomes a constant [61]. Comparing Equations 1.1 and 2.9, we see that microchannel HEX-reactors must strike a balance between improved heat transfer and hydraulic losses.

A fully resolved 3D model aids in analyzing the pressure performance of the HEX-reactor by allowing internal flow conditions to be studied. Figure 2.15 plots the internal predicted pressure of the HEX-reactor under non-reacting conditions, 50 SLPM balanced flow, the cold inlet flow at $T = 50$ °C, and the hot inlet at $T = 500$ °C. The x-axis is the position along the internal flow channels with the hot inlet and cold inlet appearing on the right and left side, respectively. It can be seen that the overall pressure drop for the cold side is approximately 5 kPa while the hot side, for the same mass flow rate, is nearer to 8 kPa. The difference between the two can be explained by the 450 °C temperature difference between the two inlet flows. At 500 °C nitrogen has approximately twice the viscosity and less than half the density as the cold side inlet at 50 °C. These factors, at least nearer the entrance of the flow channels before the flow temperatures equalize, supports the higher Δp.

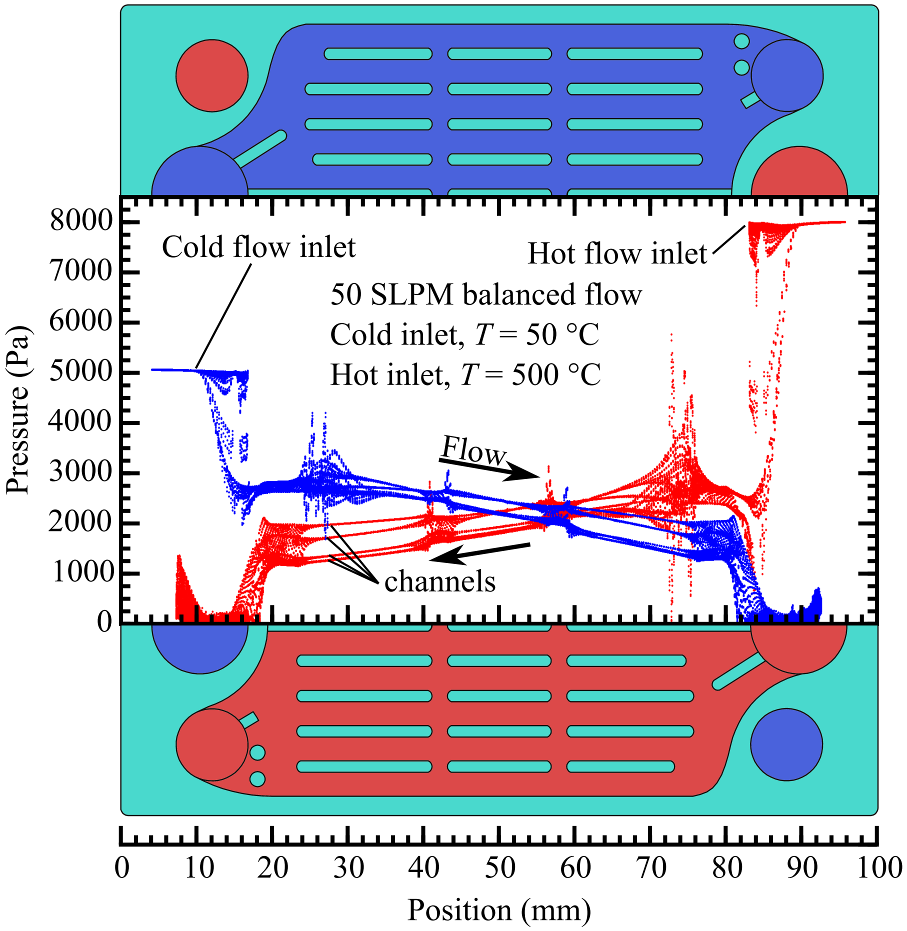

Figure 2.15: Predicted pressure within the microchannel heat exchanger under balanced flow conditions. Position within the HEX-reactor is plotted along the x-axis. The cold side flow entered at 50 °C and the hot side at 500 °C. Both sides had a mass flow rate of 50 SLPM.

Some important features beyond the overall pressure drop can be seen in Figure 2.15. One might notice first that by and large the most significant pressure drop for both flows, especially the hot flow, occurs immediately as the flow enters the microchannels from the supply tube. This is due to the significant constriction the microchannels present to the flow entering from the manifolding. Such a large pressure drop suggests that the nominal 4-layer design could benefit from more flow layers to reduce the mass flow rate through any one channel.

Inside the microchannels themselves, pressure losses roughly follow the linear trend one would expect for channel flow. The spikes apparent around 25, 40, 60, and 75 mm are due to flow impinging on the ends of the internal rib structures. Interestingly, despite the existence of gaps in the ribs to equalize flow, the separate channels still manage to support pressure variations between them, as noted on Figure 2.15, especially towards the exit ports. This is in part due to the momentum change required by flow in channels nearer to the center of the HEX-reactor to turn and exit the flow channel. It is also worth noting the pressure penalty paid for the small support structures near the exit port of either flow. These structures exist for manufacturing purposes. When laminating and sintering the alumina plates, pressure is required to ensure a good bond between layers. These structures support the above layer to prevent collapse. From a flow perspective they introduce a significant impediment to flow as evidenced by the roughly 2 kPa drop across those structures alone. While these supports are largely mandated by the pressure lamination manufacturing process for these HEX-reactors, perhaps future efforts to optimize the placement and shape of them could minimize their hydraulic penalty.

2.5 Internal reaction conditions

Whether using hot exhaust gases or catalytic partial oxidation (CPOX) to support the highly endothermic steam methane reforming (SMR), the energetic cost of maintaining ideal thermochemical conditions on the catalytically reactive surfaces has to be considered. To investigate this, the cold side of the HEX-reactor was supplied with 4 SLPM (GHSV ≈

$72,000\ \mathrm{h}^{-1}$) of nitrogen at 25 °C while the backing side mass flow rate and inlet temperature are varied from 10 – 100 SLPM and 600 – 900 °C, respectively. For each combination of boundary conditions, the average temperature and standard deviation of all internal reactive surfaces is recorded. These measures provide approximate conditions that would be present for internal SMR. While these numerical experiments are run under inert conditions, the thermal effects of SMR are discussed further in Section 2.6.1.

Figure 2.16 is a contour plot of the average predicted internal catalytic surface temperature. Over the whole operating space investigated the average reactive surface temperature ranged from approximately 460 to 860 °C. Intuitively, at low backing-side flow rates, the average reactive surface temperature is highly dependent on backing-side inlet conditions. Increasing the backing side flow shows diminishing returns though. The average reactive surface temperature $T_{\mathrm{s,avg}}$ shows decreasing dependence on the backing side flow rate as it approaches 50 SLPM, beyond which $T_{\mathrm{s,avg}}$ is largely independent on backing mass flow rate and depends only on backing inlet temperature. From an operational perspective, this suggests operating at or above 50 SLPM for these particular cold-side operating conditions is inefficient. Above 50 SLPM, $T_{\mathrm{s,avg}}$ tracks linearly with the backing side inlet temperature but cooler by approximately 27.5 °C over the whole range.

A typical operating temperature for SMR over rhodium is 750 °C. Highlighted on Figure 2.16 are the average temperature contours for 700 °C and 800 °C, bounding the nominal operating temperature.

One feature in Figure 2.16 that bears further explanation is the slight decrease in average surface temperature with increasing backing flow rate for a given backing flow temperature. The effect can be seen for flow rates greater than approximately 50 SLPM. The is a non-intuitive result as any increase in backing flow should either increase the reactive surface temperature or do nothing. The effect is small, only about 1% difference from 50 SLPM to 100 SLPM, and likely due to numerical errors arising from high velocities at the microchannel inlets as discussed in Section 2.1.5.

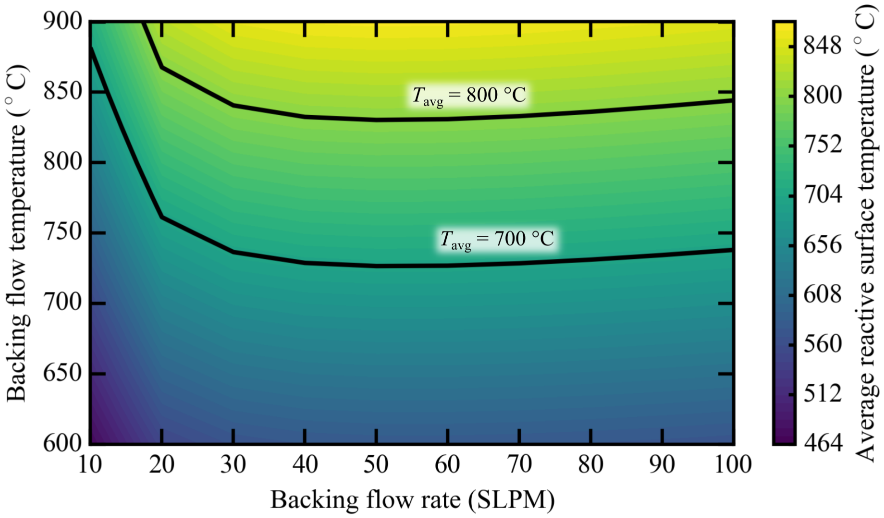

Figure 2.16: Contour plot showing the average reactive surface temperature over a range of backing side flow rates and inlet temperatures. The average temperature contours for 700 °C and 800 °C are highlighted. The reactive side was held constant at 4 SLPM and 25 °C.

The average reactive surface temperature is an important measure but does not characterize the spread of observed temperatures. Widely disparate reaction conditions can result in the same average temperature as a tightly controlled case. Figure 2.17 is the predicted standard deviation of the same temperature data collected for Figure 2.16. The standard deviation of the reactive surface temperature does not give maximum or minimum bounds but simply attempts to capture an approximate measure of the range of temperatures observed. As before, the 700 °C and 800 °C average surface temperature contours are highlighted to bound the nominal operating range.

Figure 2.17 illustrates one challenge with running a HEX-reactor in counterflow configurations. The temperature gradient across the reactor that facilitates high effectiveness factors also produces a range of reactive surface temperatures. It can be seen that even at high backing-side flow rates, a standard deviation of roughly 16 – 25 °C persists. For typical backing-side flow rates and temperatures used in this study and in the experimental data collected by Murphy et al. [52, 65], a standard deviation of approximately 50 °C is predicted.

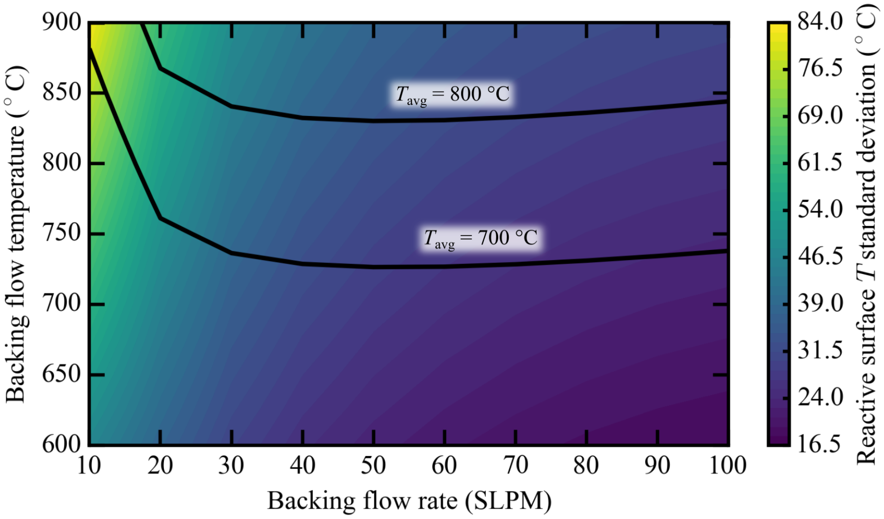

Figure 2.17: Contour plot showing the standard deviation of the reactive surface temperature over a range of backing side flow rates and inlet temperatures. The average temperature contours for 700 °C and 800 °C are highlighted. The reactive side was held constant at 4 SLPM and 25 °C.

2.6 Catalytic performance

To fully investigate the performance of the ceramic microchannel HEX-reactor, integrated catalytic chemistry is incorporated into the 3D CFD model. Details regarding the challenges and approach to incorporating detailed chemical kinetics are discussed in Chapter 3. For the following discussion, what is important is that the fluid-solid interfaces on the reactive flow channels are considered catalytically active. Species conservation equations are solved in the bulk flow and reactions are only considered on faces within the microchannels that are shared with solid body control volumes. The kinetics of SMR over rhodium are simulated using a 48-step kinetic mechanism developed by Karakaya et al. [66, 67]. The mechanism is summarized in Table 3.1.

As a case study in the catalytic performance of the HEX-reactor, the model boundary conditions were matched to the experimental conditions used by Murphy [65]. Namely, the backing side has a mass flow rate of 30 SLPM of nitrogen at 750 °C and the reactive side has a mass flow rate of 3.5 SLPM at 190 °C. The entrant gases for the reactive flow are steam and methane with a S/C = 2.5. In exploring the effect of reactive-side flow rate, a second case was run with double the flow rate, 7.0 SLPM, leaving all other boundary conditions the same.

Figure 2.18 presents the internal species mole fractions for the two simulated cases. Major species (i.e., H_2O, CH_4, and H_2) are plotted on the top graph with a detailed view of minor species (i.e., CO and CO_2) plotted on the bottom graph. An important note is that Figure 2.18 presents species mole fractions as a spatial average. Variations in species concentrations between channels at the same position along the axis of flow are subsumed into an average value. The fuel mixture enters the HEX-reactor on the left, reacts with catalytically active surfaces producing a hydrogen rich reformate, and exits at the right.

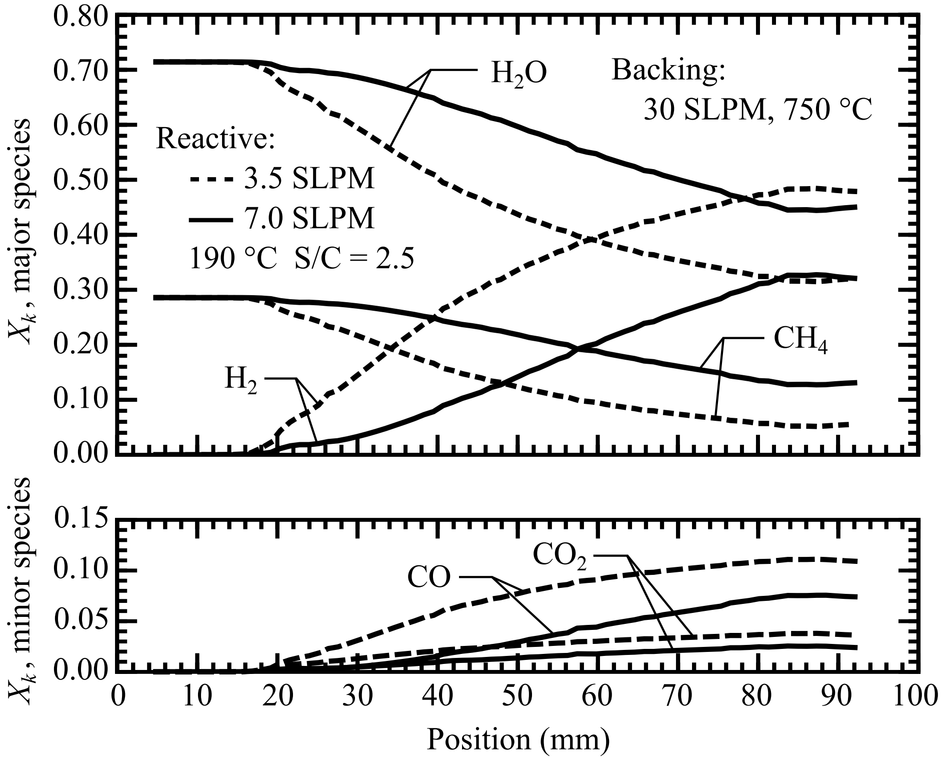

Figure 2.18: Species mole fractions as a function of position within the reactor microchannels. The backing side has a mass flow rate of 30 SLPM at 750 °C and the cold side enters at 190 °C. Two reactive side flow rates are shown, 3.5 SLPM and 7.0 SLPM, both with S/C = 2.5. Major species are plotted on the top graph and minor species are plotted on the bottom graph.

For the 3.5 SLPM case, methane conversion reaches approximately 73.8% and hydrogen yield approximately 60.0%. For the 7.0 SLPM case, the methane conversion drops to roughly 43.9% and hydrogen yield to 35.7%.

The spatially averaged species concentrations suggests fairly consistent H_2 production down the length of the channels. This is not entirely true. Figure 2.19 is a contour plot of H_2 production from the catalytically active surface within the microchannels. The contour solution is split. The top half represents the hydrogen production for the 3.5 SLPM reactive side mass flow rate, while the bottom represents the 7.0 SLPM case. What is clear is that for the low flow case, the majority of hydrogen production is done within the first third to half of the reactor. Doubling the flow rate to 7.0 SLPM shifts the localized hydrogen production and spreads it out more evenly across the channels with the majority covering the last two-thirds of the reactive channels.

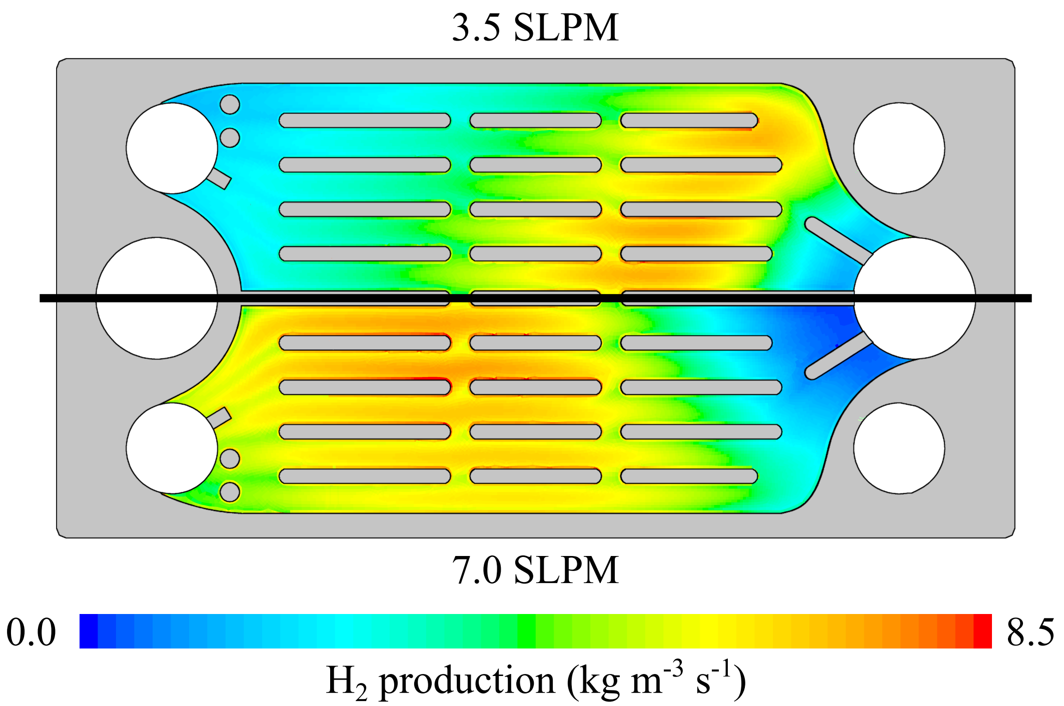

Figure 2.19: Contour plot of hydrogen production at the catalytically reactive surface Solutions for 3.5 SLPM (top) and 7.0 SLPM (bottom) reactive mass flow are shown. The direction of flow is from right to left.

Both cases show an uneven distribution of catalyst utilization between channels. Likely as a result of path length differences from one channel to the next and thermal variation as the fuel mixture enters the microchannels. The outer channels show markedly lower hydrogen production compared with channels nearer the center of the HEX-reactor. This result is complicated by the solutions displayed in Figure 2.20, which displays contours of H_2 mole percent. Again, the solution for the 3.5 SLPM and 7.0 SLPM case are shown on top and bottom, respectively.

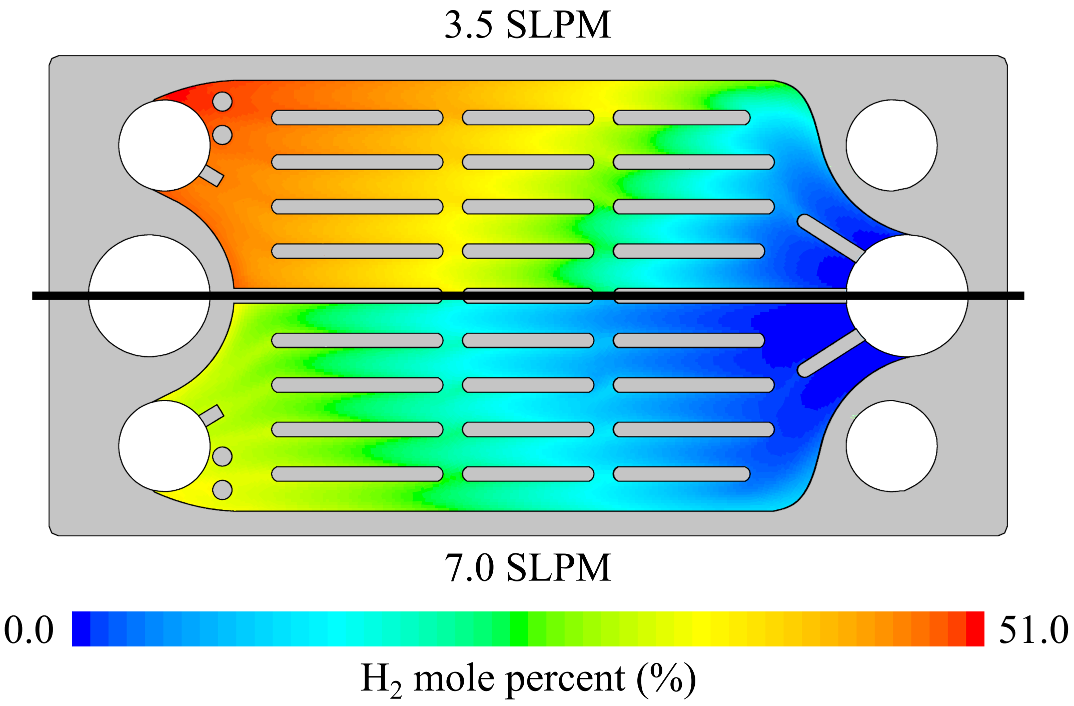

Figure 2.20: Contour plot of hydrogen mole percent within the microchannels. Solutions for 3.5 SLPM (top) and 7.0 SLPM (bottom) reactive side mass flow rate are shown. The direction of flow is from right to left.

Figure 2.20 shows in two dimensions what Figure 2.18 showed in one. Namely that the 3.5 SLPM case produces a roughly 68.0% increase in hydrogen yield at the outlet over the 7.0 SLPM case. It also indicates the outer channels tend to have higher hydrogen mole fractions. This seems to contradict the results in Figure 2.19. In fact, the higher hydrogen mole percent in the outer channels can be explained by gas velocity variation that exist between channels as well. A pathline analysis for the 7.0 SLPM, as an example, indicates that for a typical molecule traveling down the outermost channel, a representative residence time is about 22.0 ms. For the innermost channel, it is less than half that at roughly 10.0 ms. The 3.5 SLPM case shows a similar percentage change.

It stands to reason that an optimized internal geometry could more evenly distribute flow between channels, reducing the variability in catalyst utilization. Additionally, a large spread in residence time can be detrimental to reactor performance. These variations can reduce yield by promoting side reactions or increase potential for catalyst degradation in certain cases. This will be discussed further in Section 2.6.2

2.6.1 Thermal effects of SMR

SMR is a highly endothermic process (cf., Equations 1.2–1.3). Internal reforming is sure to have a marked effect on the thermal performance of the HEX-reactor. To investigate these effects, the reactor was simulated with the same boundary conditions as was done for the cases in Figure 2.18, namely the backing channel at 30 SLPM at 750 °C with the fuel inlet at 190 °C, S/C = 2.5, and two flow rates: 3.5 SLPM and 7.0 SLPM. As a point of comparison, the HEX-reactor was also run in non-reactive mode with no catalytic chemistry but all other conditions the same.

Figure 2.21 is a contour plot of the internal microchannel surfaces and internal alumina body temperature for the 7.0 SLPM case only. The bottom half is the solution to the non-reactive case while the top is the same simulation with chemistry considered. First note that at these conditions, the backing channel tends to dominate the thermal profile within the HEX-reactor. Comparing the two solutions, it's obvious the endotherm associated with catalytic chemistry tends to cool the internal surfaces, but the effect is not dominant. Each contour represents roughly 40 °C so for a given location within the reactor, the predicted temperature dropped by approximately 20 °C.

The largest temperature gradient is at the reactive flow inlet. This is exacerbated by the addition of chemistry as evidenced by the localized "cold" spot immediately inside the mi-

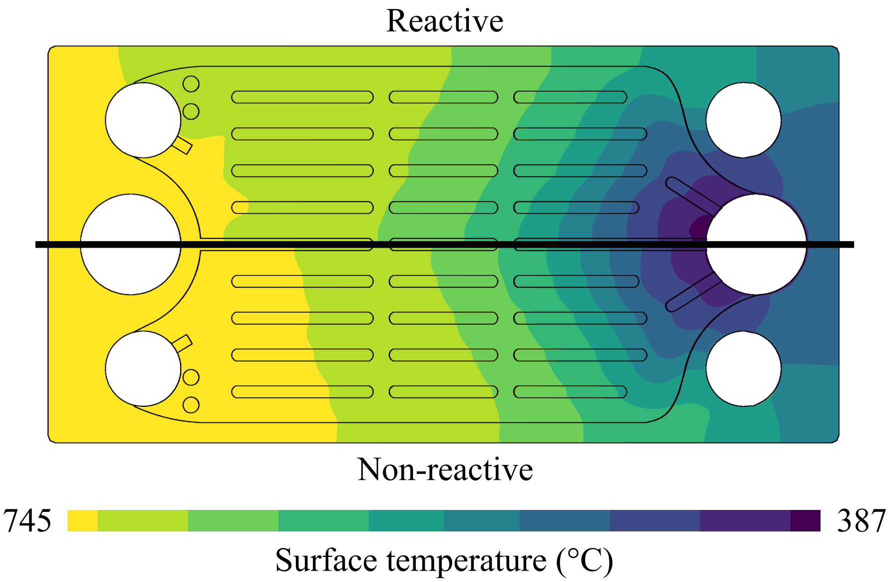

Figure 2.21: Contour plot of reactive surface and alumina body temperature for both reactive (top) and non-reactive (bottom) conditions. The backing side has a mass flow rate of 30 SLPM at 750 °C and the cold side is 7.0 SLPM at 190 °C. Both the reactive and non-reactive cases are run at a S/C = 2.5. The direction of flow is from right to left.

crochannel. From a mechanical perspective, this can have longevity consequences as ceramic materials tend to be more brittle as compared with metals used in similar applications.

Exploring further the catalytic and mechanical effects of SMR, Figure 2.22 illustrates temperature profiles for both the 3.5 SLPM and the 7.0 SLPM case. As above, both a reactive and non-reactive simulation was run for each condition. Figure 2.22a shows the temperature profile of the catalytically active surface along the flow direction of the HEX-reactor. Figure 2.22b plots the internal solid alumina body temperature. As in the species profiles in Figure 2.18, the temperatures are reported as a spatially averaged value. The solution varies in three dimensions but for clarity, temperature variations along the width and height of the reactor are averaged for a given axial position.

The first thing to note is that the predicted temperature drop with the inclusion of chemistry, both within the alumina body as a whole and on the catalytic surfaces, is pretty consistently 20 °C across the whole length of the HEX-reactor. This is true for both flow

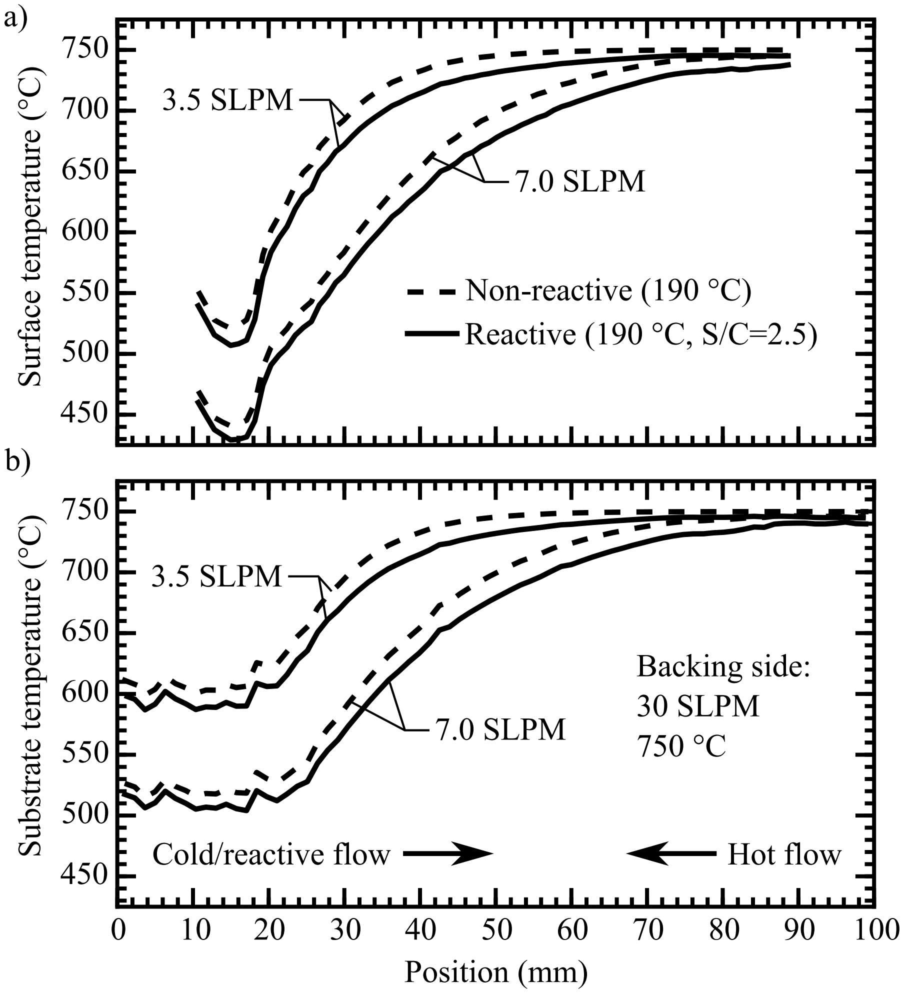

Figure 2.22: Average reactive surface a) and internal substrate temperature b) as a function of axial position within the reactor. Four different conditions are plotted: Non-reactive and catalytically reactive for both 3.5 and 7.0 SLPM.

cases as well. It is also clear that the change in mass flow rate of the inlet fuel mixture has a significantly larger effect on the overall thermal profile. Doubling the flow (from 11.6% of backing channel flow to 23.3%) dropped the average body temperature by roughly 100 °C at the fuel inlet side. The reactive surface temperature dropped by roughly the same amount. In all cases, by the time the reformate (or fuel mixture) exited the HEX-reactor, it had thermally equilibrated with the backing flow at roughly 750 °C. The scale of the cooling effect on internal flow paths is consistent the with findings of Murphy [52] when studied on a geometrically simplified channel flow model.

In the range of 0 – 20 mm on Figure 2.22 the solution appears noisy. In fact, the full 3D temperature solution is quite smooth, but due to the large thermal gradients at the fuel mixture inlet and the mix of geometric features in that region, the spatially averaged solution has the variability seen.

Performing a global energetic analysis can reveal more clearly the thermal costs of SMR. For the 3.5 SLPM case, performing an energy balance on the backing side flow shows approximately 60.5 W was transferred to the reactive flow. Based on predicted molar reaction rates r_i and referencing all species to the outlet temperature T_{out}, the heat of reaction Q_{rxn} can be calculated as

$$Q_{\mathrm{rxn}} = \sum_{\text{products}} r_i h_{i,\mathrm{T_{out}}} - \sum_{\text{reactants}} r_j h_{j,\mathrm{T_{out}}} \tag{2.10}$$

where $h_{i,\mathrm{T_{out}}}$ is the enthalpy of species i evaluated at the outlet temperature. The heat of reaction was calculated to be 10.7 W or roughly 15.4% of the total energy transferred to the reacting flow from the backing channel. Performing the same calculation for the 7.0 SLPM case leads to a heat of reaction of 12.6 W or roughly 10.0% of the heat energy supplied by the backing channel.

2.6.2 Carbon deposition

A critical consideration in catalytic chemistry is catalyst deactivation via carbon deposition or coking. This issue can appear as a gradual loss of activity over the life of the catalyst or rapid fouling due to improper conditions. Process conditions such as temperature, residence time, and gas-phase compositions can all affect coke formation.

Fouling carbon formations occur through a variety of pathways. At temperatures above 650 °C gas phase cracking and pyrolysis reactions can occur leading to deleterious coke depositions [68, 69]. At lower temperatures, coke formation tends to proceed via slower surface reactions. Adsorbed atomic carbon or CO or other hydrocarbon intermediates can evolve to high molecular weight coke formations or alternatively produce graphene-like or graphitic carbon filaments [70, 71]. Figure 2.23 illustrates various pathways for the evolution of surface species including that of carbon/coke formation on metal catalysts surfaces. While Figure 2.23 is presented in the context of a nickel catalyst, as nickel is commonly used in industry as a catalyst for SMR [72, 73], the same overall carbon deposition pathways exist for rhodium. Rhodium based catalysts tend to have high hydrogen selectivity and higher resistance to coking. Using nickel requires operating at high S/C to mitigate carbon deposition [74].

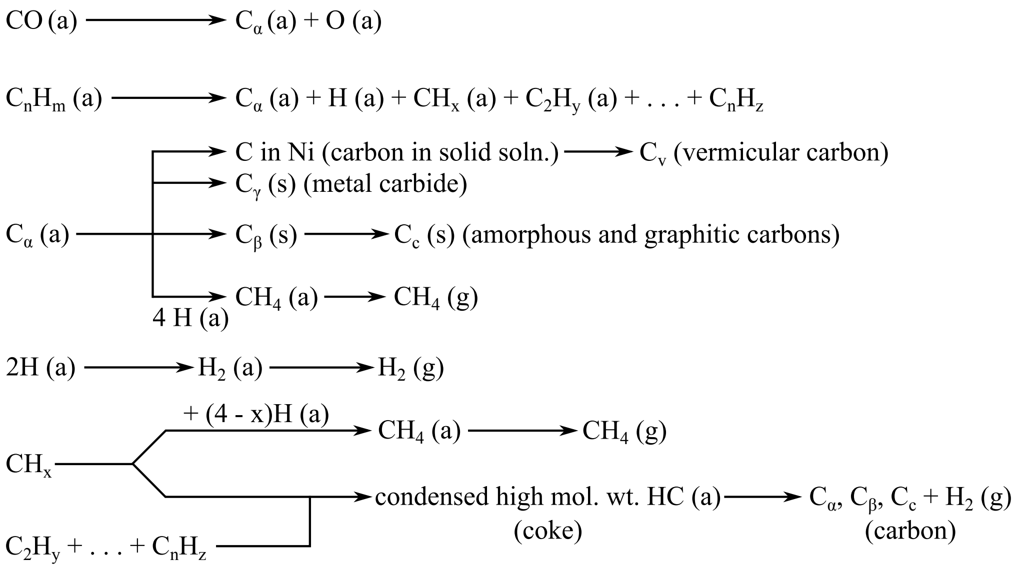

Figure 2.23: Transformation and evolution of carbon/coke formation on catalyst surfaces. a, g, and s refer to adsorbed, gaseous, and solid state, respectively. (Adapted from [70, 71])

Figure 2.23 illustrates the important role adsorbed CO and atomic carbon play in potential coking pathways. Here, α, β, v, γ, and c subscripts identify adsorbed, polymeric or amorphous, vermicular, metal carbide, and graphitic forms, respectively.

While the current model does not consider gas phase reactions that can occur above 650 °C, it can predict surface coverages of intermediate species and atomic carbon. The presence of these alone does not ensure coking, but simply act as indicator of potential fouling. The detailed thermodynamic and kinetic nature of coke formation is still an active area of research and is beyond the scope of this work.

Figure 2.24 is a contour plot of adsorbed atomic carbon on the reactive surfaces. As before, the top case is for the low flow 3.5 SLPM case while the bottom solution is for 7.0 SLPM. What is clear is that surface carbon seems to be dependent on residence time.

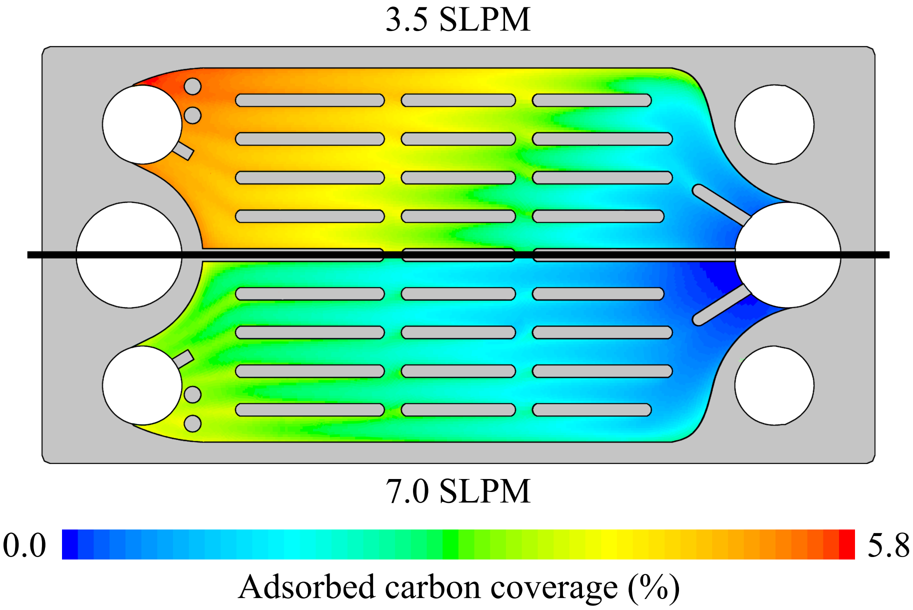

Figure 2.24: Contour plot of adsorbed atomic carbon surface site fraction. A solution for 3.5 SLPM (top) and 7.0 SLPM (bottom) is shown. The direction of flow is from right to left.

The low flow case only shows significant surface carbon (maximum of 5.8%) near the exhaust port of the microchannel layer. The higher flow case predicts 40 – 50% less surface carbon at its peak. Figure 2.24 suggests that given sufficient time-on-stream, fouling originating from adsorbed carbon is likely near the exhaust end of the microchannels.

Figure 2.25 similarly shows adsorbed CO on the reactive surfaces. The model predicts that surface CO site fractions remains approximately equal across the entire reactive surface for both flow conditions at roughly 10.0%. Several exceptions exist though. For the low flow case, CO site fraction is fairly consistent with the exception of near the entrance to the microchannels where it is slightly elevated. While small, there is a small effect in the draft of the first rib as the flow enters the reactor. This geometric effect is much more clear in the high flow case where shoulder near the entrance to the microchannels shows markedly higher adsorbed CO. This likely arises as a consequence of the reduced reactive surface temperature due to the higher flow, and the increased residence time in the shoulder. The kinetics mechanism used predicts an increase in equilibrium surface CO with decreasing temperature until approximately 457 °C where decreasing temperature shows decreasing surface CO.

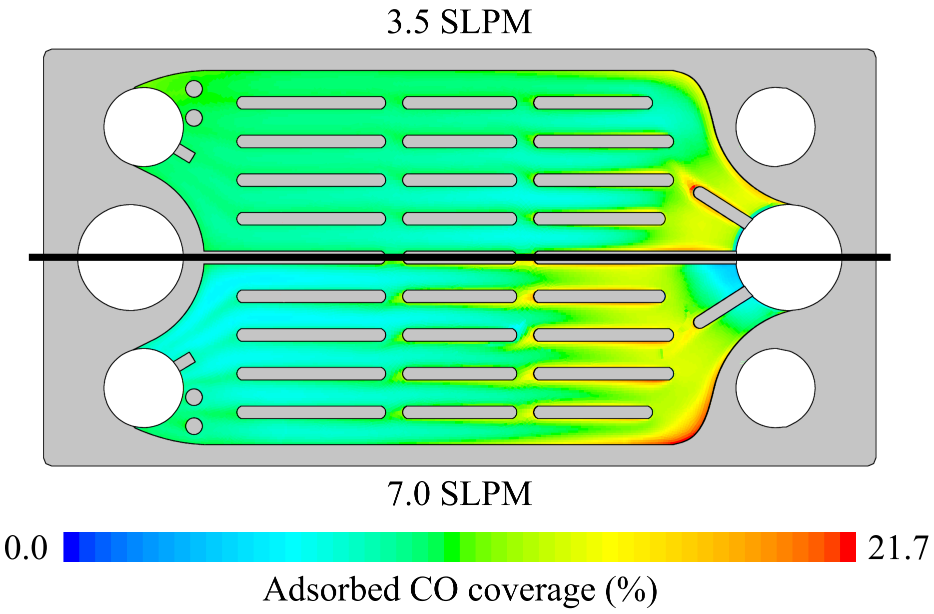

Figure 2.25: Contour plot of adsorbed CO surface site fraction. A solution for 3.5 SLPM (top) and 7.0 SLPM (bottom) is shown. The direction of flow is from right to left.

While adsorbed atomic carbon and CO are an incomplete study on catalyst fouling, they do provide insight into potential coking conditions. Additionally, by resolving the HEX-reactor in full 3D, the geometric effects as seen in Figure 2.25 become apparent where simplified models would not capture them.

2.7 Conclusions

Ceramic microchannel heat exchangers/reactors have several distinct advantages. They are cost effective, chemically inert, are capable of operating at high temperatures, and integrate well with internal catalyst. A 3D computational fluid dynamics model with conjugate heat transfer and detailed kinetics for methane steam reforming was developed to evaluate a particular design for a ceramic microchannel reactor. The model has been validated with pressure and thermal data collected from experiment. The role of thermal conductivity of the body material was investigated. It was found that for high flow cases, the thermal conductivity of the body material played a small roll on the overall HEX-reactor effectiveness. The only exception being for λ values less than 10 W m^{-1} K^{-1} where transverse thermal conduction was sufficiently inhibited. At low flow cases, the body material thermal conductivity plays a significant role on overall effectiveness. For the 25 SLPM case, an optimal thermal conductivity of $\lambda = 5$ W m^{-1} K^{-1} was identified. A roughly ten percentage point drop in effectiveness was predicted from the optimal thermal conductivity to the maximum tested, 150 W m^{-1} K^{-1}.

The effects of experimental manifolding were explored using a 3D manifolded model and a non-manifolded model as a benchmark against experimental data. The models predicted a roughly 5 – 50 W thermal loss to the environment over the range 2 – 50 SLPM cold-side flow.

Inert, high temperature simulations were used to quantify the hydraulic losses with the HEX-reactor. Predictions for internal flow at 50 SLPM suggest that only 10 – 20% of the overall pressure drop occurs within the actual microchannels. The remainder is caused by the microchannel inlet geometry and the support structures at the outlets. This is something to be considered for future design iterations.

Internal catalytic surface temperatures were profiled for a wide range of operating conditions. This illustrates the benefit of the tight thermal coupling inherent to microchannel heat exchangers. The internal reaction conditions could be controlled to within a relatively small window, though further study in comparing co- and counterflow configurations would be interesting.

Detailed kinetics for methane steam reforming over rhodium were integrated into the HEX-reactor model. The reactor model predicted 73.8% methane conversion at a reacting flow rate of 3.5 SLPM and a backing temperature of 750 °C. This prediction is in line with experimental measurements [52, 65, 69]. The coupled kinetics model was then used to predict the thermal behavior of the microchannel reactor in response to internal SMR. Finally a study of surface species coverages was conducted revealing catalyst degradation and coking potential under certain operating conditions.

Overall, this work has provided valuable new insight, predictive capability, and design consideration, into the development of a novel, ceramic microchannel reactor. As a tool for further investigation, the models developed here can facilitate future research on integrated HEX-reactor technology.

CHAPTER 3

ACCELERATED KINETICS MODELING

This chapter focuses on the adaptation of the in situ adaptive tabulation (ISAT) method for accelerating the simulation of detailed kinetics. Specifically ISAT is adapted to accelerate heterogeneous chemistry for transient simulations coupled with the CFD package ANSYS® FLUENT 15.0[1] where the fluid dynamics and energy equation are solved. FLUENT already has ISAT capabilities for homogeneous chemistry, but not for surface chemistry. The open-source chemical and thermodynamics package CANTERA [76] is used to solve the kinetics problem with ISAT handling tabulation and retrieval. ISAT is integrated with FLUENT via user defined functions (UDFs). To illustrate the approach, the transient behavior of SMR in the microchannel reactor discussed in Chapter 2 is considered.

While accelerating the simulation of heterogeneous chemistry is generally valuable, one application where high-fidelity and computationally efficient models play important roles is in the development of model predictive control strategies [77, 78]. In these methods, the inputs (i.e., actuation) to a detailed model, for example a fuel cell or catalytic reactor, are perturbed by small amounts and the transient response (i.e., sensors) measured. Using the relationships between the input perturbations and output response, locally linear models can be fit to the data. These reduced-order models capture the transient behavior of the system in the neighborhood of a particular operating point, but their small size (perhaps only a few tens of states)can be run in real-time and thus lend themselves well to control strategies that incorporate model prediction. The process of reducing large complex models to small locally linear models is known as system identification [79], and requires computationally expensive, transient simulations that can be impractical without some means of chemistry acceleration.

Significant portions of this chapter appear in the published work Blasi et al., 2016 [75]

[1] http://www.ansys.com/

3.1 Mathematical considerations

Modeling catalytic reactors requires the solution of multicomponent fluid mechanics, coupled with energy conservation for the gas and solid phases. The ISAT approach is primarily concerned with accelerating the catalytic chemistry, and thus directly affects the species conservation equations. Gas-phase species conservation within chemically reacting flow is expressed as

$$\frac{\partial}{\partial t}(\rho Y_k) + \nabla \cdot (\rho \mathbf{v} Y_k) = -\nabla \cdot \mathbf{j}_k + \tilde{\dot{s}}_k \tag{3.1}$$

where ρ and Y_k are the local density and the mass fraction of species k, respectively. The velocity vector is $\mathbf{v}$ and the diffusive mass flux for species k is $\mathbf{j}_k$.

Strictly speaking, the gas-phase species production by heterogeneous reactions $\dot{s}_k$ (kg m^{-2} s^{-1}) should appear as a boundary condition, not as a source term in Equation 3.1. However, in the CFD setting it can be convenient to assign the heterogeneous chemistry to a volume source within finite-volume cells that have catalytic surface. Thus

$$\tilde{\dot{s}}_k = \frac{A_\mathrm{s}}{V}\dot{s}_k, \tag{3.2}$$

where A_s is the catalytically active surface area and V is the finite-volume cell volume. The source term $\tilde{\dot{s}}_k$ is everywhere zero except in gas-phase cells that have a catalytically active face.

The species mass-production rates are evaluated as the sum of the rates of progress q_i over all the reactions involving the kth species [80]

$$\dot{s}_k = W_k \sum_{i=1}^{I} (\nu''_{ki} - \nu'_{ki}) q_i \qquad (k = 1, \ldots, K_s), \tag{3.3}$$

where W_k are the species molecular weights and ν''_{ki} and ν'_{ki} are the reverse and forward reaction stoichiometric coefficients, respectively. The rate of progress for the ith reversible reaction may be evaluated as

$$q_i = k_{f,i} \prod_{k=1}^{K} [X_k]^{\nu'_{ki}} - k_{r,i} \prod_{k=1}^{K} [X_k]^{\nu''_{ki}}, \tag{3.4}$$

where $k_{f,i}$ and $k_{r,i}$ are the forward and reverse rate constants, respectively. The rate constants are evaluated in Arrhenius form. In adsorption reactions, the forward rate constant can be evaluated in terms of a sticking coefficient γ_i as

$$k_{f,i} = \frac{\gamma_i}{\Gamma}\sqrt{\frac{RT}{2\pi W_k}}, \tag{3.5}$$

where Γ is the net surface site density and R is the gas constant. The activity $[X_k]$ of species k depends on its phase. For gas phase species activities are evaluated as the molar concentrations,

$$[X_k] = \rho\frac{Y_k}{W_k}. \tag{3.6}$$

The surface species activities are evaluated as

$$[X_k] = \theta_k\Gamma, \tag{3.7}$$

where θ_k are the surface site fractions. The transient evolution of surface species is represented as

$$\frac{d\theta_k}{dt} = \frac{\dot{s}_k}{\Gamma} \qquad (k = 1, \ldots, K_\mathrm{s}). \tag{3.8}$$

Energy conservation is represented generally as

$$\frac{\partial}{\partial t}(\rho h) + \nabla\cdot(\mathbf{v}\rho h) = \nabla\cdot\left(\lambda\nabla T - \sum_{k=1}^{K_g} h_k\mathbf{j}_k\right) \tag{3.9}$$

where λ is the thermal conductivity, h_k is the enthalpy of species k, and the mixture enthalpy h in the gas phase is defined as

$$h = \sum_{k=1}^{K_g} Y_k h_k\ . \tag{3.10}$$

Within the solid phase (i.e., reactor body), the convective and species-diffusion terms vanish. Because the energy equation is written in terms of enthalpy, the thermal effects of the catalytic reaction do not explicitly appear up in Equation 3.9. Instead, the variation in species composition of the catalytic control volume due to the source term in Equation 3.1 directly modifies the mixture enthalpy via Equation 3.10. FLUENT then solves the larger heat transfer problem between the gas phase and the solid boundary normally.

3.1.1 Local state vectors

The gas-phase composition varies spatially and temporally according to the coupled effects of convection, diffusion, and reaction (Equation 3.1). However, the surface-species coverages θ_k depend only on the local thermochemical state at each reactive face, which may be represented by the vector

$$\mathbf{x} = \{\theta_1, \theta_2, ..., \theta_{\mathrm{K_s}}, Y_1, Y_2, ..., Y_{\mathrm{K_g}}, T_{\mathrm{s}}, \Delta t\}, \tag{3.11}$$

where T_{s} is the surface temperature and Δt is the CFD time step over which the chemistry is solved. The CFD time step can be large compared to the numerous time steps needed to solve the stiff kinetics problem (i.e., Equation 3.8) accurately. The solution vector for the local kinetics problem is returned as

$$\mathbf{f}(\mathbf{x}) = \{\theta_1^{\mathrm{t+\Delta t}}, \theta_2^{\mathrm{t+\Delta t}}, ..., \theta_{\mathrm{K_s}}^{\mathrm{t+\Delta t}}, \dot{s}_1, \dot{s}_2, ..., \dot{s}_{\mathrm{K_g}}\}, \tag{3.12}$$

where $\theta_{\mathrm{k}}^{\mathrm{t+\Delta t}}$ are the new surface coverages after the CFD time step Δt and $\dot{s}_k$ are the area-normalized production rates for gas-phase species (kg s^{-1} m^{-2}).

3.2 ISAT algorithm

For each chemically reactive surface or volume, a system of ordinary differential equations (ODEs) must be solved for each CFD time step (i.e., Equation 3.8). For large models with thousands to millions of reactive cells and tens to hundreds of species, the cost of solving K_{s} ODEs for each cell is usually substantial. In fact, the chemistry simulation can dominate the overall computational cost. ISAT seeks to take advantage of redundancy in these calculations to reduce overall computational costs.

During the course of a CFD simulation it will often be the case that either spatially or temporally separated mesh points will share the same, or nearly the same, initial thermochemical state $\mathbf{x}$. Because the solution to the ODEs governing chemical kinetics is deterministic, the result of the $\mathbf{f}(\mathbf{x})$ depends only on the initial condition $\mathbf{x}$. Simply storing these results and retrieving them later can reduce computation time significantly. The ISAT algorithm efficiently handles the tabulation and retrieval of these solutions. Essentially, ISAT tabulates the vector function $\mathbf{f}(\mathbf{x})$. In response to an input query, $\mathbf{x}^{\mathrm{q}}$, ISAT returns either the exact solution $\mathbf{f}(\mathbf{x}^{\mathrm{q}})$, or an approximation $\mathbf{f}^{\mathrm{a}}(\mathbf{x}^{\mathrm{q}})$. It is impractical and unnecessary to tabulate all possible query vectors that might be encountered during a simulation. ISAT instead stores known solutions throughout the thermochemical space and then linearly interpolates to queries that fall nearby as

$$\mathbf{f}^{\mathrm{a}}(\mathbf{x}^{\mathrm{q}}) = \mathbf{f}^{n}(\mathbf{x}^{n}) + \mathbf{A}^{n}(\mathbf{x}^{\mathrm{q}} - \mathbf{x}^{n}), \tag{3.13}$$

where $\mathbf{f}^{n}(\mathbf{x}^{n})$ is a tabulated solution to $\mathbf{x}^{n}$ that is sufficiently close to $\mathbf{x}^{\mathrm{q}}$ for the linear approximation to be accurate. $\mathbf{A}^{n}$ is the associated mapping-gradient matrix ($n_{\mathrm{f}} \times n_{\mathrm{x}}$) to the solution $\mathbf{f}^{n}(\mathbf{x}^{n})$,

$$A_{i,j} = \frac{\partial f_i}{\partial x_j} \tag{3.14}$$

The error ε in the interpolated solution, $\mathbf{f}^{\mathrm{a}}(\mathbf{x}^{\mathrm{q}})$, is measured using the two-norm as

$$\varepsilon(\mathbf{x}^{\mathrm{q}}) = ||\mathbf{f}^{\mathrm{a}}(\mathbf{x}^{\mathrm{q}}) - \mathbf{f}(\mathbf{x}^{\mathrm{q}})|| \tag{3.15}$$

The region in n_{x}-dimensional space for which $\varepsilon(\mathbf{x}^{\mathrm{q}})$ falls within a specified error tolerance, $\varepsilon_{\mathrm{tol}}$, is known as the region of accuracy (ROA). The error tolerance is evaluated in terms of absolute and relative tolerances as

$$\varepsilon_{\mathrm{tol}} = \varepsilon_{\mathrm{a}} + \varepsilon_{\mathrm{r}}||\mathbf{f}||. \tag{3.16}$$

Within the ROA, no additional tabulation is necessary as long as the interpolating error is within the specified tolerance. The ROA itself is expensive to evaluate exactly so instead it is approximated by an ellipsoid of accuracy (EOA). The EOA is initially constructed conservatively, meaning that it covers a smaller space than $\varepsilon_{\mathrm{tol}}$ would actually permit (see Figure 3.1). This ensures a high probability that interpolated values will be within $\varepsilon_{\mathrm{tol}}$. As more information is generated through the course of the simulation, the EOA for a particular table entry might be found to be too conservative. It can then be expanded to incorporate regions found to be within tolerance, but not included in the initial calculation of the EOA.

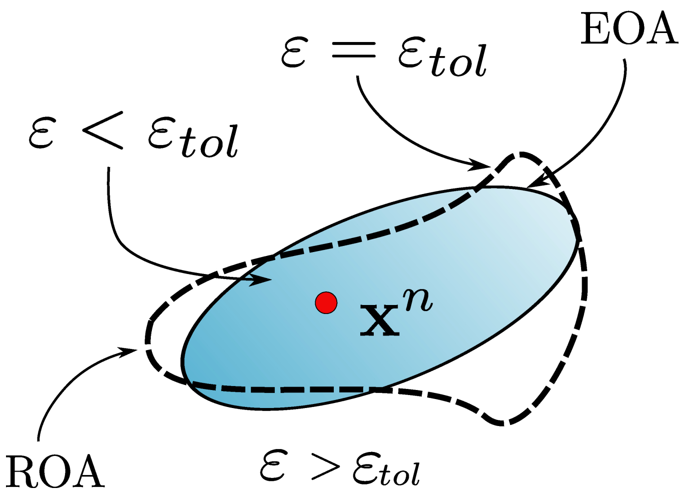

Figure 3.1: A tabulated entry, $\mathbf{x}^n$, and its associated region of accuracy (ROA) and approximated ellipsoid of accuracy (EOA)

Given a state query $\mathbf{x}^{\mathrm{q}}$, ISAT may take one of three possible actions:

Retrieve The existing entries will be searched for those whose EOA covers $\mathbf{x}^{\mathrm{q}}$. If one exists, $\mathbf{f}^{\mathrm{a}}(\mathbf{x}^{\mathrm{q}})$ will be calculated via Equation (3.13) and returned.

Grow If the retrieve fails, $\mathbf{f}(\mathbf{x}^{\mathrm{q}})$ is evaluated directly (i.e., the chemistry problem is solved). Tabulated values surrounding $\mathbf{x}^{\mathrm{q}}$ are tested to check if $\mathbf{f}(\mathbf{x}^{\mathrm{q}})$ is within $\varepsilon_{\mathrm{tol}}$. If so, the EOA of the corresponding entry is expanded to incorporate this new information and $\mathbf{f}(\mathbf{x}^{\mathrm{q}})$ is returned. No new entries are created.

Add If after directly evaluating $\mathbf{f}(\mathbf{x}^{\mathrm{q}})$, no candidates for EOA expansion are found, a new entry is added to the table for $\mathbf{f}(\mathbf{x}^{\mathrm{q}})$ with its corresponding $\mathbf{A}^n$ and EOA.

Initially the ISAT table is empty. As the CFD simulation progresses, the table is populated by entries as they are encountered and evaluated. The result is a table that is limited to the region of thermochemical space required by the simulation. As the solution evolves, the table expands to accommodate new thermochemical states.

Every entry in the table stores the input vector $\mathbf{x}^n$, its associated solution $\mathbf{f}^n$, the sensitivities of that solution, $\mathbf{A}^n$, and the calculated EOA. The table is structured as a binary tree with algorithms for traversing it efficiently. The selection of a smaller error tolerance results in a larger and more densely populated table, but less error in interpolated solutions. A larger error tolerance will result in fewer entries covering the same n_{x}-dimensional space, but with reduced accuracy.

Keeping the table as small as possible is important for minimizing costs associated with navigation and search. Techniques such as "pruning" and table-restart seek to keep ISAT overhead low. Pruning is the systematic removal of table entries that are very infrequently visited. The assumption being that the solution space no longer includes that entry and it can be discarded. Table-restart is the wholesale deletion and rebuilding of the table during simulation. Table-restart is only advantageous when the solution has changed significantly and occupies an entirely different space.

3.2.1 Implementation

In its native mode Fluent calls its internal surface-kinetics solver to evaluate heterogeneous reaction rates and predict fluxes of gas-phase species to and from the catalytic surfaces. In other words, as noted in discussing Equation 3.1, the objective is to evaluate $\dot{s}_k$ in each finite-volume cell that has a catalytically active face.

To integrate ISAT with Fluent, the internal kinetics solver is replaced via the use of UDFs. UDFs enable access to Fluent's internal flow variables (e.g., gas-phase species mass fractions, surface temperature), which are then made accessible to ISAT and Cantera software. The resulting species-production rates that are evaluated by ISAT/Cantera are returned to the Fluent core code and used as they would be in the native Fluent implementation. In addition to the species-conservation equations, Fluent also updates the energy equation. Disabling Fluent's kinetics solver through the UDF interface means there is no internal accounting for surface species θ_k. Instead, surface species coverages as evaluated by ISAT/Cantera are stored on a face-by-face basis in Fluent's User Defined

Memory (UDM).

3.3 Model

To illustrate the ISAT approach, methane steam reforming over a rhodium catalyst is simulated in the ceramic microchannel reactor developed in Chapter 2. For review, Figure 3.2 shows an exploded view of the reactor body, together with illustrative solutions. The microchannel reactor is composed of alternating flow layers within a fully enclosed alumina body. The internal microchannel features are on the order of hundreds of microns to millimeters and the overall dimensions are approximately 100 mm × 50 mm × 7.5 mm for a four-layer configuration. Two of the layers have channels that are wash coated with the catalyst. The alternating channels carry chemically inert gas flows that help maintain temperature control within the catalytically active layers. A relatively cool reactant mixture of methane and steam enters a series of channels coated with a rhodium catalyst on an Al_2O_3/CeO_2 support. The reactive microchannels are thermally coupled to the counter-flow channels that carry hot inert gases. The backing fluid is used to tightly control the thermal

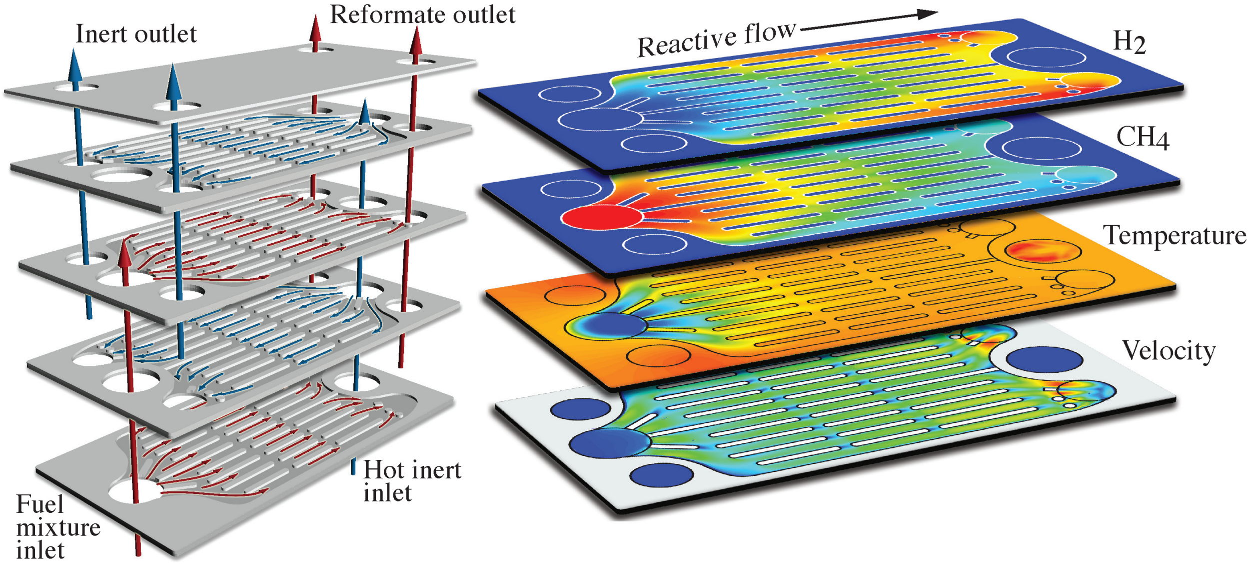

Figure 3.2: An exploded view of the microchannel reactor (left) and an example solution of chemically reacting flow within a reactive layer (right)

conditions on the reactive side. In this case, supporting the endothermic steam-reforming of methane.

3.3.1 Fluid dynamics model

The thermal and fluid dynamics model is implemented using ANSYS FLUENT 15.0. Figure 3.3 illustrates a plan view of the channel and manifold geometry. The model has approximately 396,000 finite-volume cells, 20,237 of which have at least one catalytically active face (22,237 catalytically active faces in total).

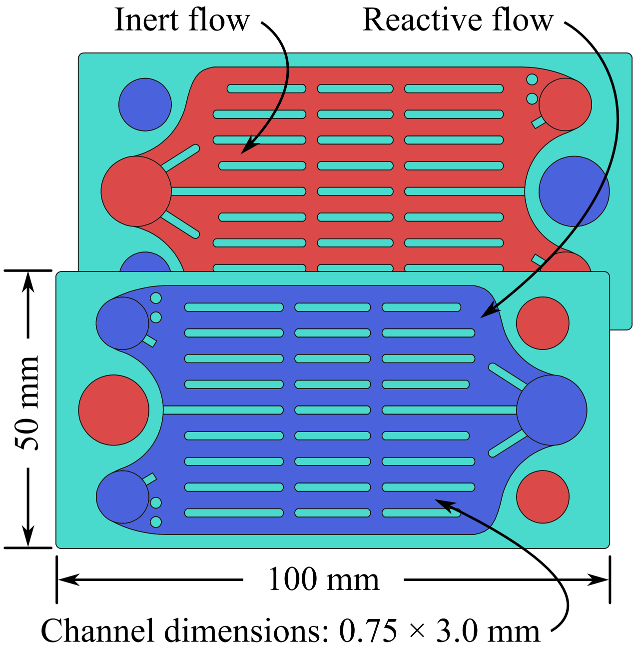

Figure 3.3: Plan view of the two reactor channel layers. Blue represents reactive flow and red represents inert, backing flow. The channel dimensions are 0.75 mm × 3 mm. The overall slide is 50 mm × 100 mm × 1.5 mm.

3.3.2 Kinetics modeling

The methane steam-reforming kinetics is modeled using a 48-step reaction mechanism (Table 3.1). [66, 67]. This mechanism, which includes 7 gas-phase species and 13 surface species, is written as irreversible pairs of reactions. Thus, for each reaction, only the first term of Equation 3.3 is used. Most of the forward rate expressions are represented in Arrhenius form. Eleven of the reactions have coverage-dependent activation energies [80]. The reactions identified as "stick" evaluate the forward rate constant as shown in Equation 3.5, with γ being entered in the A column.

The kinetics problems are solved using the open-source chemical kinetics software CANTERA to solve the 13 species-conservations equations from t to $t + \Delta t$ for each CFD time step. For the solution of each particular control volume, the mass fractions of the 7 gas-phase species are held constant at the values arising from Equation 3.1. Effectively, each catalytically active control volume is modeled as a large, well mixed reactor. CANTERA is also used to evaluate the mapping gradient matrix $\mathbf{A}$ required for error control and to interpolate to thermochemical states near $\mathbf{x}$. The $\mathbf{x}$ and $\mathbf{f}$ are the input and output vectors, respectively, which are tabulated and returned by the ISAT procedure. For the mechanism used (Table 3.1), $\mathbf{x}$ has a dimension of 22 and $\mathbf{f}$ has a dimension of 20. The CVODE software [81, 82] (part of the LLNL solver package SUNDIALS [83]) is used to solve the kinetics problem from t to $t + \Delta t$. CVODE is a stiff differential equation solver based on the backward differential formulas (BDF), which uses adaptive time-step control to maintain stability and accuracy.

3.4 Results and discussion

ISAT provides the largest efficiency improvements when solving steady-state problems and problems that occupy a small fraction of the possible thermochemical space. When the solution space is changing, solving the kinetics must be done more frequently. Thus, there is additional computational overhead associated with tabulation, thus compromising some of the ISAT speed-up. To test the relative costs of steady and transient solutions, the reactor was simulated under three conditions at nominally the same operating point. The first test simulates constant inputs, solving from an arbitrary initial state to a steady-state solution. The second example makes a 10% perturbation to the reactive inlet mass flow rate after the ISAT table has been populated. The step change effectively shifts the entire solution away from the already tabulated states, requiring the table to expand. The third case has the same perturbation as the second, but the inputs are returned to initial values after 10 s.

Table 3.1: Kinetic mechanism for the steam reforming of methane over rhodium. Rate coefficients are given in the Arrhenius form $k = AT^{\beta}\exp(-E_a/RT)$. The surface density is $\Gamma = 2.72 \times 10^{-9}$ mol cm^{-2}[66, 67].

Reaction	A (cm,mol,s)	β	E_a (kJ·mol^{-1})
$H_2 + Rh(s) + Rh(s) \rightarrow H(s) + H(s)$	0.030	stick	
$H(s) + H(s) \rightarrow Rh(s) + Rh(s) + H_2$	5.574×10^{19}	0.239	59.691
$O_2 + Rh(s) + Rh(s) \rightarrow O(s) + O(s)$	0.010	stick	
$O(s) + O(s) \rightarrow Rh(s) + Rh(s) + O_2$	5.329×10^{22}	-0.137	386.995
$CH_4 + Rh(s) \rightarrow CH_4(s)$	1.300×10^{-2}	stick	
$CH_4(s) \rightarrow CH_4 + Rh(s)$	1.523×10^{13}	-0.110	26.018
$H_2O + Rh(s) \rightarrow H_2O(s)$	1.000×10^{-1}	stick	
$H_2O(s) \rightarrow H_2O + Rh(s)$	6.858×10^{14}	-0.280	44.993
$CO_2 + Rh(s) \rightarrow CO_2(s)$	4.800×10^{-2}	stick	
$CO_2(s) \rightarrow CO_2 + Rh(s)$	3.920×10^{11}	0.315	20.505
$CO + Rh(s) \rightarrow CO(s)$	4.971×10^{-1}	stick	
$CO(s) \rightarrow CO + Rh(s)$	1.300×10^{13}	0.295	$134.07 - 47.00\theta_{CO}$
$H(s) + O(s) \rightarrow OH(s) + Rh(s)$	8.826×10^{21}	-0.048	73.365
$OH(s) + Rh(s) \rightarrow H(s) + O(s)$	1.000×10^{21}	0.045	48.041
$H(s) + OH(s) \rightarrow H_2O(s) + Rh(s)$	1.743×10^{22}	-0.127	41.731
$H_2O(s) + Rh(s) \rightarrow H(s) + OH(s)$	5.408×10^{22}	0.129	98.220
$OH(s) + OH(s) \rightarrow H_2O(s) + O(s)$	5.736×10^{20}	-0.081	121.594
$H_2O(s) + O(s) \rightarrow OH(s) + OH(s)$	1.570×10^{20}	0.081	203.407
$C(s) + O(s) \rightarrow CO(s) + Rh(s)$	1.173×10^{22}	0.0	$92.142 - 120.00\theta_{C}$
$CO(s) + Rh(s) \rightarrow C(s) + O(s)$	6.390×10^{21}	0.0	$174.00 - 47.00\theta_{CO}$
$CO(s) + O(s) \rightarrow CO_2(s) + Rh(s)$	6.183×10^{21}	0.034	$129.982 - 47.00\theta_{CO}$
$CO_2(s) + Rh(s) \rightarrow CO(s) + O(s)$	5.752×10^{22}	-0.175	106.492
$CO(s) + OH(s) \rightarrow COOH(s) + Rh(s)$	2.922×10^{20}	0.0	$55.334 - 47.00\theta_{CO}$
$COOH(s) + Rh(s) \rightarrow CO(s) + OH(s)$	2.738×10^{21}	0.0	48.375
$COOH(s) + Rh(s) \rightarrow CO_2(s) + H(s)$	1.165×10^{19}	0.160	5.610
$CO_2(s) + H(s) \rightarrow COOH(s) + Rh(s)$	1.160×10^{20}	-0.160	14.480
$COOH(s) + H(s) \rightarrow CO(s) + H_2O(s)$	5.999×10^{19}	-0.188	33.552
$CO(s) + H_2O(s) \rightarrow COOH(s) + H(s)$	2.258×10^{19}	0.051	$97.078 - 47.00\theta_{CO}$
$CO(s) + OH(s) \rightarrow CO_2(s) + H(s)$	3.070×10^{19}	0.00	$82.938 - 47.00\theta_{CO}$
$CO_2(s) + H(s) \rightarrow CO(s) + OH(s)$	2.504×10^{21}	-0.301	84.767
$C(s) + OH(s) \rightarrow CO(s) + H(s)$	4.221×10^{20}	0.078	$30.038 - 120.00\theta_{C}$
$CO(s) + H(s) \rightarrow C(s) + OH(s)$	3.224×10^{21}	-0.078	$138.262 - 47.00\theta_{CO}$
$CH_4(s) + Rh(s) \rightarrow CH_3(s) + H(s)$	4.622×10^{21}	0.136	72.262
$CH_3(s) + H(s) \rightarrow CH_4(s) + Rh(s)$	2.137×10^{21}	-0.058	46.770
$CH_3(s) + Rh(s) \rightarrow CH_2(s) + H(s)$	1.275×10^{24}	0.078	107.563
$CH_2(s) + H(s) \rightarrow CH_3(s) + Rh(s)$	1.073×10^{21}	-0.078	39.537
$CH_2(s) + Rh(s) \rightarrow CH(s) + H(s)$	1.275×10^{24}	0.078	115.388
$CH(s) + H(s) \rightarrow CH_2(s) + Rh(s)$	1.073×10^{22}	-0.078	52.612
$CH(s) + Rh(s) \rightarrow C(s) + H(s)$	1.458×10^{20}	0.078	23.088
$C(s) + H(s) \rightarrow CH(s) + Rh(s)$	1.122×10^{23}	-0.078	$170.712 - 120.00\theta_{C}$
$CH_4(s) + O(s) \rightarrow CH_3(s) + OH(s)$	3.465×10^{23}	0.051	77.708
$CH_3(s) + OH(s) \rightarrow CH_4(s) + O(s)$	1.815×10^{22}	-0.051	26.892
$CH_3(s) + O(s) \rightarrow CH_2(s) + OH(s)$	4.790×10^{24}	0.0	114.517
$CH_2(s) + OH(s) \rightarrow CH_3(s) + O(s)$	2.858×10^{21}	0.0	20.883
$CH_2(s) + O(s) \rightarrow CH(s) + OH(s)$	4.790×10^{24}	0.0	141.792
$CH(s) + OH(s) \rightarrow CH_2(s) + O(s)$	2.858×10^{21}	0.0	53.408
$CH(s) + O(s) \rightarrow C(s) + OH(s)$	5.008×10^{20}	0.0	26.792
$C(s) + OH(s) \rightarrow CH(s) + O(s)$	2.733×10^{22}	0.00	$148.808 - 120.00\theta_{C}$

This tests the relative performance of ISAT when expanding the table and then returning to the previously tabulated thermochemical space. As a point of comparison, all cases were run with the kinetics being handled by FLUENT's internal surface chemistry solver (i.e., without ISAT). All simulations were run on 12 Intel E5-2680 processors with 0.5 s CFD time steps. The ISAT absolute and relative error tolerances (Equation 3.16) were set to 5.0×10^{-5} and 1.0×10^{-4}, respectively. The components of the input and output vectors are scaled individually to be order-one, such that Equation 3.15 provides a reasonable overall measure of error.

3.4.1 Steady inputs

The reactor was simulated with a reactive-side inlet flow rate of 3.5 standard liters per minute (SLPM) of CH_4 and H_2O with a steam-to-carbon ratio of 2.5 and 190 °C. The backing channel was run at 30 SLPM of N_2 and 750 °C. Figure 3.4 shows the simulation time versus wall-clock-time performance for FLUENT alone and FLUENT integrated with ISAT-CANTERA over 30 s of simulated time. While not easily evident from Figure 3.4, the first time step of the FLUENT-ISAT case required a great deal of time to construct the initial ISAT table. Although the first CFD time step demands time to build the table from scratch, subsequent time steps require only infrequent table updates. This results in a speed-up factor of approximately 20 after the 30 s simulation time.

Figure 3.5 shows that solutions using FLUENT alone and FLUENT-ISAT are virtually indistinguishable. Additionally, Figure 3.6 shows the distribution of error in ISAT queries for 125,000 calls for this simulation. The maximum error was well under 1%. Relaxing error tolerances could provide further gains in computational time, but possibly with some loss of accuracy.

3.4.2 Perturbed inputs

To test the cost of table expansion, a problem similar to the steady problem was investigated. In this case, the problem was exactly the same as the previous case up to

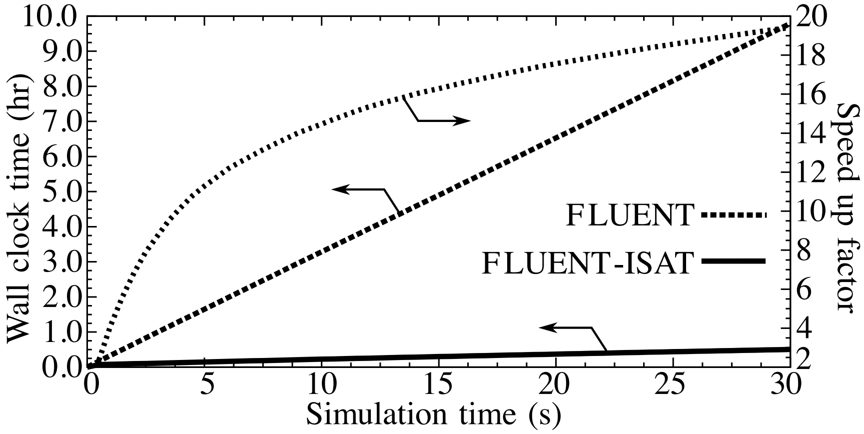

Figure 3.4: Simulation time versus wall-clock time for both FLUENT alone and the FLUENT-ISAT algorithm.Results are for 30 s of a transient simulation with steady inputs. This simulation resulted in 14,612 ISAT table entries.

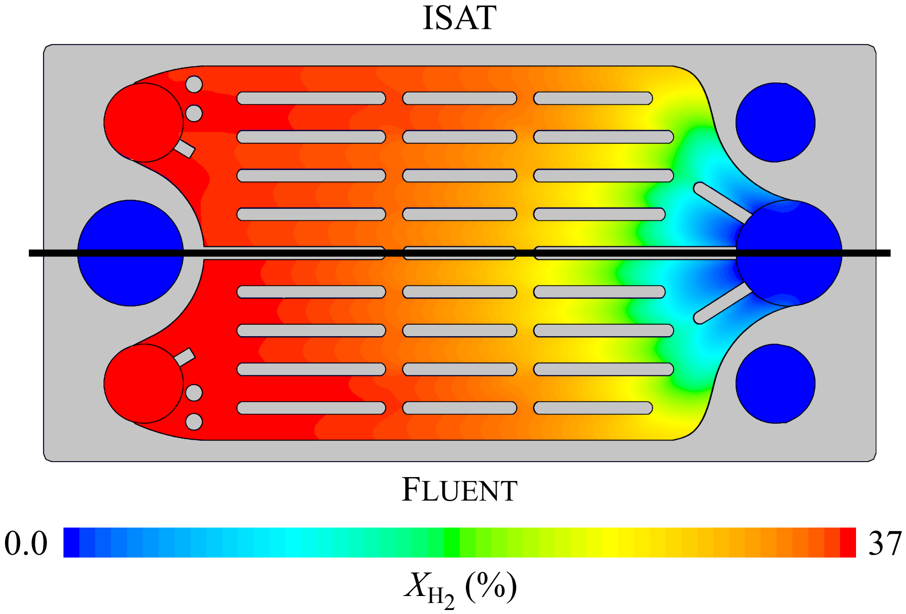

Figure 3.5: Predicted hydrogen mole fraction contours using FLUENT's internal kinetics solver using the ISAT algorithm.

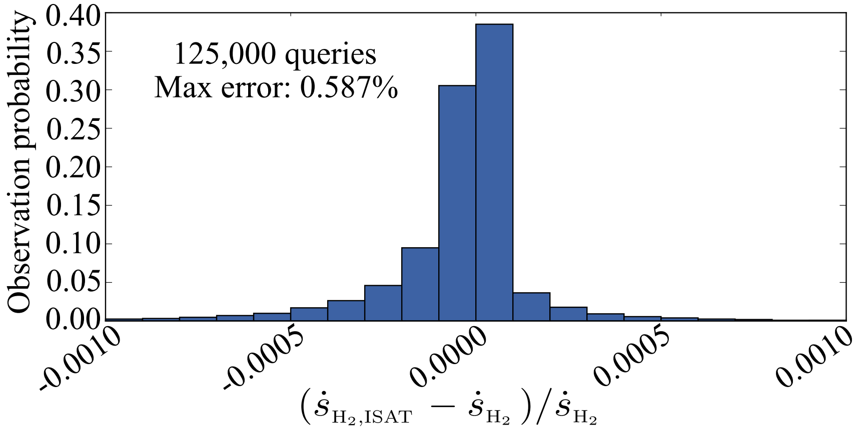

Figure 3.6: Distribution of error in hydrogen production at the catalytic surface for 125,000 ISAT queries.The maximum error for this set of queries was 0.587%.

10 s of simulation time. At that point, the reactive-side inlet flow rate was suddenly increased by 10%, with the steam-to-carbon ratio remaining unchanged. This perturbation significantly changed the operating conditions, rendering all or part of previously tabulated kinetics solutions to be essentially useless. Figure 3.7 illustrates the computational effect of the perturbation. As easily anticipated, the FLUENT-alone solution shows no effect from the step-change. Both prior to and after the inlet-flow-rate step, the same number of chemistry solutions are required. However, ISAT must, at least in part, rebuild its table to incorporate new thermochemical space. The bulk of this cost occurs in the time steps immediately following the step change, and then tapers off as the solution stabilizes around its new operating point. Over the 30 s simulation time, the resulting speed-up factor was reduced to approximately 15.5.

To enable model-predictive control, system identification requires making small perturbations to the inputs and observing the transient response of the outputs. As the ISAT table expands to accommodate new thermochemical space, the computational cost of each subsequent perturbation should decrease. To test this behavior, the reactive side inlet flow rate was again increased via a 10% step change at 10 s but then returned to its original value at 20 s. Presumably, the cost of traversing the new solution space after the step increase should

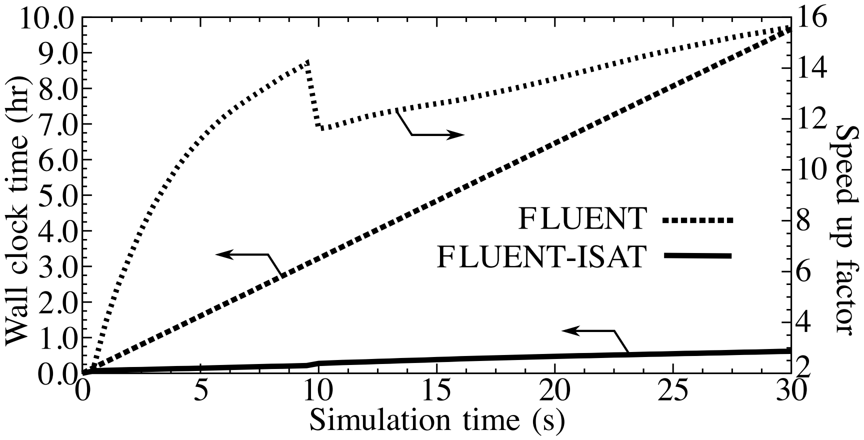

Figure 3.7: Simulation time versus wall-clock time for both Fluent alone and the Fluent-ISAT algorithm.Results are for 30 s of a transient simulation with a 10% step increase in reactive side flow rate at 10 s. This simulation resulted in 31,075 ISAT table entries.

be greater than traversing that same space back to the starting inputs. Figure 3.8 illustrates the results of this test. The second perturbation had a smaller effect on the speed-up factor as compared to the first. This can be further demonstrated by the number of ISAT table entries required to sufficiently cover the solution space. In the first case with steady inputs, 14,612 entries were required to tabulate the observed thermochemical states. This number more than doubled in the second case to 31,075 entries. Returning to the nominal reactive side flow rate required an increase of approximately 16% to 36,091 entries, a significantly smaller change. The overall speed-up factor dropped from roughly 15.5 to 14.5. These results indicate that ISAT is well suited to accelerate system-identification simulations, where inputs are perturbed by small amounts around a nominal operating condition.

3.5 Conclusions

Prior ISAT research for modeling combustion kinetics has reported speed-up by factors from 100 to 1000. Certainly, such speed-up factors are significantly greater than the factors of 10 – 20 reported here for catalytic chemistry. However, there are fundamental differences between speed-up potentials between homogeneous and heterogeneous kinetics. The most significant difference is that surface chemistry is inherently a lower dimensional problem

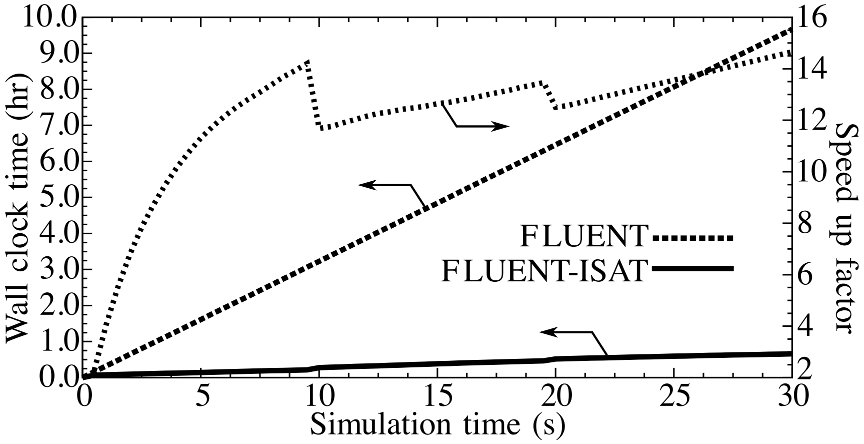

Figure 3.8: Simulation time versus wall-clock time for both FLUENT alone and the FLUENT-ISAT algorithm.Results are for 30 s of a transient simulation with a 10% step increase in reactive side flow rate at 10 s and a return to initial inputs at 20 s. This simulation resulted in 36,091 ISAT table entries.

compared to homogeneous chemistry.

In combustion (or any simulation with homogeneous chemistry) every CFD volume can be chemically active, meaning the cost of solving the chemistry represents a larger fraction of the overall computational cost and therefore larger gains can be achieved by ISAT. Surface chemistry, while still expensive, proceeds only in CFD cells that have catalytically active faces (in the present models, approximately 5.5% of all CFD cells have catalytically active faces). In the test cases reported here, once the ISAT tables are built and additional kinetics solutions are infrequent, the heterogeneous chemistry becomes virtually free. In the FLUENT-alone case, solving the chemistry for only 5.5% of the CFD cells constitutes approximately 95% of the total computation time. For models with a higher fraction of reactive surfaces or more species, that percentage will be higher, and larger speed-up factors can be achieved.

Speed-up factors of 10 – 20 represent very significant computational savings. For example, some 10 to 20 different design alternatives could be evaluated using computational resources that would previously be needed to evaluate a single design. The ISAT approach greatly reduces the computational resources needed to develop reduced-order models needed in model-predictive control. In fact, ISAT is particularly well suited to the small-perturbation inputs that characterize system identification.

CHAPTER 4

WASHCOAT MICROSTRUCTURE ANALYSIS

The overarching goal of this work is to develop simple relations that can be used to assist the qualitative and quantitative interpretation of washcoat performance. This is accomplished by developing geometrically simple models motivated by the well known one-dimensional Thiele analysis [35, 36], that are validated and informed by geometrically complex simulations of actual washcoat structures. The washcoat structures are reconstructed from FIB-SEM experiments performed on actual commercial Rh-γAl_2O_3 partial-oxidation catalyst washcoat.

The geometrically simple cylindrical-pore model and the geometrically complex three-dimensional reconstructed-pore model both characterize the reaction-diffusion processes in terms of a Damköhler number that relates an irreversible first-order reaction and an effective diffusion coefficient. Both models report performance metrics in terms of dimensionless effective product flux emerging from the pore opening, the pore effectiveness, and the depth of reaction. By casting the models in compatible forms, insight from the complex microscale geometry can be used in the more traditional setting. The overall performance metrics for the reconstructed pores are mapped to the same performance metrics that emerge from the ideal cylindrical-pore model. This process provides quantitative insight that assists understanding the relationships between approximate macroscale models and actual washcoat microstructures. The objective is to seek generalizations that enable the actual complex catalyst microstructures to be represented in terms of easier-to-use dimensionless representations. The results from this study can be further used to assist designing and improving washcoat morphologies (e.g., thickness, porosity, surface/volume ratio) for targeted catalytic

---

Significant portions of this chapter appear in the submitted work Karakaya et al., 2015 [84] and Blasi et al., 2015 [85]. The work and results presented herein are part of a collaborative effort including myself, Peter Weddle, Dr. Karakaya, Dr. Diercks, and Dr. Kee. Permissions can be found in Appendix C.

chemistries.

The present work is the first to make concrete connections between ideal pore models (i.e., along the lines of the Thiele modulus) and reconstructed pores from actual catalyst washcoats. This approach provides significant new insight and quantitative approaches for incorporating microscale knowledge into approximate models at the macroscale.

4.1 FIB-SEM experiments

The FIB-SEM experiments consist of first extracting a small sample of washcoat on substrate material. For this study, a commercial Rh-γAl_2O_3 CPOX washcoat supported on cordierite (supplied by Umicore AG) was used (see Figure 4.1). Both for mechanical support and improved SEM imaging, the washcoat was impregnated with a specialized epoxy doped with a conductive polymer. Further processing is required to expose the washcoat for FIB-SEM imaging. During milling, a Ga-ion beam is used to remove 100 nm of material from the exposed epoxy-washcoat face. A SEM image is collected of the newly exposed surface, each pixel of the resulting image representing approximately 23 nm. The milling and imaging process was repeated until 300 images had been collected. The total collected volume was approximately 30.0 μm × 46.5 μm and the full depth of the washcoat, roughly 15.0 μm. For full details of the FIB-SEM experiments, the reader is referred to Karakaya et al. [84]

4.2 FIB-SEM data processing

Raw data from FIB-SEM experiments are unprocessed, gray-scale images and are numbered in the hundreds. A critical component in 3D reconstruction is the proper phase discrimination between epoxy filler and actual washcoat structure. Simply applying a basic thresholding scheme to the unprocessed images to discriminate between phases is problematic. Images collected via FIB-SEM often have to be done so with the collector at an oblique angle to the exposed face, in this case 52° relative to the milling direction. The perspective of the FIB-SEM data then has to be corrected. This leads to variations in exposure within a single image, and across multiple images, often leading to poor or inaccurate thresholding re-

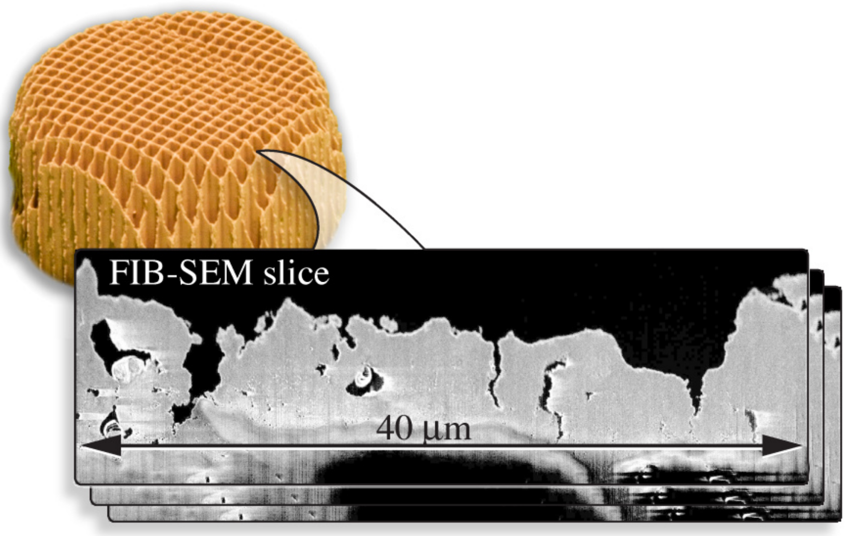

Figure 4.1: Umicore CPOX catalyst monolith and example FIB-SEM images.

sults. Additionally, the effect known as curtaining shown in Figure 4.2 is the result of density and material variability during the ion-milling operation. These undulations, appearing as semi-consistent lines in the FIB-SEM data interfere with phase information. This curtaining, when thresholded, leads to artifacts in the phase data that can be quite significant.

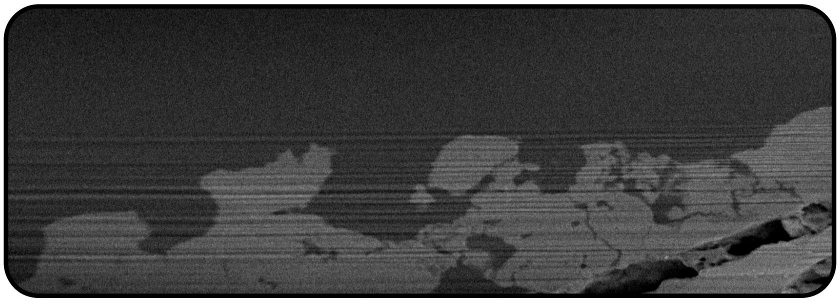

Figure 4.2: An example FIB-SEM image showing catalyst support material (lighter) and impregnated epoxy material (darker). The curtaining effect is apparent by the horizontal lines in the image, making phase discrimination more difficult and inaccurate.

In order to mitigate these problems and produce an accurate discrimination between phases, these issues must be addressed using an automated approach. Processing by hand hundreds of images is simply not practical. First, all the images are averaged to determine any systematic exposure variance that may results from the particular angle-of-incidence that the SEM images were captured at. Correcting for this variance leaves all the images, on average, with equal contrast from left to right, top to bottom. Removing the curtaining is more involved.

Due to the nature of the ion-milling operation, the curtaining appears consistently in one direction as roughly equally spaced lines. These properties make a notch filter particularly useful in removing the lines. A notch filter is a signal processing technique that is designed to remove a particular, generally small, band of frequencies from a larger signal. In the case of an image, a two-dimensional Fourier transform can be used to disassemble the 2D data into its constituent frequency components. Figure 4.3 is the 2D Fourier transform of the FIB-SEM data in Figure 4.2. Lighter pixels indicate a greater contribution of that particular frequency while darker pixels indicate less. Pixels at the extremities of the image represent higher-frequency content while pixels in the interior represent lower-frequency content, with the center pixel indicating DC or the constant offset of the image. Frequencies in the FIB-SEM image that are largely in a single direction, for example in the horizontal direction, will appear on the center horizontal line in the Fourier transform image. Similarly, frequencies largely in the vertical direction will appear on the center vertical line. All other frequencies will appear at some angle between those two. The black boxes shown in Figure 4.3 represent the approximate location of the frequency content contained in the curtaining effect seen in Figure 4.2. By zeroing out, or notching, those particular frequency components, and then using the inverse Fourier transform to recover the filtered image, the curtaining can be removed or at least reduced significantly without compromising the original phase data. The top image in Figure 4.4 is the FIB-SEM image again but after having been filtered. It is clear that the curtaining effect has been by and large removed while preserving phase information.

Once filtered, the phases are binarized using an adaptive thresholding technique known as Otsu's Method [86]. Otsu's method exhaustively searches threshold values selecting the

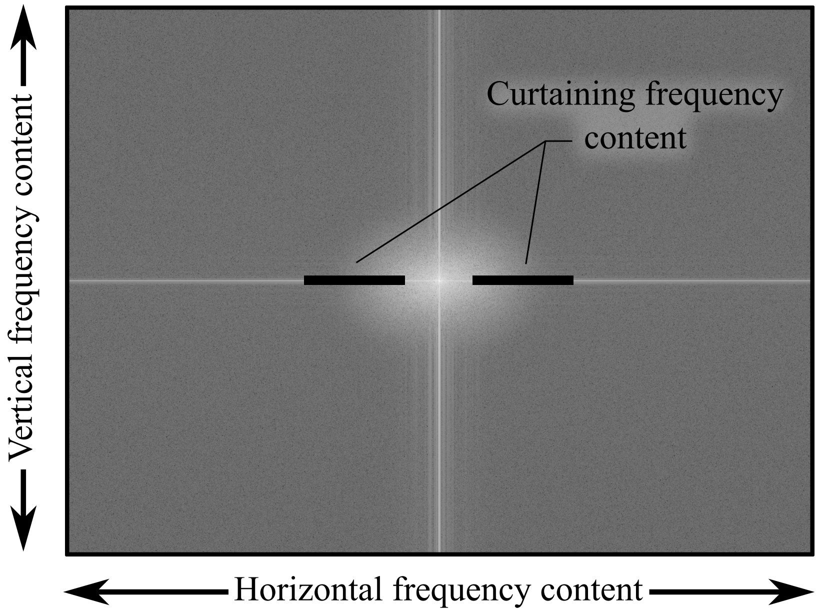

Figure 4.3: A two-dimensional Fourier Transform of the raw FIB-SEM image data. Frequency information in the horizontal and vertical direction are displayed as light or dark pixels in the image. The horizontal curtaining frequency content is largely captured by the black boxes shown.

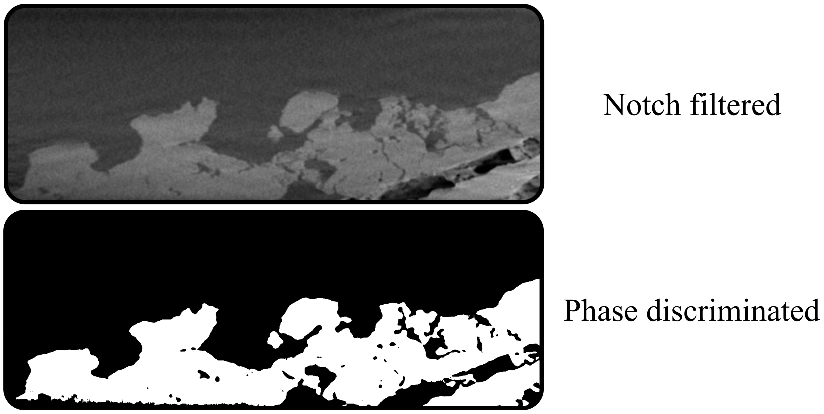

Figure 4.4: Example FIB-SEM images showing micron-scale washcoat characteristics. The top image shows a FIB-SEM image after the notch filter has been applied to remove curtaining and the bottom shows the same data after phase discrimination.

value that minimizes intra-class variance and maximizes inter-class variance. An example image distribution and optimal threshold value can be seen in Figure 4.5. Prior to exposure correction and notch filtering, the bi-modal distribution seen in Figure 4.5 is not apparent. After processing, the optimal threshold, as shown, can be calculated via Otsu's Method. The binarized image is shown on bottom of Figure 4.4.

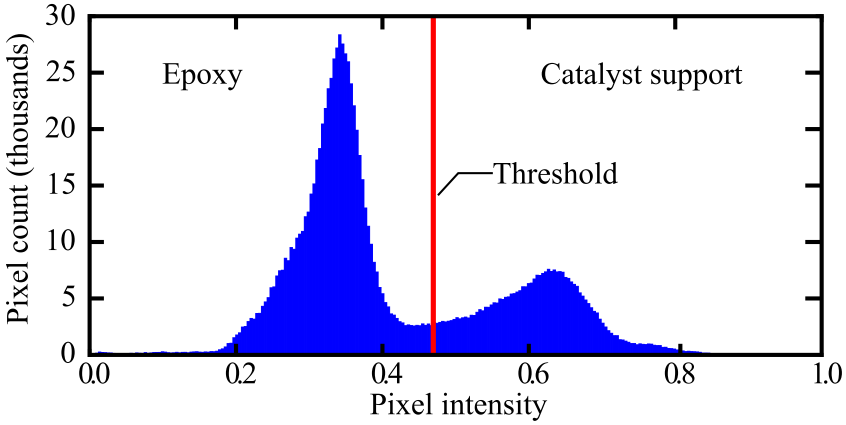

Figure 4.5: Pixel intensity distribution for the filtered image. Exposure correction and notch filtering have resulted in two distinct classes of pixels as evidenced by the bi-modal distribution. The optimal threshold as calculated by Otsu's Method is shown in red.

While each image is corrected to have roughly equal exposure across its width and height, variations from one image to the next can be significant. A single threshold value across all images will produce poor results. By employing an adaptive thresholding technique, each image may have a different optimal threshold, but the overall discrimination process will be more accurate. Once the FIB-SEM images are processed and binarized, they are ready for reconstruction.

4.3 Microstructural reconstruction

Reconstruction is done using the medical imaging software Mimics. Mimics uses the phase information from the FIB-SEM images to reconstruct in 3D the original washcoat structure. A reconstructed washcoat volume, with some cropping, is shown in Figure 4.6.

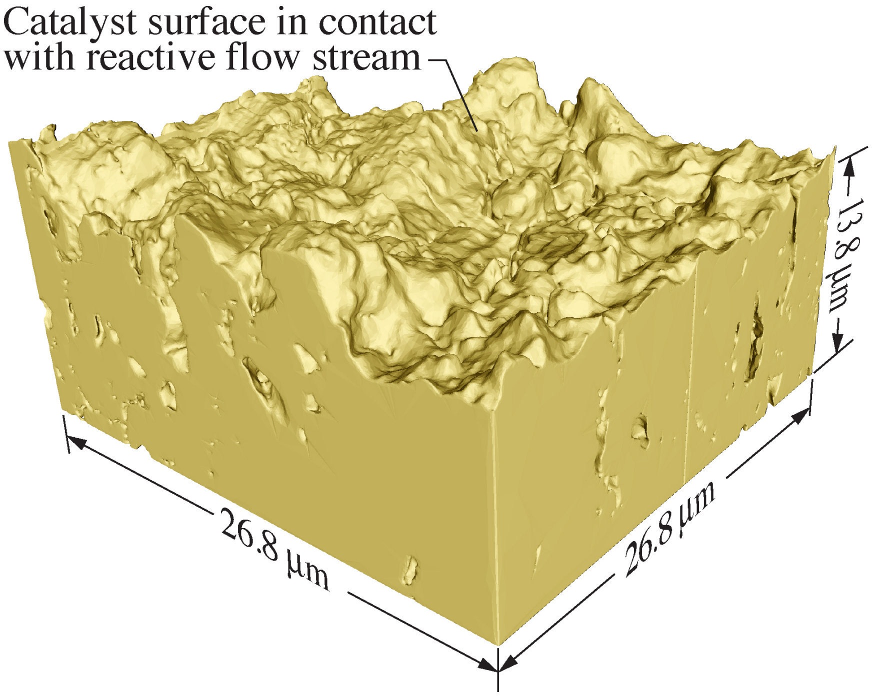

Figure 4.6: A three-dimensional reconstruction of catalyst washcoat.

The microstructure is clearly different from packed spheres or regular cylindrical pores (cf., Figure 1.3). It is largely solid, with a highly textured top surface. A variety of features that resemble cracks, fissures, and crevices penetrate into the washcoat.

Fully resolving the washcoat pore volume for the purpose of simulating the catalytic performance is simply too computationally expensive. Instead, a random sampling of individual pores are extracted from the larger washcoat structure. Figure 4.7 illustrates five example pore volumes.

The pore volumes span a range of shapes and sizes with some characterized by long spindly features while others are more crevice-like. Along with graphical representations of each pore volume, Figure 4.7 presents each respective pores surface area as a function of depth into the pore. A range of relationships is seen. Some contain most of the available reactive surface area near the surface (e.g., pore volume 1 and 5) tapering off near the bottom. Others have an inverse relationship with most catalytic area near the bottom (e.g., pore volume 4 and 3). Pore volume 2 has a roughly even distribution of catalytic area along

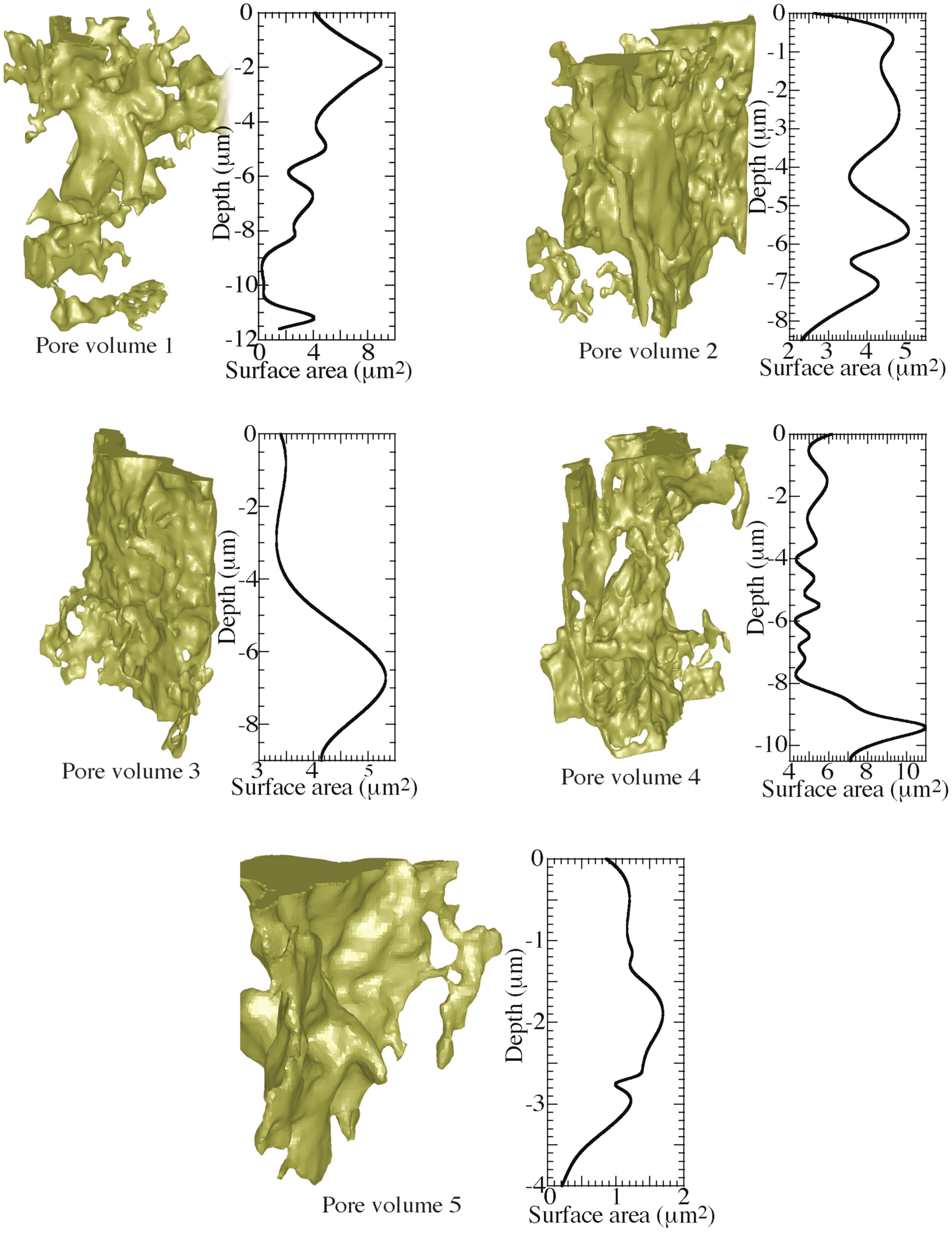

Figure 4.7: Five example pore volumes extracted from the larger washcoat structure. Plotted along side each pore volume is the available catalytic area as a function of pore depth.

its depth.

4.4 Microstructural modeling

As generalized washcoat performance relations are the goal, the formulation of the reaction-diffusion problem in the complex pore geometry is kept as general as possible. The model assumes only two generic gas-phase species, A and B. The catalytic surface chemistry is represented simply as a first-order irreversible reaction A → B, with a rate constant of k. Gas phase chemistry is not considered. Within the pore volume, steady-state gas-phase diffusion of A is represented as

$$\nabla \cdot (D_{\text{eff}} \nabla C_{\text{A}}) = 0 \ , \tag{4.1}$$

where C_{A} represents the concentration of A and D_{eff} is an effective diffusion coefficient. At the length scales considered, molecule-wall collisions can represent an appreciable fraction of molecule interactions. As such, the effective diffusion, D_{eff}, may be a combination of Knudsen and bulk diffusion [87]. This formulation neglects any pressure variations and convective fluid flow within the microstructure, which is usually a good assumption in micro-scale pores. The active catalyst is assumed to be uniformly distributed over the entire surface of the pore volume. Finally, the model assumes isothermal conditions.

Equation 4.1 is an elliptic partial differential equation whose solution requires boundary conditions. At the gas-surface interfaces within the pore-volumes a flux matching boundary condition is enforced as

$$\mathbf{n} \cdot D_{\text{eff}} \nabla C_{\text{A}} = k C_{\text{A}} \ , \tag{4.2}$$

where **n** is the outward-pointing normal unit vector at the catalyst surface. There may be on the order of 10,000 finite-volume surface elements where Equation 4.2 applies. At the top of the pore volume (where the pore volume opens to the flow channel), the mole fraction of A is assumed to be unity. In some circumstances, a particular pore-volume feature may intersect with the edge of the full three-dimensional volume (i.e., Figure 4.6). In this case, symmetry boundaries are enforced.

With the aim of generalizing performance metrics, the model can be put into dimensionless form using characteristic scale factors. The length scale is defined as

$$L = \frac{V_{\mathrm{p}}}{A_{\mathrm{s}}} \ , \tag{4.3}$$

where V_{p} and A_{s} are a pore volume's volume and surface area, respectively. Although the geometry is complex, these values can be easily extracted from the three-dimensional reconstructions. The characteristic concentration is taken to be $C_{\mathrm{A,top}}$, which is assumed to be pure species A at the top of the pore. Using these scale factors, the dimensionless variables of the problem are

$$\hat{C}_{\mathrm{A}} = \frac{C_{\mathrm{A}}}{C_{\mathrm{A,top}}} \ , \qquad \hat{x} = \frac{x}{L} \ , \qquad \hat{y} = \frac{y}{L} \ , \qquad \hat{z} = \frac{z}{L} \ . \tag{4.4}$$

Upon transformation with these scale factors, the dimensionless form of the conservation equation and boundary condition can be expressed as

$$\nabla^2 \hat{C}_{\mathrm{A}} = 0 \ , \tag{4.5}$$

$$\mathbf{n} \cdot \nabla \hat{C}_{\mathrm{A}} = \mathrm{Da} \ \hat{C}_{\mathrm{A}} \ . \tag{4.6}$$

A single dimensionless parameter, the Damköhler number, appears in the boundary condition,

$$\mathrm{Da} = \frac{kL}{D_{\mathrm{eff}}} \ . \tag{4.7}$$

The Damköhler number Da is parameterized by the first-order kinetic rate constant k, the effective diffusion coefficient D_{eff}, and the length scale, L. Essentially, the Damköhler number characterizes the balance between the rate of diffusion and the rate of reaction. A high Damköhler number indicates a diffusion limited regime while a low Damköhler number indicates a kinetically limited regime.

4.4.1 Catalytic performance

Once a solution is found for a particular pore volume, summary performance metrics can be evaluated. Consider first the product species flux (here, species B) emerging from the pore opening, where the pore meets the flow channel. The flux can be evaluated as

$$J_{\mathrm{p}} = \frac{\int_{\mathrm{top}} D_{\mathrm{eff}} \nabla C_{\mathrm{B}} \cdot \mathbf{n} \, \mathrm{d}A}{A_{\mathrm{p}}} \, , \tag{4.8}$$

where A is the surface defining the pore-volume opening to free-stream flow, and A_{p} is the total pore-volume opening area. The integral is needed because the solution is represented locally on the discrete mesh network.

It is useful to normalize pore flux by the flux that would be produced by a catalytic flat plate with the same surface area as the pore-opening area. Continuing to assume first-order kinetics and fixed composition of species A, the flat-plate flux can be written as

$$J_{\mathrm{o}} = C_{\mathrm{A,top}} k \; . \tag{4.9}$$

The normalized pore flux Γ_{p} follows as

$$\Gamma_{\mathrm{p}} = \frac{J_{\mathrm{p}}}{J_{\mathrm{o}}} = \frac{\int_{\mathrm{top}} D_{\mathrm{eff}} \nabla C_{\mathrm{B}} \cdot \mathbf{n} \, \mathrm{d}A}{C_{\mathrm{A,max}} k \; A_{\mathrm{p}}} \; . \tag{4.10}$$

In dimensionless terms, which is the form delivered from the three-dimensional simulations, the normalized effective product flux can be written as

$$\Gamma_{\mathrm{p}} = \frac{1}{\mathrm{Da}} \frac{\int_{\mathrm{top}} \nabla \hat{C}_{\mathrm{B}} \cdot \mathbf{n} \mathrm{d}\hat{\mathrm{A}}}{\hat{A}_p} \; . \tag{4.11}$$

The normalized flux compares the catalytic performance of a pore to an equivalent-area flat washcoat. A value of unity for Γ_{p} indicates that a pore is producing an equivalent product species flux as a flat catalytic surface of the same area as the pore opening.

Another measure of pore performance is the pore effectiveness η_{p}, which is evaluated as

$$\eta_{\mathrm{p}} = \Gamma_p \frac{A_{\mathrm{p}}}{A_{\mathrm{s}}} \; . \tag{4.12}$$

The pore effectiveness measures the flux of product leaving the pore volume compared to the maximum possible flux if all catalytic surfaces were exposed to free stream conditions. The pore effectiveness would unity if there were no mass-transport limitations within the pore.

Yet another relevant measure of washcoat performance is the pore depth beyond which any additional catalyst is unused. If reaction rates are high (relative to diffusion), then most reaction occurs near the pore opening and relatively shallow pores are appropriate. The present study measures the pore depth $\hat{Z}_{95}$ above which 95% of the catalytic reaction has been completed. This measure has relevance to the above discussed $F_{\text{cat,geo}}$. Given certain reaction-diffusion regimes, a significant portion of the measured catalytic surface area considered in $F_{\text{cat,geo}}$ may not be available for reaction. This will be discussed further in Section 4.8.2.

4.4.2 Reconstructed pore results

The five pore volumes were meshed in ANSYS TGRID and the 3D reaction-diffusion problem solved in ANSYS Fluent. Each pore volume was simulated with five Damköhler numbers from $10^{-5} \leq \text{Da} \leq 10^{-1}$. For full details and results, the reader is referred to Karakaya et al., 2015 [84]. For the purposes of the discussion here, only summary results are presented. As an example solution, Figure 4.8 illustrates concentration contours for species A for pore volume 1 at various Damköhler numbers.

For higher Damköhler numbers, where the kinetic rate is fast compared to diffusion, the reaction penetration is limited to relatively small depths. For Damköhler numbers 10^{-3} and 10^{-4}, the tortuous nature of the pores and constrictions in the diffusion path become apparent. For very low Damköhler numbers, the entirety of the pore reaches near free stream conditions and all of the catalyst is being used effectively. The solution for $\text{Da} = 10^{-1}$ is trivial as reactant species A fails to penetrate the pore at all, and is therefore not shown.

For the purposes of generating simplified pore performance relations for upscaling, the metrics outlined in Section 4.4.1 were measured for each of the five reconstructed pore volumes. Figure 4.9 presents a summary of these performance metrics as a function of Damköhler number.

At high Damköhler numbers, very little of the pore depth is used. As such, pore effectiveness, effective pore flux, and reaction depth for all five pore volumes are at a minimum. While some differences are apparent, the pore effectiveness and reaction depth for all five pores generally follow the same trend: at their minimum at high Damköhler numbers and

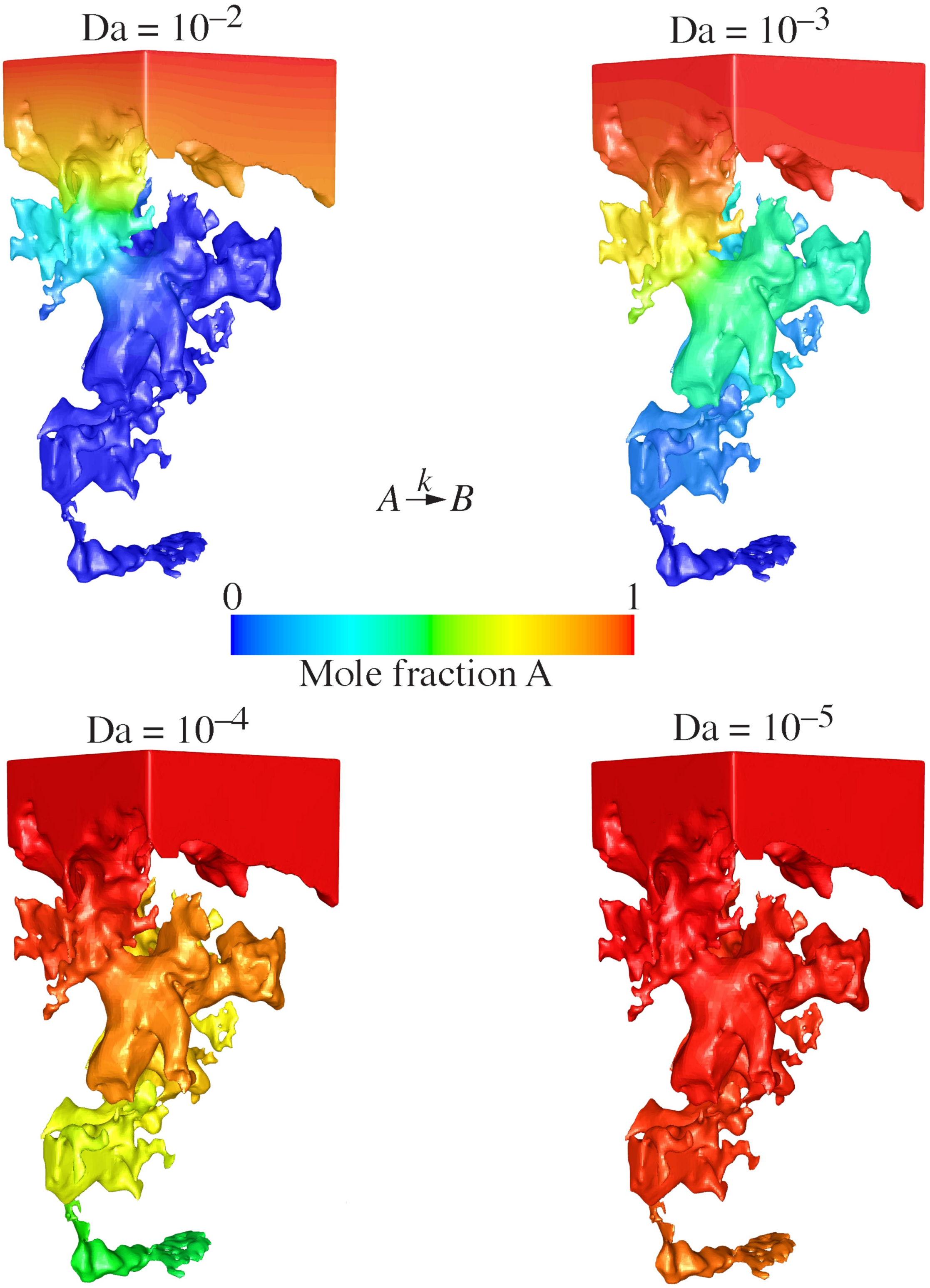

Figure 4.8: 3D reaction-diffusion solutions for Pore Volume 1 at various Damköhler numbers.

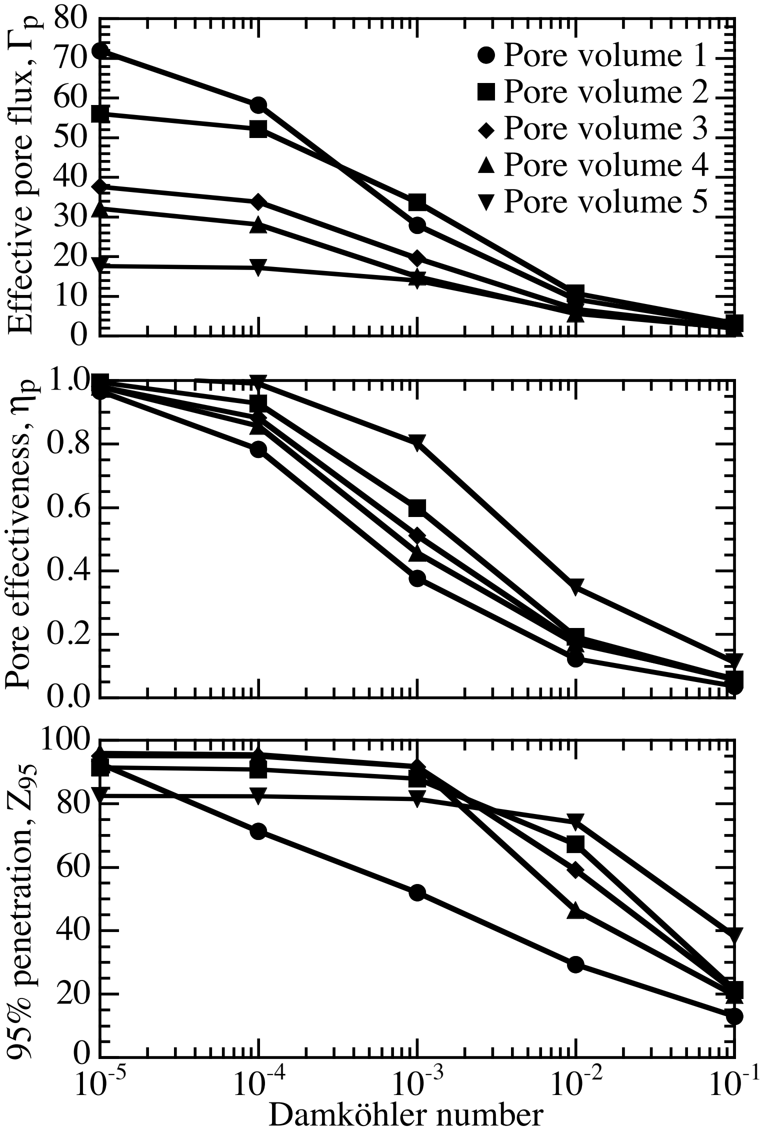

Figure 4.9: Effective pore flux Γ_{p}, pore effectiveness η_{p}, and reaction depth Z_{95} are shown versus Damköhler number.

asymptoting to unity (or 100% in the case of Z_{95}) at Da $= 10^{-5}$. One exception would be the reaction depth of pore volume 1, which tends to under-perform compared to the other four until eventually reaching a reaction depth of 100% at highly kinetically limited conditions. This is likely due the particularly tortuous nature of pore volume 1.

The largest differences from one pore volume to another appear in effective pore flux at low Damköhler numbers. At low Da, the full depth of the pore is taking part in the catalytic chemistry highlighting the morphological differences from one pore to another, namely the reactive surface area.

Characterizing actual, physically reconstructed washcoat pores has provided insight into the chemical, transport, and morphological factors in play in catalyst washcoats. The following sections will develop generalizations to apply the insight learned here to simplified models and eventually full washcoat performance.

4.5 Cylindrical pore model

In seeking generalization for a full washcoat, it is useful to first develop relations based on single pore performance and then upscale. A lower-order model is sought, but one that can be quantitatively informed by characteristics of the actual catalyst microstructures. The two-dimensional cylindrical-pore model developed here is an extension of widely used models based on the Thiele modulus [35, 36, 2]. The extensions are motivated by the need to be more compatible with models of detailed reconstructed washcoats developed in the previous sections.

4.5.1 Thiele modulus

The Thiele modulus Φ provides a dimensionless representation of a reaction-diffusion process within a bottomless cylindrical pore. Assuming a first-order catalytic reaction, the Thiele modulus may be defined as

$$\Phi = Z\sqrt{\frac{2k}{RD_{\text{eff}}}}\,. \tag{4.13}$$

In this definition, Z and R are the pore's depth and radius, respectively. The rate constant for the single irreversible reaction (e.g., A → B) is represented as k, and D_{eff} is an effective gas-phase diffusion coefficient. When Φ is large, internal diffusion limits the overall rate of reaction. When Φ is small, the surface reaction is the rate-limiting process [36].

With this definition of the Thiele modulus, the reactant composition profile within the pore can be evaluated by solving a well known and straightforward ordinary differential equation. The pore effectiveness can be evaluated from the solution to the Thiele problem as [36]

$$\eta_{\mathrm{T}} = \frac{\tanh \Phi}{\Phi}. \tag{4.14}$$

The Thiele pore effectiveness represents the catalytic activity of the pore relative to the catalytic activity if the reactant composition within the entire pore volume were the same as at the top pore opening. Of course, $\eta_{\mathrm{T}} \leq 1$ because the reaction-diffusion processes within the pore deplete the reactant concentration as a function of depth within the pore.

4.5.2 Two-dimensional cylindrical pore

The cylindrical pore model developed here departs from the Thiele approach in two ways. First, the gas-phase diffusion problem is two dimensional, with axial and radial coordinates being the independent variables. Second, the catalytic bottom surface of the pore is included. As illustrated in Figure 4.10, the pore geometry is characterized by its depth Z and radius R. The pore opening has an area of $A_{\mathrm{p}} = \pi R^2$. The total top-surface area (pore opening plus catalytic surface surrounding the pore opening) is designated as A_{o}. The model solves the axisymmetric reaction-diffusion problem within the pore volume.

As was the case for the Thiele approach, and the reconstructed pore volume models, the simplified pore model considers only two generic gas-phase species. A first-order irreversible reaction (A → B, with rate constant k) proceeds at the gas-catalyst interfaces. The problem is assumed to be isothermal and isobaric.

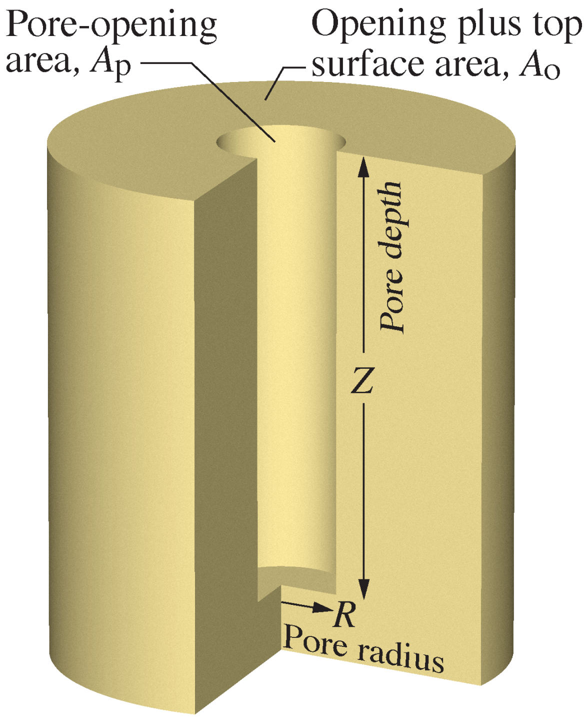

Figure 4.10: Illustration of an idealized cylindrical pore plunging into a washcoat.

The species diffusion problem is solved in the same fashion as the reconstructed pore volumes via Equation 4.1.

Especially in the context of using the cylindrical-pore model to assist interpretation of actual pore microstructures, there is value in representing the cylindrical-pore model in dimensionless variables. The characteristic length scale is taken to be

$$L = \frac{V_\mathrm{p}}{A_\mathrm{s}}, \tag{4.15}$$

where V_p and A_s are the pore volume and surface area, respectively. In this fashion, the simplified pore model is made dimensionless in an analogous way to the reconstructed pore volumes. Thus, the dimensionless variables are

$$\hat{z} = \frac{z}{L}, \qquad \hat{r} = \frac{r}{L}, \qquad \hat{C}_\mathrm{A} = \frac{C_\mathrm{A}}{C_\mathrm{A,top}}. \tag{4.16}$$

As before, the Damköhler number emerges at the boundary condition for the catalytically active surface. Unlike before, though, the Damköhler number does not fully characterize the simplified pore model. The two-dimensional solutions also depend on the pore aspect ratio,

$$\alpha = \frac{Z}{R}. \tag{4.17}$$

For the cylindrical pore, the characteristic length scale (Equation 4.15) is easily written as

$$L = \frac{\pi R^2 Z}{2\pi R Z + \pi R^2} = \frac{RZ}{2Z + R} = \frac{Z}{2\alpha + 1}. \tag{4.18}$$

The computational domain for solving Equation 4.5 is

$$0 \leq \hat{z} \leq (2\alpha + 1), \qquad 0 \leq \hat{r} \leq \left(2 + \frac{1}{\alpha}\right). \tag{4.19}$$

The reason to consider the two-dimensional problem and use the particular characteristic length scale (Equation 4.15) is to assist in establishing relationships with the computational simulations using the actual geometric complexity of reconstructed microscale pore volumes. The characteristic length scale ($L = V_\mathrm{p}/A_\mathrm{s}$) can be extracted computationally from the reconstructed pore geometry. Although the cylindrical-pore model and complex-pore model are best characterized with the Damköhler number, it is useful to consider the relationship between the Thiele modulus (Equation 4.13, applicable for a one-dimensional cylindrical pore model) and the more general Damköhler number. For the two-dimensional cylindrical pore, the relationship depends on the aspect ratio as

$$\Phi = \sqrt{2\,\mathrm{Da}\,\alpha(2\alpha + 1)}. \tag{4.20}$$

4.5.3 Computational solution

Solving Equations 4.5 and 4.6 in the context of the two-dimensional pore represents a linear, elliptic, boundary-value problem. In principle, the problem is solvable analytically using separation of variables, leading to an infinite-series solution. The present study solves the problem computationally. Following finite-volume discretization on a uniform axisymmetric mesh network, the resulting linear system of algebraic equations is easily and rapidly solved by an iterative conjugate-gradient method. The computational solution is programmed in Python. The problem is solved for a large range of aspect ratios $10^{-2} \leq \alpha \leq 10^{3}$ and for five

Damköhler numbers $10^{-5} \leq \mathrm{Da} \leq 10^{-1}$.

4.6 Cylindrical and reconstructed pore performance

The cylindrical-pore model is exercised over a wide range of pore aspect ratios and Damköhler numbers to predict performance metrics. The cylindrical-pore simulation results are directly compared with results from the five reconstructed pores reported in Section 4.4.2.

4.6.1 Effective pore flux

Figure 4.11 shows predicted effective pore flux Γ_{p} as a function of Damköhler number and pore aspect ratio α. At small aspect ratios, the pore resembles a shallow disk, which approaches flat-plate behavior. At large α, the effective pore flux depends greatly on the Damköhler number, and hence on the competition between reaction and diffusion processes. At low Da and high α the effective pore flux is large, meaning that the catalyst area is used effectively throughout the pore.

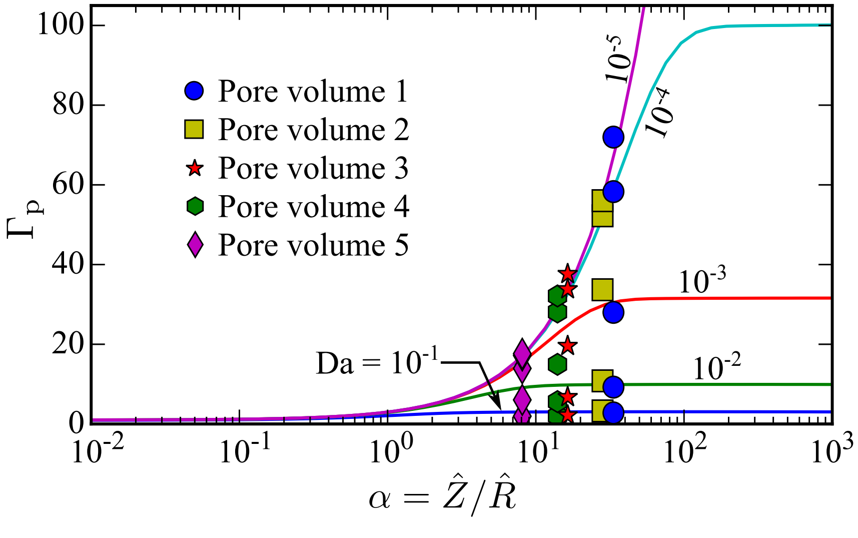

Figure 4.11: Effective pore flux Γ_{p} as a function of aspect ratio and Damköhler number for the cylindrical pore model (lines). The symbols represent simulated results from the three-dimensional reconstructed pore volumes.

The symbols on Figure 4.11 show results from the five reconstructed pore-volume simulations. These simulations are based on the specified Damköhler numbers, but with the geometrically complex reconstructed pore microstructures. Each of the simulated results predicts the effective pore flux Γ_p. Thus, each result can be placed onto Figure 4.11, on the line associated with the specified Da and the predicted Γ_p. However, doing so leads to a different aspect ratio α for each Damköhler number. Because reconstructed pore geometries are so geometrically complex, there is no unique definition for the aspect ratio. Nevertheless, even an approximate α has value in characterizing the pore performance and relating the performance to the much simpler cylindrical-pore model. In any case, the pore geometry is fixed and cannot change as a function of Damköhler number.

The reconstructed pore-volume symbols are placed onto Figure 4.11 with effective αs that are established for each of the five reconstructed pore volumes. The effective aspect ratio α_eff for a given pore is established by calculating the α that minimizes the root-mean-square distance between the effective pore flux predicted by the reconstructed pores $\Gamma_\mathrm{p,r}$ and the respective $\Gamma_\mathrm{p}(\alpha, \mathrm{Da})$ curve, or

$$\min_{\alpha_\mathrm{eff}} \left(\sqrt{\sum_\mathrm{Da} \left|(\alpha_\mathrm{eff}, \Gamma_\mathrm{p,r}(\mathrm{Da})) - \Gamma_\mathrm{p}(\alpha, \mathrm{Da})\right|^2} \right) . \tag{4.21}$$

The symbols that appear on Figure 4.11 are placed according to α_eff and predicted $\Gamma_\mathrm{p,r}$. Although the Damköhler number is not independently specified, the results show that the points fall very close to the appropriate cylindrical-pore Damköhler-number curves. This process enables the assignment of effective aspect ratios for each of the microstructurally complex reconstructed pore volumes.

4.6.2 Pore effectiveness

Figure 4.12 shows predicted pore effectiveness η_p (Equation 4.12) as a function of Damköhler number and pore aspect ratio α. A pore effectiveness of unity means that the maximum concentration of reactant is reaching all reactive surfaces within the pore. A pore effectiveness approaching zero indicates high diffusive resistance relative to the kinetic rate, limiting access to catalyst surfaces deep within the pore. At small aspect ratios, the pore effectiveness approaches flat-plate behavior (i.e., very shallow pore). However, at small aspect ratios and $\mathrm{Da} = 10^{-1}$ the pore effectiveness doesn't approach unity. Strictly speaking, this is the case for all Da, but is much less apparent for lower Da. This is the result of the normalization used in Equation 4.11. As α shrinks, the characteristic length L tends toward Z and the cylindrical-pore model resembles a flat plate catalytic surface with diffusion length Z. This solution will always underperform with respect to the normalization case $J_\mathrm{o} = C_{\mathrm{A,top}}k$ by varying degrees depending on the Damköhler number.

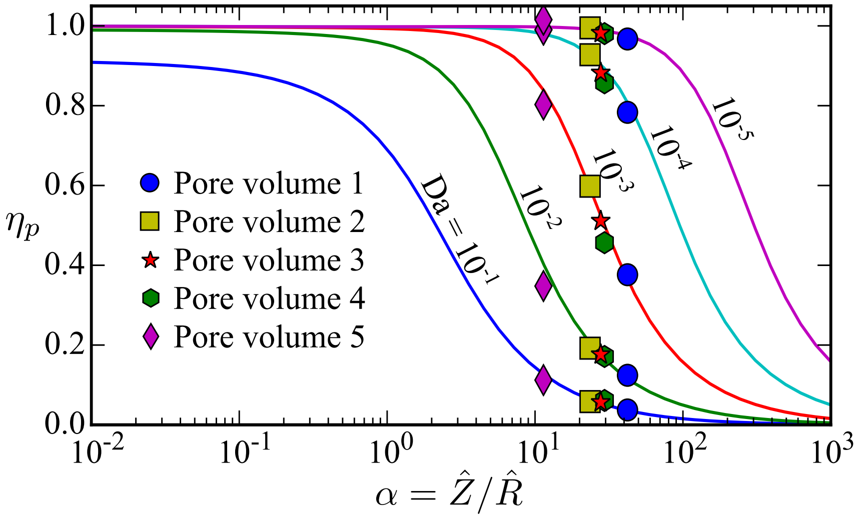

Figure 4.12: Pore effectiveness η_p as a function of aspect ratio and various Damköhler number for the cylindrical pore model (lines). The symbols represent simulation results from the three-dimensional reconstructed pore volumes.

The symbols on Figure 4.12 show the simulation results from the five reconstructed pores. These simulations specify a Damköhler number for the complex pore microstructure, and the three-dimensional simulations predict η_p. As was done in placing reconstructed points on the Γ_p map (Figure 4.11), an effective aspect ratio is established for each of the reconstructed pores on the η_p map. As is the case in Figure 4.11, the reconstructed pores that are fit with effective aspect ratios α lie close to the appropriate Da lines. However, comparing Figure 4.11 and Figure 4.12, it is seen that the average aspect ratios as predicted from the pore effectiveness are slightly higher than are the average aspect ratios as predicted from the effective pore flux. Perhaps not surprisingly, it is difficult to uniquely establish an average aspect ratio for such geometrically complex pore microstructures.

Figure 4.11 and Figure 4.12 both show strong dependence on the Damköhler number. At high Damköhler numbers, both Γ_p and η_p depend weakly on the aspect ratio. However, at low Damköhler numbers Γ_p depends strongly on the aspect ratio, while η_p depends weakly on α.

4.6.3 Pore effectiveness and Thiele approach

Figure 4.13 is a contour plot of pore effectiveness as predicted by the one-dimensional Thiele model η_T (Equation 4.14) and by the two-dimensional cylindrical-pore model η_p (Equation 4.12). Both the Thiele model and the cylindrical-pore model predict the same effectiveness at high α and low Damköhler number. However, the two models deviate somewhat at high Damköhler numbers and low α. This is because the cylindrical model includes a reactive pore bottom and two-dimensional diffusion effects, which are more apparent at low α and high Da.

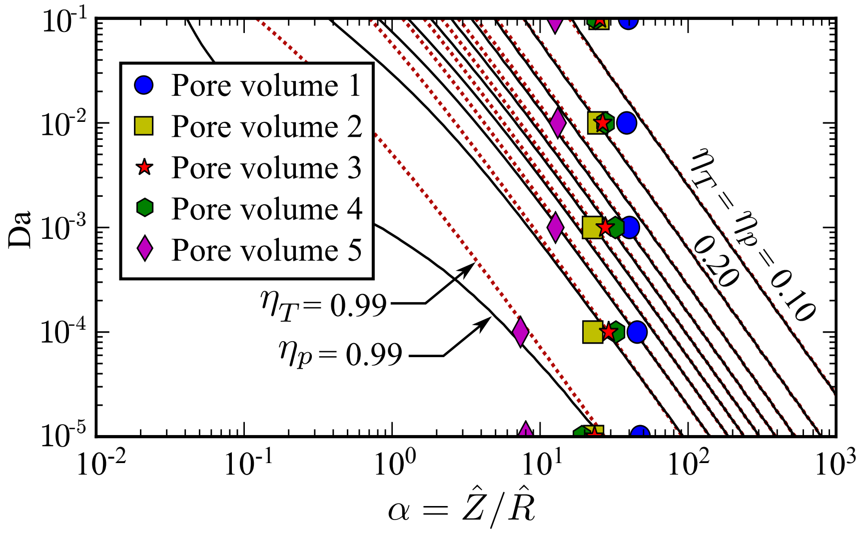

Figure 4.13: Contour map of pore effectiveness η_p as predicted by the cylindrical-pore model (solid lines) and the η_T as predicted by the Thiele modulus approach (dashed lines).The pore effectiveness is a function of Damköhler number and aspect ratio. The symbols represent predictions from the reconstructed three-dimensional pore volumes.

The symbols on Figure 4.13 represent simulation results for the five reconstructed pore volumes. In this case an average pore aspect ratio is not used. Rather, the symbols are placed at specified values of Damköhler number and η_p as predicted from the three-dimensional models of the reconstructed pores. With the exception of Pore 5 at low Da, each pore shows very nearly a constant de-facto aspect ratio.

4.6.4 Depth of reaction

Figure 4.14 illustrates the predicted depth of reaction $\hat{Z}_{95}$ as a function of Damköhler number and pore aspect ratio α. The cylindrical-pore model predicts that at low Damköhler numbers, where the reaction-diffusion problem is kinetically limited, most of the pore depth is effectively used, up to very large aspect ratios. At high Damköhler numbers, on the other hand, much of the pore depth is catalytically ineffective for a large range of aspect ratios.

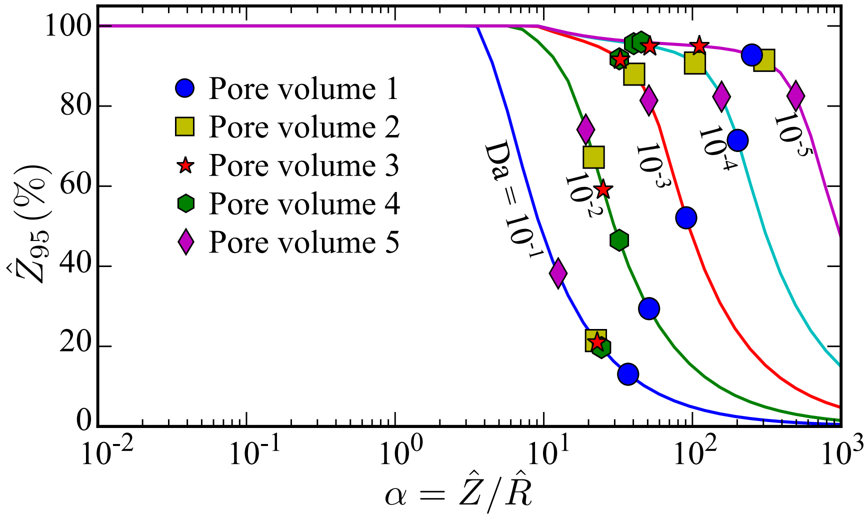

Figure 4.14: Percent of pore depth above which 95% of the reaction occurs as a function of α and Damköhler numbers (lines).The symbols show simulated reaction depths as predicted from the reconstructed pore volumes.

The symbols on Figure 4.14 represent results from the reconstructed pore volumes. The symbols are placed according to the specified Damköhler number and the predicted $\hat{Z}_{95}$. At low Damköhler numbers (with the exception of Pore 1) the reconstructed simulations show that the $\hat{Z}_{95}$ depths tend to reach asymptotic values that depend only weakly on the apparent aspect ratio α. At $\mathrm{Da} = 10^{-1}$, none of the reconstructed pores used more than approximately 30% of the pore depth, with the average being about 23%.

Based on depth-of-reaction results, the apparent aspect ratios vary greatly, with the apparent aspect ratios at low Damköhler numbers being much larger than those inferred from the analysis of Γ_p and η_p. These results indicate that the depth of reaction is highly dependent on unique pore morphology that is not fully captured in the idealized pore model.

4.6.5 Effective pore flux characteristics

Figure 4.15 is a contour map of predicted effective pore flux Γ_p as a function of the Damköhler number and aspect ratio α. For the cylindrical-pore model, this map shows the same information as in Figure 4.11, but presented differently. At high Damköhler numbers and large aspect ratios α, the effective pore flux depends only on the Damköhler number. Conversely at low Damköhler numbers and small α, the effective pore flux depends only on the pore aspect ratio. This behavior suggests an optimum in terms of washcoat fabrication that follows the "knee" in the pore-flux contours.

For a given reaction-diffusion regime, a particular aspect ratio will tend to maximize the product species flux from washcoat pores, beyond which no gains in flux are obtainable. Based upon Equation 4.20 and plotted on Figure 4.15, the knee is approximately bounded by the Thiele modulus in range $0.5 \leq \Phi \leq 2.0$. The measure of effective pore flux as a fraction of the maximum effective pore flux at high α is designated as the maximum effective pore flux $\Gamma_\mathrm{max,p}$.

The fractional pore flux, relative to the maximum possible, may be represented as a function of α and Da.

$$\Gamma_\mathrm{frac,p}\left(\mathrm{Da},\ \alpha\right) = \frac{\Gamma_\mathrm{p}\left(\mathrm{Da}, \alpha\right)}{\Gamma_\mathrm{p}\left(\mathrm{Da},\ \alpha \to \infty\right)}. \tag{4.22}$$

Due to the asymptotic nature of the effective pore flux at high α, a cut-off value of $\Gamma_\mathrm{frac,p} =$ 95% can be used to define the knee. At $\Gamma_\mathrm{frac,p} = 95\%$ the corresponding Thiele modulus is

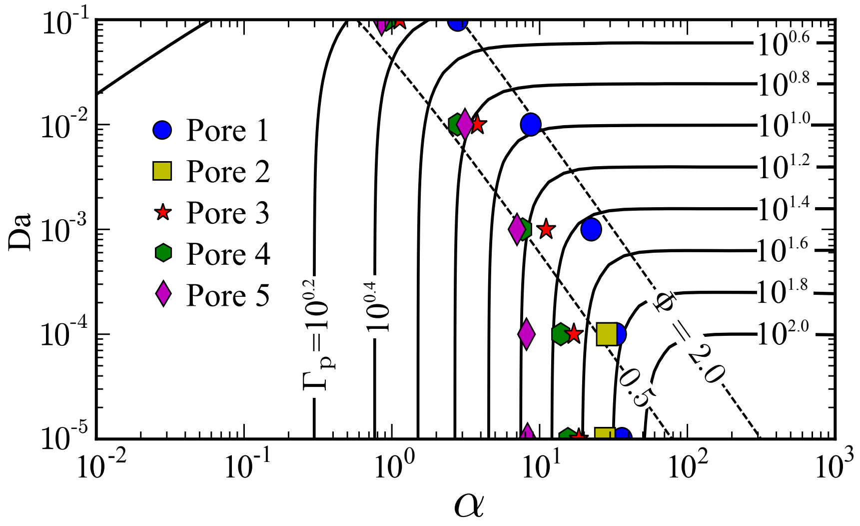

Figure 4.15: Contour of effective pore flux Γ_{p} for a range of Damköhler numbers and aspect ratios.The symbols show simulated effective pore flux for the reconstructed pores. Three points from Pore 2 at high Damköhler numbers cannot be mapped directly on the their appropriate contours and are therefore not shown.

$\Phi_{\mathrm{opt}} \approx 1.832$ or $\eta_{\mathrm{T,opt}} \approx 51.862\%$. The optimal aspect ratio α_{opt} associated with this cut-off parameter can be approximated as

$$\alpha_{\mathrm{opt}} = -\frac{1}{4} + \sqrt{\frac{1}{16} + \frac{\Phi_{\mathrm{opt}}}{4\mathrm{Da}}}. \tag{4.23}$$

This optimum knee in the effective pore flux plot can also suggest an optimum pore depth. If the average effective pore radius $\overline{R}$ for a washcoat can be approximated, then Equation 4.23 can be used to evaluate the optimal washcoat thickness based on effective diffusion and kinetic rate as

$$Z_{\mathrm{opt}} = \sqrt{\frac{D_{\mathrm{eff}}\overline{R}}{2k}\Phi_{\mathrm{opt}}}. \tag{4.24}$$

These optimum variables specify the limit above which no further gains in effective pore flux can be achieved by increasing pore aspect ratios for a given reaction-diffusion regime (i.e., Damköhler number).

The symbols on Figure 4.15 show the simulation results from the five reconstructed pore volumes. In this case (unlike in Figure 4.11) an effective aspect ratio is not used. Instead, the simulated results are shown at the specified Damköhler number and predicted effective pore flux.

At high Damköhler numbers, Pore 1 is operating at a Thiele modulus of approximately $\Phi \approx 1.73$ which corresponds to an effectiveness as predicted by the Thiele approach of $\eta_{\mathrm{T}} = 54.16\%$ and maximum pore flux effectiveness of $\Gamma_{\mathrm{max,p}} = 94.0\%$. At the other end of the scale, Pore 5 has a Thiele modulus of approximately $\Phi \approx 0.662$ with an effectiveness $\eta_{\mathrm{T}} = 87.6\%$ and maximum pore flux effectiveness of $\Gamma_{\mathrm{max,p}} = 58.0\%$. At high Damköhler numbers, the effective pore fluxes for Pore 2 are slightly above the maximum predicted values for the cylindrical-pore model (cf., Figure 4.11). Consequently three effective pore fluxes for Pore 2 cannot be directly mapped onto the appropriate contour and therefore do not appear on Figure 4.15.

The symbols on Figure 4.15 appear to indicate that effective aspect ratios do not accurately represent the pore morphologies at high Damköhler numbers. At high Damköhler numbers, the flux performance suggests effective aspect ratios in the range $1 \leq \alpha \leq 3$. Also, there appears to be a relationship between the reconstructed pore performance at high Damköhler numbers and the contours of Thiele modulus. However, this may well be a computational artifact. As previously noted, for $\Phi \geq 1.832$ the pore-flux performance depends insensitively on α, meaning that any small deviations in normalized flux tend to produce large variations in effective α. Inasmuch as nearly all of the reconstructed pores performed slightly below the idealized pore model at high Damköhler (cf., Figure 4.11) their points on the contour tend toward the knee. However, effective aspect ratios that fall below the knee are particularly insensitive to minor variations in Γ_{p}.

Because the Thiele modulus lumps reaction kinetics and pore morphology into a single parameter, it accurately predicts the pore effectiveness but not the maximum pore performance. This suggests that there is value in defining reaction-transport competition (Da) and pore morphology (α) as two independent parameters to characterize the maximum product flux from a pore. By separating the Thiele modulus into two independent parameters, a nonlinear relationship is found between the Damköhler number and aspect ratio in determining effective pore flux. For example, considering Figure 4.15, at low Damköhler numbers the effective pore fluxes are largely independent of the Damköhler number and vary only between pore microstructures. This is likely due to the transport limitations within the reconstructed pores being the dominant effect compared to the reaction limitations. At low Damköhler numbers the microstructure controls pore performance and thus none of the actual pores reach a fractional pore-flux effectiveness greater than $\Gamma_{\mathrm{frac,p}} \approx 20\%$.

4.7 Effective aspect ratio α

There are inherent inaccuracies in characterizing complex pore morphologies in terms of effective aspect ratios. The reconstructed pore volumes are tortuous and contain a range of narrow constrictions and choke points that cause complex mass-transport resistances. The cylindrical-pore model does not directly consider such complex morphologies, but instead absorbs them into an effective aspect ratio. Thus, simplifying pore morphology solely in terms of effective aspect ratios has varying degrees of success in predicting the performance metrics under consideration.

Figure 4.16 illustrates the average de-facto aspect ratios for the reconstructed pores as predicted by each output parameter. The average aspect ratio $\overline{\alpha}$ is determined for each output parameter and Damköhler number by averaging the de-facto α values as predicted by the reconstructed pore simulations. Additionally, the variations in the de-facto aspect ratios between reconstructed pores is illustrated by the shaded regions, indicating the minimum and maximum bounds of the de-facto pore aspect ratios for each performance metric. It should be noted that the shaded region does not quantify error bounds, only the observed range of de-facto α for the five reconstructed pore volumes that were simulated.

It is clear from Figure 4.16 that the de-facto α predicted by pore effectiveness η_{p} is generally consistent for the full range of simulated Damköhler numbers. This consistent behavior is not simply an effect of the averaging procedure, but is also consistent for each respective reconstructed pore (cf., Figure 4.12 and Figure 4.13). This suggests η_{p} is a good

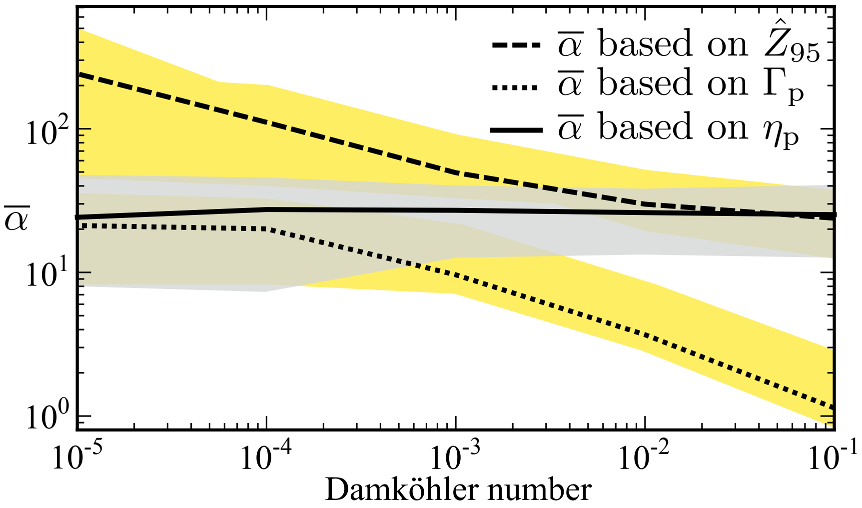

Figure 4.16: Average de-facto aspect ratios $\overline{\alpha}$ as functions of Damköhler number for the three performance metrics.The shaded regions show maxima and minima of the de-facto aspect ratios for the five pores for each performance metric.

performance metric for upscaling the pore results to a full washcoat.

Figure 4.16 suggests that the effective pore flux Γ_p is not well characterized by the effective aspect ratio for all Damköhler numbers. At low Damköhler numbers, $\overline{\alpha}$ based on Γ_p agrees well with the $\overline{\alpha}$ based on η_p, but the two measures diverge at high Damköhler numbers. This divergence likely stems from computational sensitivities. Considering Figure 4.11, the cylindrical-pore model predicts the effective pore flux reasonably accurately for the reconstructed pores. At high Damköhler numbers, however, the de-facto α is very sensitive to small variations in Γ_p (cf., Figure 4.15). For example, at $\mathrm{Da} = 10^{-1}$, the de-facto α as fit by the effective flux of the cylindrical pore model for Pore 1 is 2.79 whereas α_eff as fit by Equation 4.21 is 33.4. The factor of 12 difference between these two α values represents a difference in predicted effective flux of approximately 9%. Thus, approximating $\overline{\alpha}$ based on Γ_p is not as well suited for upscaling as is predicting an effective $\overline{\alpha}$ based on η_p.

The $\overline{\alpha}$ based on $\hat{Z}_{95}$ shows a similar divergence as does $\overline{\alpha}$ based on Γ_p, but at low Damköhler numbers. At high Damköhler numbers, where pore morphology is less important because so little of the pore is actually used, α as fit by $\hat{Z}_{95}$ and η_p agree well. At low

Damköhler numbers pore morphology plays a significant role that is not captured in the idealized pore model. Thus, depth predictions for reconstructed pore volumes deviate from ideal predictions. Therefore $\overline{\alpha}$ based on $\hat{Z}_{95}$ has some predictive capabilities for estimating depth of reaction, especially for mid-to-high Damköhler numbers. Nevertheless, $\overline{\alpha}$ based on $\hat{Z}_{95}$ does not provide a good basis for upscaling for all Damköhler numbers, especially for low Damköhler numbers.

4.8 Upscaling to a full washcoat structure

A single-pore model, whether reconstructed or ideal, can only partially capture the behavior of the full washcoat. To extrapolate to a complete washcoat structure, effective parameters related to geometric area, washcoat depth, pore area, pore density, and average pore radius must be approximated. Figure 4.17 illustrates only the top surface of the reconstructed catalyst sample area. The surface is irregular and highly textured. Even with the detailed geometry from the FIB-SEM reconstruction, unambiguous measures of pore density and pore-opening area are at best difficult.

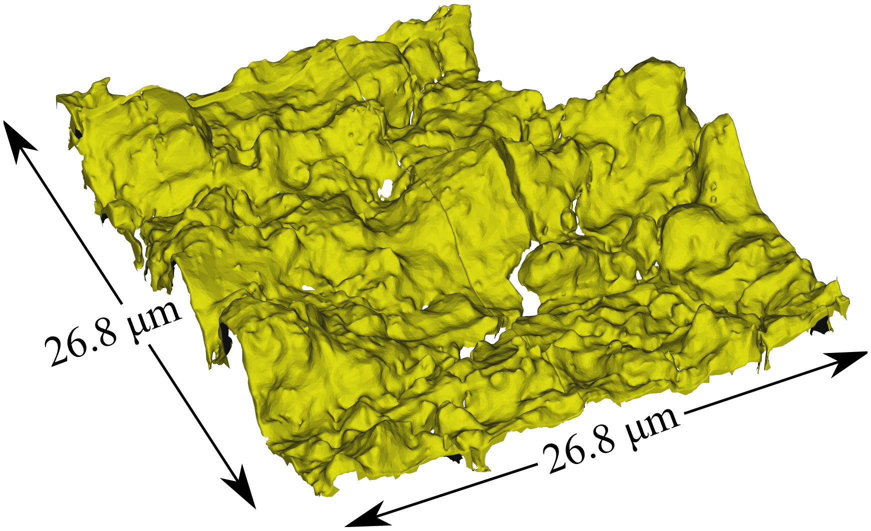

Figure 4.17: Top surface of the reconstructed washcoat.

Table 4.1 tabulates the relevant surface areas and the average aspect ratios of the pores that are extracted from the FIB-SEM reconstruction. These statistics provide some relevant

Table 4.1: Reconstructed washcoat and sample pore volume statistics

Parameter	Value	
Pore opening area, A_p	48.0	μm^2
Total catalytic area, A_c	4270.4	μm^2
External surface area, A_o	1273.3	μm^2
Geometric surface, A_geo	668.4	μm^2
Pore 1 catalytic surface area, $A_{\mathrm{s},1}$	190.5	μm^2
Pore 2 catalytic surface area, $A_{\mathrm{s},2}$	233.7	μm^2
Pore 3 catalytic surface area, $A_{\mathrm{s},3}$	203.9	μm^2
Pore 4 catalytic surface area, $A_{\mathrm{s},4}$	288.9	μm^2
Pore 5 catalytic surface area, $A_{\mathrm{s},5}$	54.9	μm^2
Effective pore-volume aspect ratio based on η_p		
Parameter	Value	
Pore 1 average aspect ratio, $\alpha_{1,\mathrm{eff}}$	43.06	
Pore 2 average aspect ratio, $\alpha_{2,\mathrm{eff}}$	23.59	
Pore 3 average aspect ratio, $\alpha_{3,\mathrm{eff}}$	28.89	
Pore 4 average aspect ratio, $\alpha_{4,\mathrm{eff}}$	33.02	
Pore 5 average aspect ratio, $\alpha_{5,\mathrm{eff}}$	13.33	

clues for upscaling.

4.8.1 Average washcoat geometry

Of course, pore microstructures significantly increase catalytic surface area within washcoat structures. However, depending on the reaction-diffusion processes all the catalyst surface area may not be practically accessible. Thus, developing approaches to design and fabricate optimal pore structures and pore densities has practical value.

A parameter β is introduced to assist the study of pore densities

$$\beta = \frac{A_\mathrm{o}}{A_\mathrm{p}} \; . \tag{4.25}$$

In this definition A_p is the pore-opening area and A_o is the area of the pore opening and the surrounding area (cf., Figure 4.10).

Using data from Table 4.1, the reconstructed washcoat has a measured pore density of $\beta = 26.53$. For the idealized pore model, the external surface area A_o is equal to the geometric surface area A_geo. However, because of the texture in the actual washcoat surface (cf.,

Figure 4.6 and Figure 4.17), the measured A_o for the reconstructed washcoat is approximately twice the projected geometric area.

If the washcoat surface were assumed to be flat and populated by cylindrical pores plunging into the surface (cf., Figure 1.3), the total catalytic surface area A_c would be expressed as

$$A_\mathrm{c} = A_\mathrm{o} + N \times 2\pi \overline{R}\,\overline{Z}, \tag{4.26}$$

where N is the number of pores on the washcoat surface, $\overline{R}$ is the average pore radius, and $\overline{Z}$ is the average depth of the washcoat (assumed to be a good approximation of average pore depth Z). The pore volume is

$$V_\mathrm{p} = N \times \pi \overline{R}^2\,\overline{Z}. \tag{4.27}$$

Combining the above two equations, the average radius can be expressed as

$$\overline{R} = \frac{2V_\mathrm{p}}{A_\mathrm{c} - A_\mathrm{o}}. \tag{4.28}$$

With an effective pore aspect ratio $\overline{\alpha}$ being expressed as

$$\overline{\alpha} = \overline{Z}/\overline{R}, \tag{4.29}$$

the average pore density can be expressed as

$$\overline{\beta} = \frac{2\overline{\alpha}}{A_\mathrm{c}/A_\mathrm{o} - 1}. \tag{4.30}$$

Although developing processes to fabricate washcoats with specific pore densities and pore radii may be difficult in practice, the foregoing relationships assist developing target specifications that are informed by model-based predictions.

4.8.2 Average washcoat performance

Using the cylindrical-pore model, the total flux from the surface (pores and external surface) can be expressed as

$$J_\mathrm{tot} = \frac{J_\mathrm{p} A_\mathrm{p} + (A_\mathrm{o} - A_\mathrm{p}) J_\mathrm{o}}{A_\mathrm{o}}. \tag{4.31}$$

As in the case of a single pore, the normalized flux for the entire washcoat Γ_{tot} is evaluated by normalizing with respect to external surface flux J_{o} as

$$\Gamma_{\text{tot}} = \frac{J_{\text{tot}}}{J_{\text{o}}} = 1 - \frac{1}{\overline{\beta}} + \Gamma_{\text{p}} \frac{1}{\overline{\beta}}. \tag{4.32}$$

The total effectiveness factor for the washcoat follows as

$$\eta_{\text{tot}} = \frac{J_{\text{tot}} A_{\text{o}}}{J_{\text{o}} A_{\text{c}}} = \frac{J_{\text{p}} A_{\text{p}} + (A_{\text{o}} - A_{\text{p}}) J_{\text{o}}}{J_{\text{o}} A_{\text{c}}} \ . \tag{4.33}$$

Using Equations 4.25 and 4.26, and the fact that $A_{\text{o}} = N \times \overline{\beta} \pi \overline{R}^2$ the total pore effectiveness can be simplified further as

$$\eta_{\text{tot}} = \Gamma_{\text{tot}} \frac{\overline{\beta}}{\overline{\beta} + 2\overline{\alpha}}. \tag{4.34}$$

Using the relationships developed above, data from Table 4.1, and performance results from the simulated reconstructed pores, the performance of the washcoat as a whole can be predicted. For example, assuming $\text{Da} = 10^{-3}$, the average effective pore flux for all five samples is $\Gamma_{\text{p,avg}} = 22.06$. Knowing $\overline{\beta}$, the average normalized flux for the washcoat is

$$\Gamma_{\text{tot}} \approx 1.79. \tag{4.35}$$

Using the effective pore aspect ratio $\overline{\alpha}$ for the five samples $\overline{\alpha}_{\text{avg}} = 28.378$, the total washcoat effectiveness is

$$\eta_{\text{tot}} \approx 0.57 \ . \tag{4.36}$$

As the $\hat{Z}_{95}$ measures suggest, significant portions of the total catalytic area may not be accessible for reaction. For example, using the reconstructed area profiles (Table 4.1), the measure of actual catalytic area to geometric area $F_{\text{cat,geo}}$ for the reconstructed washcoat is

$$F_{\text{cat,geo}} = \frac{A_{\text{c}}}{A_{\text{g}}} \approx 6.39. \tag{4.37}$$

Based on the idealized washcoat model, a relationship can be derived for a modified washcoat factor $F_{\text{cat,geo}}(\overline{\alpha}, \overline{\beta}, \text{Da})$, which is a function of the surface's physical characteristics and the reaction-diffusion regime. Using the definitions of A_{c}, A_{o}, and $\overline{\beta}$, the modified $F_{\text{cat,geo}}$ is expressed as

$$F_{\text{cat,geo}} = \frac{\overline{\beta} + 2\overline{\alpha}\hat{Z}_{95}}{\overline{\beta}}. \tag{4.38}$$

Figure 4.18 shows contour maps of $F_{\text{cat,geo}}$ as functions of $\overline{\alpha}$ and $\overline{\beta}$ for five Damköhler numbers. The strong Damköhler number dependence is apparent. For $\text{Da} = 10^{-1}$ and any realistic $\overline{\beta}$, the modified $F_{\text{cat,geo}}$ is unlikely to be above 2 or 3. Alternatively, at $\text{Da} = 10^{-5}$ double-digit washcoat factors are achievable, although only at large α and high pore density.

4.9 Summary and conclusions

Advances in FIB-SEM techniques have enabled the imaging and reconstruction of catalytic washcoats at the micron- and submicron-scale. FIB-SEM images of a commercial Rh-γAl_2O_3 partial-oxidation catalyst washcoat were collected, processed, and reconstructed into a three-dimensional fluid dynamics model. A dimensionless reaction-diffusion problem was developed to provide new insight into chemical, transport and morphological effects on washcoat performance. The physically reconstructed pore volumes are characterized by effective pore flux, pore effectiveness and reaction depth.

A microscale two-dimensional cylindrical-pore model is developed and used to evaluate the same catalytic performance metrics as the physically reconstructed pores: effective pore flux, pore effectiveness, and reaction depth. The pore itself is characterized by an aspect ratio, while the first-order reaction-diffusion competition is characterized by a Damköhler number. This model is a two-dimensional version of the well-known analysis based on a Thiele modulus. The principle reason to develop a cylindrical-pore model is to provide a basis for comparison with geometrically complex, three-dimensional models.

Using the same quantitative performance metrics, predictions from the ideal cylindrical-pore model and the three-dimensional reconstructed pore model can be compared directly. The analysis based on these comparisons yields significant new insight about the performance of actual catalyst washcoats. The geometrically complex microstructures certainly

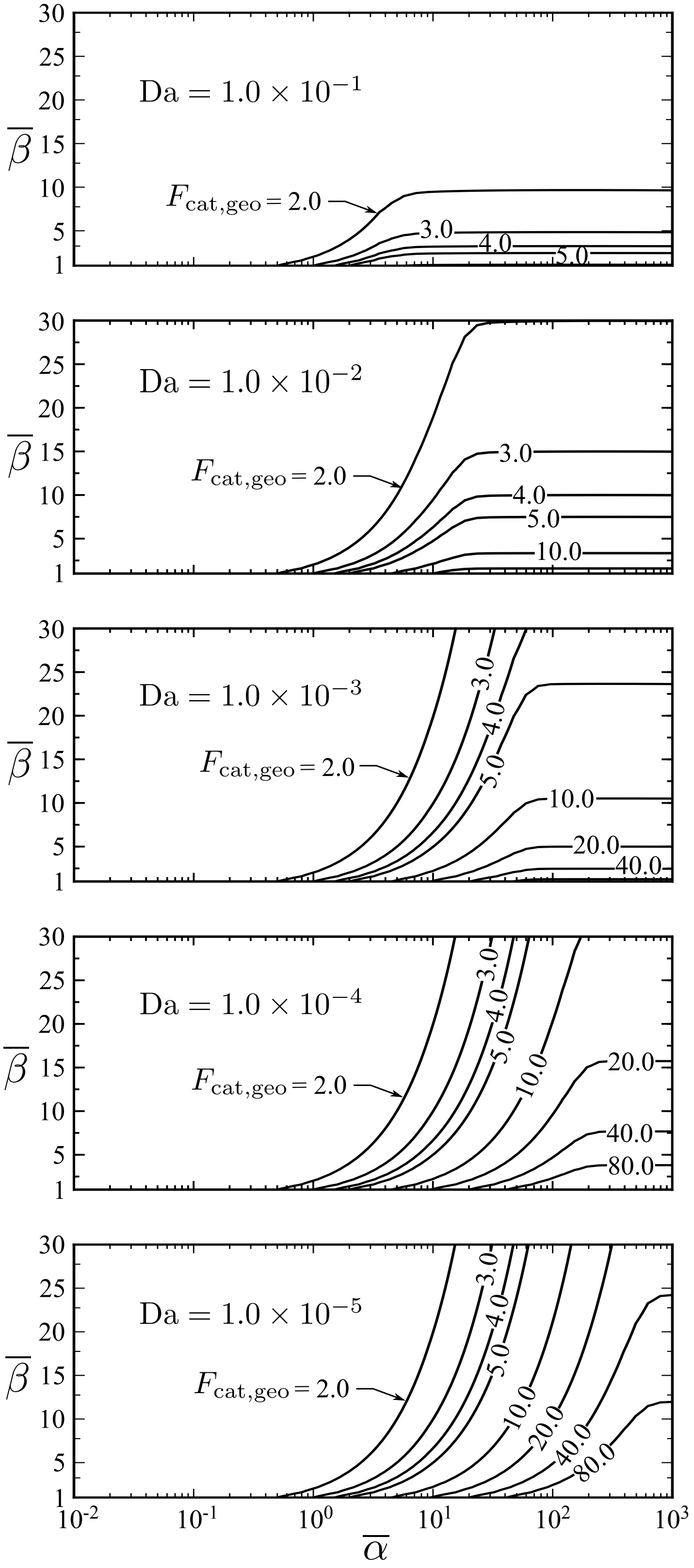

Figure 4.18: Contour maps of $F_{\text{cat,geo}}$ as a function of $\overline{\alpha}$ and $\overline{\beta}$ for five Damköhler numbers.

do not appear as simple cylindrical pores plunging into the washcoat. Nevertheless, there are interesting common features in the performance metrics. By identifying and analyzing such commonalities and trends, the results suggest qualitative and quantitative insights that advance the fundamental understanding of reaction-diffusion processes within catalytic washcoat structures. Such understanding contributes new insight that can assist the improved design and fabrication of washcoat microstructures.

CHAPTER 5
FUTURE WORK

The following sections discuss some potential avenues for continuing the research in the preceding chapters. As before, the three sub-topics will be addressed in turn.

5.1 Ceramic microchannel reactor

With a fully resolved 3D model in hand, important design considerations can be investigated at a reduced cost as compared to physical prototyping. One such opportunity would be a more complete thermal stress analysis of the ceramic reactor body. Ceramics tend to have poor fracture toughness which makes them susceptible to failure via thermal shock or temperature gradient induced stresses [52]. By resolving the full CFD and conjugate heat transfer problem, and with the added benefit of integrated kinetics, a full investigation of the internal thermal gradients can be done. Coupled with a mechanical finite element method (FEM) analysis, the internal stresses can be calculated and geometric features that act as stress magnifiers can be identified and new designs can attempt to reduce these. This becomes even more important when considering integrating CPOX reactions into the backing side flow channels where hot spots can lead to failure.

On the subject of CPOX, a study, which was not done in this work but the tools are in place for it, is the combined simulation of SMR and CPOX within the same reactor model. Blakeley [88] demonstrated CPOX in what is essentially the same ceramic microchannel reactor presented in this work supported with a geometrically simplified model with detailed kinetics. The reactor nor the model were run with combined SMR and CPOX and could provide interesting insights into potential efficiency gains in such an integrated design.

In any embedded system with tightly coupled thermal and chemical devices, optimal control strategies become important. For example, in the case of a SOFC system doing load following, the transient dynamics of each component and subsystem has to be accounted for in order to protect components and provide satisfactory performance. A particular class of control methods known as model predictive control (briefly discussed in Chapter 3) rely on low-order dynamic models to predict behavior of system components and actuate optimal control strategies. Utilizing the ceramic microchannel HEX-reactor model developed here, a study of its thermal and chemical transient dynamics would be generally valuable, but would also be interesting to see of system identification and MPC is something that could be applied.

In Section 2.6.2, a study on potential catalyst deactivation through coke formation was performed. Coking is an ever present problem in catalytic processes and pathways by which it is formed are not always clear. In industry high S/C ratios are typically used to help mitigate coke formation, but that strategy comes with a thermodynamic cost. A recent study by Eßmann et al. has developed a detailed reaction mechanism for the prediction of coke formation during steam reforming of natural gas over rhodium [68]. With this mechanism, utilizing ISAT for accelerated simulation, the current model could be extended for more detailed and temporal predictions of coke formation. Exercising this model could provide design suggestions based on coking predictions. Insights could also be gained for the optimal S/C ratio for catalyst longevity, high hydrogen yield, and minimizing the thermodynamic cost of high steam content.

5.2 Accelerated kinetics modeling

The test case for the acceleration provided by ISAT had practical value to the research on the microchannel HEX-reactor in Chapter 2, but was not a comprehensive test of ISATs performance compared with the myriad of other techniques in the literature. For a different kinetic mechanism, one with different dynamics or more/less species of interest, ISAT may not be the optimal choice. At the limit of ISATs capability it may be that other options outperform. A full exploration of these options for heterogeneous chemistry might yield other, better options. Multi-zone methods are enjoying much success in combustion modeling, but it is unclear if those benefits will transition to heterogeneous chemistry.

An exciting new area of research is in the use of GPU accelerated chemistry simulations [89, 90]. GPUs present a fundamentally different computing architecture compared to traditional processors that have potential for significant speed-up in detailed kinetics simulations. This is still a developing tool for chemistry acceleration, but could potentially provide chemistry solutions for large mechanisms more efficiently than ISAT.

5.3 Catalytic washcoat characterization

Having actual 3D reconstructed washcoat geometry enables a wide range of possible avenues for further study. Extending beyond the simplified dimensionless reaction-diffusion problem, fully resolved detailed kinetics is an obvious next step. By incorporating the more realistic mass action kinetics of a full catalytic mechanism, a more accurate representation of washcoat pores can be investigated. By applying a specific chemistry to the model, the generality developed in presented relations is lost, but it would also serve as a measure of the actual utility of the dimensionless relations. Additionally, resolving detailed chemistry in reconstructed washcoats could inform observed behaviors. For example, Saito et al. developed a reactor specifically designed to measure the catalytic performance of steam reforming with different depths of washcoat [91]. It would be interesting to compare their experimental results with those predicted by reconstructed physical washcoats and the performance relations derived in Chapter 4.

The analysis in this work was done with a steady-state assumption. While many important catalytic processes of interest are steady-state, many are not. The transient thermochemical behavior within washcoat structures, for example during light-off in catalytic converters, is an ongoing area of study [92]. With models already developed, extending this work to include transient behaviors, including the use of dimensionless parameters to generalize the results, can be very valuable.

An obvious simplification in the presented work is that the chemistry occurs at isothermal conditions. For fast reactions or reactions that are highly endo- or exothermic, the thermal gradients established in the washcoat can have an appreciable effect. Investigating the thermal behavior at the microscale in reconstructed washcoats could provide novel insights for washcoat performance and catalyst degradation. The current models would have to be expanded to include the discretization of the γAl_2O_3 support material in addition to the pore volume.

CHAPTER 6
CONCLUSION

Each respective chapter contained concluding sections on the material presented therein. This chapter will serve as an overall summary of the accomplishments of this research.

A three-dimensional model of a novel ceramic microchannel reactor was developed. The model solved flow with conjugate heat transfer and detailed chemical kinetics. This model was validated against flow and thermal data collected during experiments at the CFCC. A thermal analysis was done to highlight the importance of the thermal conductivity of the body material on heat exchanger effectiveness. Despite having a relatively low thermal conductivity at high temperatures compared to commonly used metals, alumina is well suited for microchannel reactors in a counterflow configuration. It was demonstrated that for this particular geometry, low thermal conductivity tended to promote high effectiveness, especially at flow rates at or below 50 SLPM.

An extended model with stainless steel manifolding was validated against the experimental setup and provided insight into thermal losses inherent in the experimental apparatus. Further, the hydraulic losses associated with the microchannel flow and the particular support structures were quantified. For 50 SLPM balanced flow with cold- and hot-flow sides entering at 50 °C and 500 °C, respectively, fully 90% of the pressure drop incurred on the hot flow channel occurs at the microchannel entrance and at the exhaust port. For the cold side, 80% of the pressure drop occurs outside the microchannels.

The model was then used to explore internal conditions not easily accessible by experiment. The average and standard deviation of the temperature of the catalytic surfaces were studied over a wide range of operating conditions. It was found that for a cold flow of 4 SLPM, 50 SLPM backing flow was sufficient to thermally saturate the HEX-reactor. Beyond 50 SLPM, the average temperature of the reactive surface varies only with backing side inlet temperature. Below 50 SLPM, a balance must be struck between backing side flow rate and temperature to achieve the desired thermal conditions on the reactive side.

A detailed chemical mechanism for the steam reforming of methane over rhodium developed by Karakaya [66] was integrated into the model. The thermal burden of internal reforming chemistry was evaluated, which represented a relatively small portion of the overall heat transferred ($Q_{\text{rxn}} \approx 10.0 - 15\%$ for the flows studied). A roughly 20 °C drop in catalytic surface temperature was predicted when reactive flows where compared to inert conditions. A study of adsorbed surface species was done to predict regions within the microchannel reactor that have high potential for coking. The results suggest a strong geometric dependence for CO adsorption, supporting the need for physically representative models.

ISAT, commonly used for the acceleration of homogeneous combustion chemistry, was adapted for transient, heterogeneous chemistry. A transient simulation of SMR in the microchannel HEX-reactor model was used as a test case. Depending on perturbations to the inputs, ISAT delivered 10 – 20 times speed-up factors over FLUENTs internal surface chemistry solver with no appreciable decline in accuracy. These are significant gains with real practical importance and facilitated the kinetics simulations in the HEX-reactor discussed above. For the particular CFD model used as a case study, once the bulk of tabulation was done, chemistry was essentially computed for free. The source for the developed implementation of ISAT has been provided to ANSYS FLUENT and an implementation may appear in a future release.

Finally, FIB-SEM imaging provided nanoscale phase information for actual, commercial washcoat structures. Algorithms were developed to process, filter, and discriminate phase information in the FIB-SEM images to facilitate 3D reconstruction. Five pores were extracted from the reconstructed washcoat and a dimensionless reaction-diffusion problem was solved for each. By posing the problem in dimensionless terms, characterized by the Damköhler number, the catalytic behavior could be generalized. Performance relations, first for pores alone, and then for washcoats as a whole, were developed based on good agreement between reconstructed pores and an idealized 2D cylindrical pore model. The generalized relations suggest optimum washcoat depth based on effective kinetic rates and diffusion coefficients. Additionally a modified washcoat factor was developed to relate the often used multiplicative factor $F_{\text{cat,geo}}$ to a particular reaction-diffusion regime. These have important implications not only on the accurate simulation of washcoat performance but also on washcoat manufacturing.

REFERENCES CITED

[1] R. A. Sheldon. Catalysis: The key to waste minimization. *J. Chem. Technol. Biotechnol.*, 68(4):381–388, 1997. ISSN 1097-4660.

[2] I. Chorkendorff and J. W. Niemantsverdriet. *Concepts of Modern Catalysis and Kinetics*. Wiley, 2005. ISBN 9783527602650.

[3] Z. Anxionnaz, M. Cabassud, C. Gourdon, and P. Tochon. Heat exchanger/reactors (HEX reactors): Concepts, technologies: State-of-the-art. *Chem. Eng. Process.*, 47(12):2029–2050, 2008. ISSN 0255–2701.

[4] A. Stankiewicz and J. Moulijn. Process intensification: Transforming chemical engineering. *Chem. Eng. Prog.*, 96(1):22–34, 2000.

[5] S. G. Kandlikar, S. Garimella, D. Li, S. Colin, and M. R. King. *Heat Transfer and Fluid Flow in Minichannels and Microchannels*. Elsevier Science Ltd, 2006. ISBN 978-0-08-044527-4.

[6] L. Luo, Y. Fan, and D. Tondeur. Heat exchanger: From micro-to multi-scale design optimization. *Int. J. Energy Res.*, 31(13):1266–1274, 2007.

[7] M. G. Khan and A. Fartaj. A review on microchannel heat exchangers and potential applications. *Int. J. Energy Res.*, 35(7):553–582, 2011. ISSN 1099-114X.

[8] R. K. Shah and D. P. Sekulic. *Fundamentals of Heat Exchanger Design*. Wiley, 2003.

[9] M. I. Hasan, A. Rageb, M. Yaghoubi, and H. Homayoni. Influence of channel geometry on the performance of a counter flow microchannel heat exchanger. *Int. J. Therm. Sci.*, 48(8):1607–1618, 2009. ISSN 1290-0729.

[10] K. Foli, T. Okabe, M. Olhofer, Y. Jin, and B. Sendhoff. Optimization of micro heat exchanger: CFD, analytical approach and multi-objective evolutionary algorithms. *Int. J. Heat Mass Transfer*, 49(56):1090 – 1099, 2006. ISSN 0017-9310.

[11] L. Kiwi-Minsker and A. Renken. Microstructured reactors for catalytic reactions. *Catal. Today*, 110(12):2 – 14, 2005. ISSN 0920-5861.

[12] A. Sommers, Q. Wang, X. Han, C. T'Joen, Y. Park, and A. Jacobi. Ceramics and ceramic matrix composites for heat exchangers in advanced thermal systems — A review. *Appl. Thermal Engr.*, 30(11–12):1277–1291, 2010. ISSN 1359–4311.

[13] R. O'Hayre, S. Cha, W. Colella, and F. Prinz. *Fuel Cell Fundamentals.* Wiley, 2009. ISBN 9780470258439.

[14] M. Irani, A. Alizadehdakhel, A. N. Pour, N. Hoseini, and M. Adinehnia. CFD modeling of hydrogen production using steam reforming of methane in monolith reactors: Surface or volume-base reaction model? *Int. J. Hydrogen Energy*, 36(24):15602–15610, 2011. ISSN 0360-3199.

[15] U. Izquierdo, V. Barrio, J. Cambra, J. Requies, M. Güemez, P. Arias, G. Kolb, R. Zapf, A. Gutiérrez, and J. Arraibi. Hydrogen production from methane and natural gas steam reforming in conventional and microreactor reaction systems. *Int. J. Hydrogen Energy*, 37(8):7026–7033, 2012. ISSN 0360-3199.

[16] G. Grasso, G. Schaefer, Y. Schuurman, and C. Mirodatos. Methane steam reforming in microchannel reactors: Technical challenges and performances benefits. *Top. Catal.*, 54(13–15):859–865, 2011. ISSN 1022–5528.

[17] R. Kee, B. Almand, J. Blasi, B. Rosen, M. Hartmann, N. Sullivan, H. Zhu, A. Manerbino, S. Menzer, W. Coors, and J. Martin. The design, fabrication, and evaluation of a ceramic counter-flow microchannel heat exchanger. *Appl. Thermal Engr.*, 31:2004–2012, 2011.

[18] X. Zhai, S. Ding, Y. Cheng, Y. Jin, and Y. Cheng. CFD simulation with detailed chemistry of steam reforming of methane for hydrogen production in an integrated micro-reactor. *Int. J. Hydrogen Energy*, 35(11):5383–5392, 2010. ISSN 0360–3199.

[19] A. Tomlin, T. Turányi, and M. Pilling. Chapter 4 mathematical tools for the construction, investigation and reduction of combustion mechanisms. In M. Pilling, editor, *Low-Temperature Combustion and Autoignition*, volume 35 of *Comprehensive Chemical Kinetics*, pages 293–437. Elsevier, 1997.

[20] M. Votsmeier. Efficient implementation of detailed surface chemistry into reactor models using mapped rate data. *Chem. Eng. Sci.*, 64(7):1384–1389, 2009. ISSN 0009–2509.

[21] T. Nien, J. Mmbaga, R. Hayes, and M. Votsmeier. Hierarchical multi-scale model reduction in the simulation of catalytic converters. *Chem. Eng. Sci.*, 93(0):362–375, 2013. ISSN 0009–2509.

[22] A. Scheuer, O. Hirsch, R. Hayes, H. Vogel, and M. Votsmeier. Efficient simulation of an ammonia oxidation reactor using a solution mapping approach. *Catal. Today*, 175(1):141–146, 2011. ISSN 0920–5861.

[23] U. Maas and S. Pope. Simplifying chemical kinetics: Intrinsic low-dimensional manifolds in composition space. *Combust. Flame*, 88(3–4):239–264, 1992. ISSN 0010–2180.

[24] M. J. McNenly, M. A. Havstad, S. M. Aceves, and W. J. Pitz. Integration strategies for efficient multizone chemical kinetics models. Technical report, SAE Technical Paper, 2010.

[25] S. M. Aceves, D. L. Flowers, C. K. Westbrook, J. R. Smith, W. Pitz, R. Dibble, M. Christensen, and B. Johansson. A multi-zone model for prediction of HCCI combustion and emissions. Technical report, SAE Technical paper, 2000.

[26] S. Pope. Computationally efficient implementation of combustion chemistry using *in situ* adaptive tabulation. *Combust. Theor. Model.*, 1(1):41–63, 1997.

[27] S. Pope, V. Hiremath, S. Lantz, Z. Ren, and L. Lu. ISAT-CK7: A Fortran 90 library to accelerate the implementation of combustion chemistry. http://tcg.mae.cornell.edu/ISATCK7, 2012.

[28] L. Lu and S. Pope. An improved algorithm for *in situ* adaptive tabulation. *J. Comput. Phys.*, 228(2):361–386, 2009. ISSN 0021–9991.

[29] S. Mazumder. Adaptation of the *in situ* adaptive tabulation (ISAT) procedure for efficient computation of surface reactions. *Comput. Chem. Eng.*, 30(1):115–124, 2005. ISSN 0098–1354.

[30] A. Kumar and S. Mazumder. Adaptation and application of the *in situ* adaptive tabulation (ISAT) procedure to reacting flow calculations with complex surface chemistry. *Comput. Chem. Eng.*, 35(7):1317–1327, 2011. ISSN 0098–1354.

[31] S. Tischer and O. Deutschmann. Recent advances in numerical modeling of catalytic monolith reactors. *Catal. Today*, 105(34):407–413, 2005. ISSN 0920-5861.

[32] O. Deutschmann. *Modeling and simulation of heterogeneous catalytic reactions: From the molecular process to the technical system.* John Wiley & Sons, 2013.

[33] E. A. Mason and A. Malinauskas. *Gas Transport in Porous Media: The Dusty-Gas Model.* American Elsevier, New York, 1983.

[34] H. Zhu, R. Kee, V. Janardhanan, O. Deutschmann, and D. Goodwin. Modeling elementary heterogeneous chemistry and electrochemistry in solid-oxide fuel cells. *J. Electrochem. Soc.*, 152:A2427–A2440, 2005.

[35] E. W. Thiele. Relation between catalytic activity and size of particle. *Ind. Eng. Chem.*, 31(7):916–920, 1939.

[36] H. Fogler. *Elements of chemical reaction engineering.* Prentice Hall, Upper Saddle River, NJ, 1992.

[37] M. K. Szukiewicz. An approximate model for diffusion and reaction in a porous pellet. *Chem. Eng. Sci.*, 57(8):1451–1457, 2002. ISSN 0009-2509.

[38] Y.-P. Sun, S.-B. Liu, and S. Keith. Approximate solution for the nonlinear model of diffusion and reaction in porous catalysts by the decomposition method. *Chem. Eng. J.*, 102(1):1–10, 2004. ISSN 1385-8947.

[39] J. C. Gottifredi and E. E. Gonzo. Approximate expression for the effectiveness factor estimation and a simple numerical method for concentration profile calculation in porous catalyst. *Chem. Eng. J.*, 109(1–3):83–87, 2005. ISSN 1385-8947.

[40] J. Lee and D. H. Kim. An approximation method for the effectiveness factor in porous catalysts. *Chem. Eng. Sci.*, 61(15):5127–5136, 2006. ISSN 0009-2509.

[41] A. Berson, H.-W. Choi, and J. G. Pharoah. Determination of the effective gas diffusivity of a porous composite medium from the three-dimensional reconstruction of its microstructure. *Phys. Rev. E*, 83:026310, 2011.

[42] G. Salejova, Z. Grof, O. Solcova, P. Schneider, and J. Kosek. Strategy for predicting effective transport properties of complex porous structures. *Comput. Chem. Eng.*, 35(2):200–211, 2011. ISSN 0098-1354.

[43] J. M. Zalc, S. C. Reyes, and E. Iglesia. The effects of diffusion mechanism and void structure on transport rates and tortuosity factors in complex porous structures. *Chem. Eng. Sci.*, 59(14):2947–2960, 2004. ISSN 0009-2509.

[44] M. J. Stutz and D. Poulikakos. Optimum washcoat thickness of a monolith reactor for syngas production by partial oxidation of methane. *Chem. Eng. Sci.*, 63(7):1761–1770, 2008. ISSN 0009–2509.

[45] P. Kočí, F. ŠtépÁnek, M. Kubíček, and M. Marek. Modelling of micro/nano-scale concentration and temperature gradients in porous supported catalysts. *Chem. Eng. Sci.*, 62(18–20):5380–5385, 2007. ISSN 0009-2509.

[46] M. Behnam, A. G. Dixon, M. Nijemeisland, and E. H. Stitt. Catalyst deactivation in 3D CFD resolved particle simulations of propane dehydrogenation. *Ind. Eng. Chem. Res.*, 49(21):10641–10650, 2010.

[47] J. Pereira, J. Navalho, A. Amador, and J. Pereira. Multi-scale modeling of diffusion and reaction-diffusion phenomena in catalytic porous layers: Comparison with the 1D approach. *Chem. Eng. Sci.*, 117:364–375, 2014.

[48] V. Novák, P. Kočí, M. Marek, F. Štěpánek, P. Blanco-García, and G. Jones. Multi-scale modelling and measurements of diffusion through porous catalytic coatings: An application to exhaust gas oxidation. *Catal. Today*, 188(1):62–9, 2012. ISSN 0920-5861.

[49] A. T. Naseri, B. A. Peppley, and J. G. Pharoah. Computational analysis of the reacting flow in a microstructured reformer using a multiscale approach. *AlChE J.*, 60(6):2263–2274, 2014. ISSN 1547-5905.

[50] P. Kočí, V. Novák, F. Štěpánek, M. Marek, and M. Kubíček. Multi-scale modelling of reaction and transport in porous catalysts. *Chem. Eng. Sci.*, 65(1):412–419, 2010. ISSN 0009-2509.

[51] Coorstek. Ad-94 alumina material properties. `http://www.coorstek.com/materials/ceramics/alumina_ad-94.php`, 2011.

[52] D. M. Murphy. *Development of a novel ceramic microchannel reactor for methane steam reforming.* Ph.D. thesis, Colorado School of Mines, 2013.

[53] T. Blacker. The cooper tool. In *5th International Meshing Roundtable, SAND 95-2130, Sandia National Laboratories*, pages 13–29. 1996.

[54] *GAMBIT 2.4 User's Guide*, 2007.

[55] R. K. Shah and D. P. Sekulić. *Fundamentals of Heat Exchanger Design.* John Wiley & Sons, Inc., 2007. ISBN 9780470172605.

[56] R. W. Powell, C. Y. Ho, and P. E. Liley. Thermal conductivity of selected materials. Technical report, National Bureau of Standards, 1966.

[57] D. C. Ginnings and R. J. Corruccini. Enthalpy, specific heat, and entropy of aluminum oxide from 0 ° to 900 °C. *Journal of Research of the National Bureau of Standards*, 38:593–600, 1947.

[58] A. Cybulski and J. A. Moulijn. *Structured catalysts and reactors*. CRC Press, 2005.

[59] H. Suzuki, H. Saito, and T. Hayashi. Thermal and electrical properties of alkoxy-derived cordierite ceramics. *J. Eur. Ceram. Soc.*, 9(5):365–371, 1992. ISSN 0955-2219.

[60] G. A. Slack. Thermal conductivity of pure and impure silicon, silicon carbide, and diamond. *J. Appl. Phys.*, 35(12):3460–3466, 1964.

[61] T. L. Bergman, A. S. Lavine, F. P. Incropera, and D. P. DeWitt. *Fundamentals of Heat and Mass Transport*. Wiley, 7th edition, 2011.

[62] Special Metals Corporation. Inconel alloy 625. www.specialmetals.com, 2015.

[63] D. Salmon, G. Roebben, A. Lamberty, and R. Brandt. Certification of thermal conductivity and thermal diffusivity up to 1025 K of a glass-ceramic reference material BCR-724. *Report EUR 21764 EN*, 2007.

[64] W. Stoecker. *Design Of Thermal Systems*. McGraw-Hill Education, 3rd edition, 1989. ISBN 9781259002397.

[65] D. Murphy, A. Manerbino, M. Parker, J. Blasi, R. Kee, and N. Sullivan. Methane steam reforming in a novel ceramic microchannel reactor. *Int. J. Hydrogen Energy*, 38(21):8741–8750, 2013. ISSN 0360–3199.

[66] C. Karakaya. *A novel, hierarchically developed surface kinetics for oxidation and reforming of methane and propane over* Rh/Al_2O_3. Ph.D. thesis, Karlsruhe Institute of Technology, 2012.

[67] C. Karakaya, R. Otterstätter, L. Maier, and O. Deutschmann. Kinetics of the water-gas shift reaction over Rh/Al_2O_3 catalysts. *Appl. Catal., A*, 470(0):31–44, 2014. ISSN 0926–860X.

[68] C. Eßmann, L. Maier, A. Li, S. Tischer, and O. Deutschmann. Natural Gas Steam Reforming over Rhodium/Alumina Catalysts: Experimental and Numerical Study of the Carbon Deposition from Ethylene and Carbon Monoxide. *Ind. Eng. Chem. Res.*, 53(31):12270–12278, 2014.

[69] B. T. Schädel, M. Duisberg, and O. Deutschmann. Steam reforming of methane, ethane, propane, butane, and natural gas over a rhodium-based catalyst. *Catal. Today*, 142(12):42–51, 2009. ISSN 0920-5861.

[70] C. H. Bartholomew. Mechanisms of catalyst deactivation. *Appl. Catal., A*, 212(12):17–60, 2001. ISSN 0926-860X.

[71] C. H. Bartholomew. Carbon deposition in steam reforming and methanation. *Catalysis Reviews*, 24(1):67 – 112, 1982.

[72] E. C. Luna, A. Becerra, and M. Dimitrijewits. Methane steam reforming over rhodium promoted Ni/Al_2O_3 catalysts. *React. Kinet. Catal. Lett.*, 67(2):247–252, 1999. ISSN 0133-1736.

[73] J. G. Jakobsen, M. Jakobsen, I. Chorkendorff, and J. Sehested. Methane steam reforming kinetics for a rhodium-based catalyst. *Catal. Lett.*, 140(3-4):90–97, 2010. ISSN 1011-372X.

[74] C. Bernardo, I. Alstrup, and J. Rostrup-Nielsen. Carbon deposition and methane steam reforming on silica-supported Ni-Cu catalysts. *Journal of Catalysis*, 96(2):517 – 534, 1985. ISSN 0021-9517.

[75] J. M. Blasi and R. J. Kee. In situ adaptive tabulation (ISAT) to accelerate transient computational fluid dynamics with complex heterogeneous chemical kinetics. *Comput. Chem. Eng.*, 84:36–42, 2016. ISSN 0098–1354.

[76] D. Goodwin, H. Moffat, and R. Speth. Cantera: An Object-oriented Software Toolkit for Chemical Kinetics, Thermodynamics, and Transport Processes. http://www.cantera.org, 2014. Version 2.1.2.

[77] C. García, D. Prett, and M. Morari. Model predictive control: Theory and practice —A survey. *Automatica*, 25(3):335–348, 1989. ISSN 0005–1098.

[78] E. Camacho and A. Carlos. *Model predictive control.* Springer Science & Business Media, 2013.

[79] L. Ljung. System identification. In A. Procházka, J. Uhlír, P. Rayner, and N. Kingsbury, editors, *Signal Analysis and Prediction*, Applied and Numerical Harmonic Analysis, pages 163–173. Birkhäuser Boston, 1998. ISBN 978-1-4612-7273-1.

[80] R. Kee, M. Coltrin, and P. Glarborg. *Chemically Reacting Flow: Theory and Practice*. Wiley, 2005. ISBN 9780471461302.

[81] A. Hindmarsh, P. Brown, K. Grant, S. Lee, R. Serban, D. E. Shumaker, and C. S. Woodward. SUNDIALS: Suite of Nonlinear and Differential/Algebraic Equation Solvers. *ACM Trans. Math. Software*, 31(3):363–396, 2005.

[82] S. Cohen and A. Hindmarsh. CVODE, A Stiff/Nonstiff ODE Solver in C. *Computers in Physics*, 10(2):138–143, 1996.

[83] C. Woodward, A. Hindmarsh, and R. Serban. SUNDIALS. http://computation.llnl.gov/casc/sundials/main.html, 2015.

[84] C. Karakaya, P. J. Weddle, J. M. Blasi, D. R. Diercks, and R. J. Kee. Modeling reaction-diffusion processes within catalyst washcoats: I. Microscale processes based on three-dimensional reconstructions. *Chem. Eng. Sci.*, submitted, 2015.

[85] J. Blasi, P. Weddle, C. Karakaya, D. Diercks, and R. Kee. Modeling reaction-diffusion processes within catalyst washcoats: II. Macroscale processes informed by microscale simulations. *Chem. Eng. Sci.*, submitted, 2015.

[86] N. Otsu. A threshold selection method from gray-level histograms. *Systems, Man and Cybernetics, IEEE Transactions on*, 9(1):62–66, 1979. ISSN 0018–9472.

[87] F. Zhang, R. Hayes, and S. Kolaczkowski. A new technique to measure the effective diffusivity in a catalytic monolith washcoat. *Chem. Eng. Res. Des.*, 82(4):481 – 489, 2004. ISSN 0263-8762. 8th {UK} National Heat Transfer Conference.

[88] B. Blakeley. *Autothermal reforming of methane for syngas production in a novel ceramic microchannel reactor*. Master's thesis, Colorado School of Mines, 2015.

[89] Y. Shi, W. H. G. Jr., H.-W. Wong, and O. O. Oluwole. Redesigning combustion modeling algorithms for the graphics processing unit (GPU): Chemical kinetic rate evaluation and ordinary differential equation integration. *Combust. Flame*, 158(5):836–847, 2011. ISSN 0010-2180.

[90] H. P. Le, J.-L. Cambier, and L. K. Cole. GPU-based flow simulation with detailed chemical kinetics. *Comput. Phys. Commun.*, 184(3):596–606, 2013. ISSN 0010-4655.

[91] M. Saito, J. Kojima, H. Iwai, and H. Yoshida. The limiting process in steam methane reforming with gas diffusion into a porous catalytic wall in a flow reactor. *Int. J. Hydrogen Energy*, 40(29):8844–8855, 2015. ISSN 0360–3199.

[92] R. R. Ratnakar and V. Balakotaiah. Reduced order multimode transient models for catalytic monoliths with micro-kinetics. *Chem. Eng. J.*, 260:557–572, 2015. ISSN 1385-8947.

[93] B. J. McBride, S. Gordon, and M. A. Reno. Coefficients for calculating thermodynamic and transport properties of individual species. Technical Report NASA-TM-4513, NASA Lewis Research Center, 1993.

[94] J. Rose and J. Cooper. *Technical data on fuels.* Wiley, 7th edition, 1977.

APPENDIX A - TECHNICAL DRAWINGS

The following pages contain technical drawings for a single ceramic slide, from which the larger microchannel reactor is assembled.

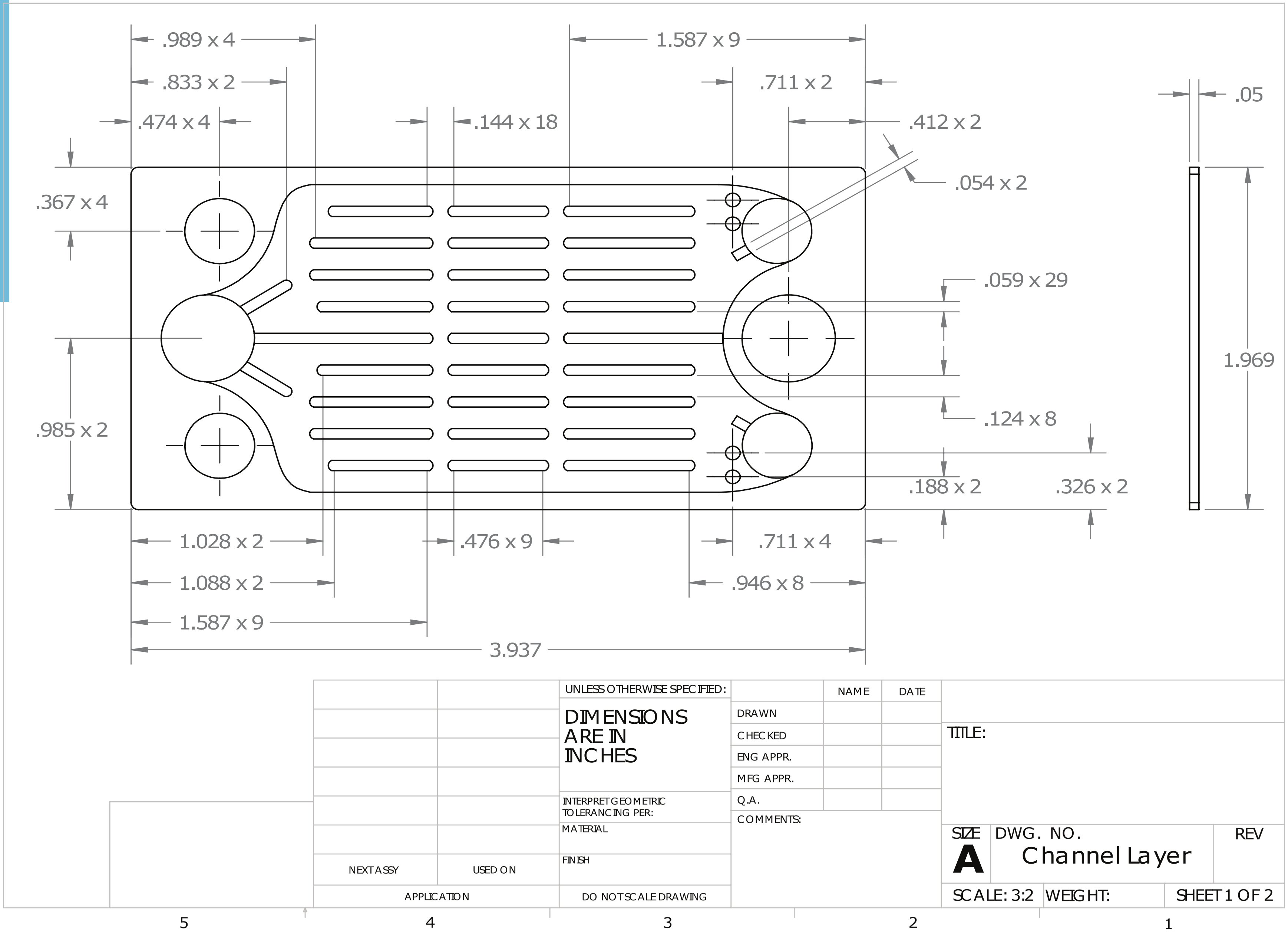
.989 x 4
.833 x 2
.474 x 4
.144 x 18
1.587 x 9
.711 x 2
.412 x 2
.054 x 2
.05
.367 x 4
.059 x 29
1.969
.985 x 2
.124 x 8
.188 x 2
.326 x 2
1.028 x 2
.476 x 9
.711 x 4
1.088 x 2
.946 x 8
1.587 x 9
3.937
UNLESS OTHERWISE SPECIFIED:
DIMENSIONS ARE IN INCHES
INTERPRET GEOMETRIC TOLERANCING PER:
MATERIAL
FINISH
NEXT ASSY
USED ON
APPLICATION
DO NOT SCALE DRAWING
NAME
DATE
DRAWN
CHECKED
ENG APPR.
MFG APPR.
Q.A.
COMMENTS:
TITLE:
SIZE
A
DWG. NO.
Channel Layer
REV
SCALE: 3:2
WEIGHT:
SHEET 1 OF 2
5
4
3
2
1

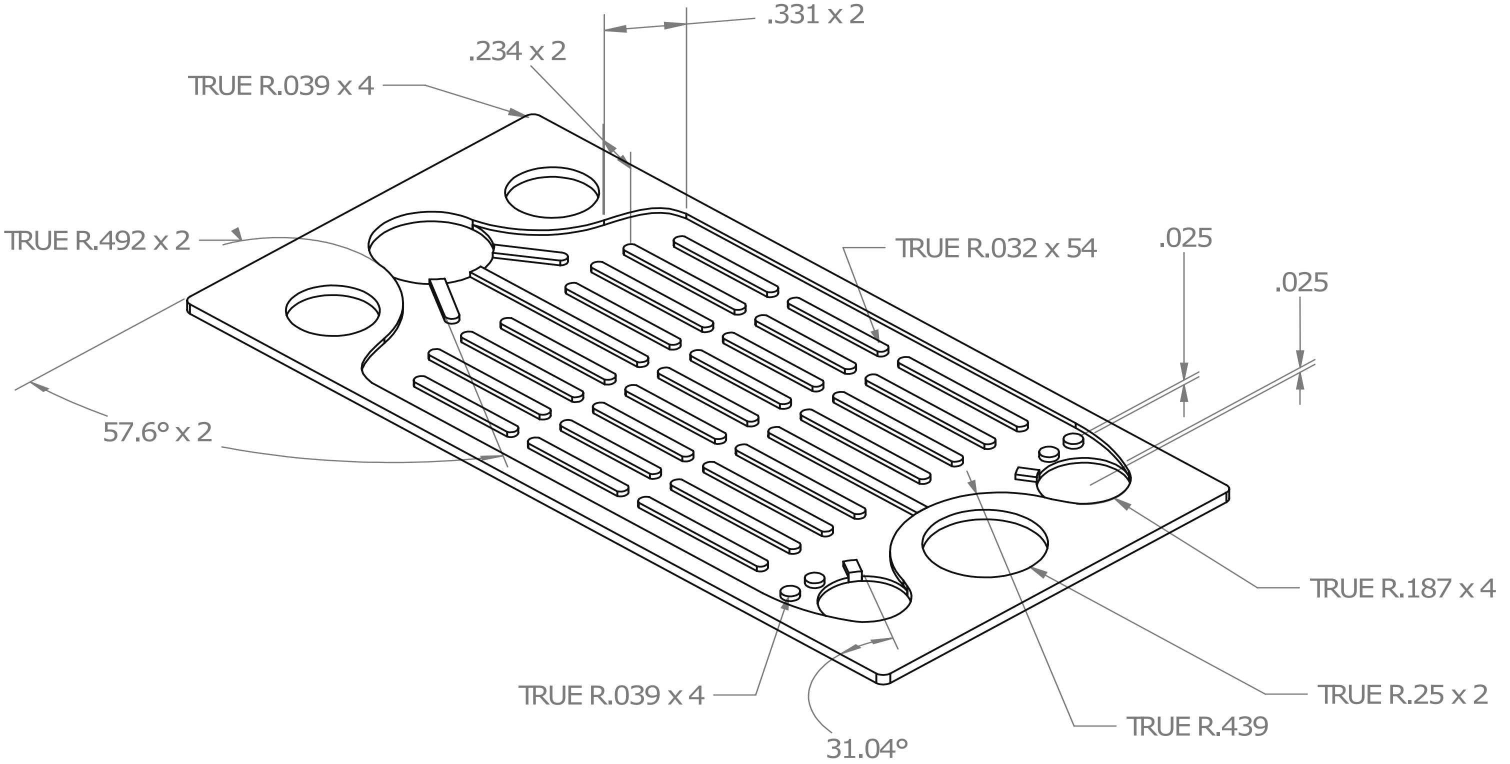

UNLESS OTHERWISE SPECIFIED:		NAME	DATE
DIMENSIONS ARE IN INCHES	DRAWN		
	CHECKED		
	ENG APPR.		
	MFG APPR.		
INTERPRET GEOMETRIC TOLERANCING PER:	Q.A.		
MATERIAL	COMMENTS:		
FINISH			
DO NOT SCALE DRAWING			

NEXT ASSY	USED ON
APPLICATION	

TITLE:

SIZE A DWG. NO. Channel Layer REV

SCALE: 3:2 WEIGHT: SHEET 2 OF 2

5 4 3 2 1

APPENDIX B - THERMOPHYSICAL PROPERTIES OF FLUIDS

Table B.1 contains the coefficients $A_{1\text{–}5}$ for evaluating the temperature dependent properties of various gases used in the simulations in this work. The thermophysical properties are evaluated as

$$P(T) = A_1 + A_2T^2 + A_3T^3 + A_4T^4 + A_5T^5 \tag{B.1}$$

where $P(T)$ is the property being evaluated and T is the temperature in K. The units of specific heat, thermal conductivity, and viscosity are J kg^{-1} K^{-1}, W m^{-1} K^{-1}, and kg m^{-1} s^{-1} respectively.

Table B.1: Thermophysical property coefficients [93, 94]

	A_1	A_2	A_3	A_4	A_5
H_2O(g)					
$c_p(T)$	1.5631E+03	1.6038E+00	-2.9328E-03	3.2161E-06	-1.1568E-09
$\lambda(T)$	-7.9680E-03	6.8813E-05	4.4905E-08	-9.0999E-12	6.1733E-16
$\mu(T)$	-4.4189E-06	4.6876E-08	-5.3894E-12	3.2029E-16	4.9192E-22
O_2(g)					
$c_p(T)$	8.3483E+02	2.9296E-01	-1.4956E-04	3.4139E-07	-2.2784E-10
$\lambda(T)$	3.9218E-03	8.0812E-05	-1.3541E-08	2.2204E-12	-1.4161E-16
$\mu(T)$	7.8794E-06	4.9249E-08	-9.8515E-12	1.5274E-15	-9.4257E-20
CH_4(g)					
$c_p(T)$	4.0358E+02	9.0573E+00	-1.4425E-02	1.5805E-05	-6.3431E-09
$\lambda(T)$	3.3200E-02				
$\mu(T)$	1.0870E-05				
CO_2(g)					
$c_p(T)$	4.2993E+02	1.8745E+00	-1.9665E-03	1.2973E-06	-4.0000E-10
$\lambda(T)$	1.4500E-02				
$\mu(T)$	1.3700E-05				
CO(g)					
$c_p(T)$	9.6839E+02	4.4879E-01	-1.1522E-03	1.6569E-06	-7.3464E-10
$\lambda(T)$	2.5000E-02				
$\mu(T)$	1.7500E-05				
H_2(g)					
$c_p(T)$	1.3602E+04	3.4023E+00	-3.3584E-03	-3.9080E-07	1.7053E-09
$\lambda(T)$	8.2691E-02	3.5615E-04	1.0723E-08	-4.4052E-12	3.2633E-16
$\mu(T)$	3.7733E-06	1.9323E-08	-3.2320E-12	4.9170E-16	-3.0243E-20
N_2(g)					
$c_p(T)$	9.7904E+02	4.1796E-01	-1.1763E-03	1.6744E-06	-7.2563E-10
$\lambda(T)$	4.7371E-03	7.2719E-05	-1.1220E-08	1.4549E-12	-7.8717E-17
$\mu(T)$	7.4733E-06	4.0837E-08	-8.2446E-12	1.3056E-15	-8.1779E-20

APPENDIX C - CO-AUTHOR PERMISSIONS

I hereby provide my permission to Justin Blasi to use material from [1] and support material from [2], for which I am a co-author, in his thesis.

[1] J. Blasi, P. Weddle, C. Karakaya, D. Diercks, and R. Kee. Modeling reaction-diffusion processes within catalyst washcoats: II. Macroscale processes informed by microscale simulations. *Chem. Eng. Sci.*, submitted, 2015.

[2] C. Karakaya, P. J. Weddle, J. M. Blasi, D. R. Diercks, and R. J. Kee. Modeling reaction-diffusion processes within catalyst washcoats: I. Microscale processes based on three-dimensional reconstructions. *Chem. Eng. Sci.*, submitted, 2015.

Co-Author	Date
Canan Karakaya	11/16/15
Peter Weddle	11/16/15
Dave Diercks	11/16/15